ISSN : 2165-4069(Online)
ISSN : 2165-4050(Print)

IJARAI

International Journal of Advanced Research in Artificial Intelligence

Volume 2 Issue 12

www.ijarai.thesai.org

A Publication of
The Science and Information Organization

IJARAI

INTERNATIONAL JOURNAL OF
ADVANCED RESEARCH IN ARTIFICIAL INTELLIGENCE

THE SCIENCE AND INFORMATION ORGANIZATION

www.thesai.org | info@thesai.org

Editorial Preface

From the Desk of Managing Editor…

“The question of whether computers can think is like the question of whether submarines can swim.” ― Edsger W. Dijkstra, the quote explains the power of Artificial Intelligence in computers with the changing landscape. The renaissance stimulated by the field of Artificial Intelligence is generating multiple formats and channels of creativity and innovation.

This journal is a special track on Artificial Intelligence by The Science and Information Organization and aims to be a leading forum for engineers, researchers and practitioners throughout the world.

The journal reports results achieved; proposals for new ways of looking at AI problems and include demonstrations of effectiveness. Papers describing existing technologies or algorithms integrating multiple systems are welcomed. IJARAI also invites papers on real life applications, which should describe the current scenarios, proposed solution, emphasize its novelty, and present an in-depth evaluation of the AI techniques being exploited. IJARAI focusses on quality and relevance in its publications.

In addition, IJARAI recognizes the importance of international influences on Artificial Intelligence and seeks international input in all aspects of the journal, including content, authorship of papers, readership, paper reviewers, and Editorial Board membership.

The success of authors and the journal is interdependent. While the Journal is in its initial phase, it is not only the Editor whose work is crucial to producing the journal. The editorial board members , the peer reviewers, scholars around the world who assess submissions, students, and institutions who generously give their expertise in factors small and large— their constant encouragement has helped a lot in the progress of the journal and shall help in future to earn credibility amongst all the reader members.

I add a personal thanks to the whole team that has catalysed so much, and I wish everyone who has been connected with the Journal the very best for the future.

Thank you for Sharing Wisdom!

Managing Editor
IJARAI
Volume 2 Issue 12 December 2013
ISSN: 2165-4069(Online)
ISSN: 2165-4050(Print)

Editorial Board

Reviewer Board Members

CONTENTS

Method for Aureole Estimation Refinement Through Comparisons Between Observed Aureole and Estimated Aureole Based on Monte Carlo Ray Tracing

Kohei Arai [1]
Graduate School of Science and Engineering
Saga University
Saga City, Japan

***Abstract*—Method for aureole estimation refinement through comparisons between observed aureole and estimated aureole based on Monte Carlo Ray Tracing: MCRT is proposed. Through some experiments, it is found that the proposed method does work for refinement of aureole estimation. The experimental results also show the proposed method is validated through comparison with empirical aureole estimation equation which is proposed by Shebrooke University research group.**

Keywords*—*Monte Carlo method; Ray tracing method; Aureole; aerosol; optical depth; solar diffuse; solar direct

I. INTRODUCTION

In order to improve estimation accuracy of aerosol refractive index, it is necessary to improve estimation accuracy and measuring accuracy of aureole, and solar diffuse irradiance. It is not so difficult to improve solar direct irradiance because it is large enough for measurements. Meanwhile, it is not so easy to improve measuring and estimating aureole and solar diffuse irradiance because these are quit small.

For many years, research scientists proposed their method for measurement and estimation of aureole which results in empirical equation of aureole. One of those is the well known empirical equation proposed by Shebrooke University research group.

On the other hand, it would be better to improve or refine the estimated aureole by using empirical equation. Aureole can be estimated with some atmospheric codes, or Monte Carlo Ray Tracing: MCRT method. Measured aureole can be refined by using estimated aureole derived from MCRT in the sense of least square means. The proposed method is based on this idea. Through comparisons the refined aureole and empirically estimated aureole, the proposed method can be validated.

The following section describes research background and the proposed method followed by some experimental data. Then conclusion is described together with some discussions.

II. PROPOSED MODEL

A. Theoretical Background

The solar aureole is a region of enhanced brightness within about 20° of the sun's disk, due to the predominant forward-scattering effect of atmospheric aerosols. The solar aureole theory and its use for determining aerosol size distributions also has been discussed in detail by Deirmendjian(1959). Here, we calculated aureole irradiance using MS(multiply scattering) approximation proposed by M.A.Box et.al(1981). They assumed that the solar aureole irradiance was essentially due to SS(single scattering) by aerosols and molecules, and MS by molecules alone. Moreover, they also taken into account the effect of the surface reflectance in the computation of the aureole irradiance. P.Romanov et al.(1999) summarized an empirical formula of aureole irradiance based on the method proposed by M.A.Box et.al. It is shown as follows,

$$I_{aur}(\Theta,\lambda)=\frac{F_0(\lambda)}{\mu_0}\exp\left(-\frac{\tau(\lambda)}{\mu_0}\right)\left(\tau_{mol}(\lambda)P_{mol}(\Theta,\lambda)+\tau_{sca}(\lambda)P_{aer}(\Theta,\lambda)+\Delta_{ms}(\Theta,\lambda,A)\right) \quad (1)$$

where),(λΘ*aurI* is the aureole irradiance measured at scattering angle Θ,),(λΘ*molP* and),(λΘ*aerP* are the Rayleigh and aerosol phase functions, respectively.)(λτ*sca* is the aerosol scattering optical depth.),,(*Ams*λΘΔ is a term that represents the contribution of the effects of multiple scattering and reflection from the surface in solar aureole. It can be written as follows,

$$\Delta_{ms}(\Theta,\lambda,A)=\tau_A(\lambda,A)P_{mol}(0^0,\lambda)+P_{mol}(\Theta,\lambda)t_{ms} \quad (2)$$

where

$$\tau_A(\lambda,A)=A\tau_2/(1-A\tau_3),$$

$$\tau_2=1.34\tau_{ss}\mu_0/(1.0+0.22(\tau_{ss}/\mu_0)^2), \quad (3)$$

$$\tau_3=0.9\tau_{ss}-0.92\tau_{ss}^2+0.54\tau_{ss}^3, \quad (4)$$

$$t_{ms}=0.02\tau_{ss}+1.2\tau_{ss}^2/\mu_0^{0.25},$$

$$\tau_{ss}=\tau_R(\lambda)+\tau_{sa}(\lambda) \quad (5)$$

A is the surface reflectance and $ss\tau$ is the total scattering optical depth.

Figure 1 shows a comparison of the calculated result between aureole irradiance from MS model and diffuse irradiance from the method of successive orders of scattering. The aureole irradiance was calculated by the aureole model described as above in an angle range of the forward scattering in which the azimuth angles are from 0° to 30° and the zenith angle is the same as the solar zenith angle. Meanwhile, the diffuse irradiance was calculated in all azimuth angles from 0° to 180° by the method of the successive orders of scattering. In the forward scattering, we found that it was quite different of calculated results between the diffuse irradiance and the aureole irradiance. This is because that it exist not only scattering but also diffraction when light passes particle in the forward direction. It results in generating a region of enhanced brightness in forward direction. From now on, we removed the unrealistic part of diffuse irradiance, and remained the corresponding exact estimates of the aureole irradiance in the forward scattering.

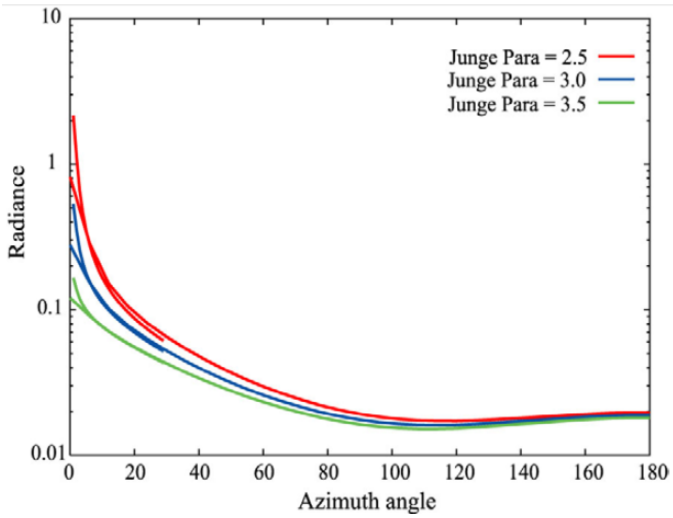

Fig. 1. Comparison the Aureole Irradiance from MS Model and Diffuse Irradiance from the Method of Successive Orders of Scattering

B. Shebrooke Model

The estimation method for the refractive index and the size distribution of aerosol proposed by P.Romanovs of the Sherbrooke University based on linear inversion method is summarized as follows. The aerosol refractive index and size distribution are retrieved by minimizing the squared difference between the measured data and the simulated data of direct solar irradiance at surface (or aerosol optical depth), downward diffuse irradiance at surface and solar peripheral irradiance (aureole) based on the plane-parallel atmospheric model. This model also considered molecular Rayleigh scattering and Mie scattering which is dependence on the aerosol refractive index and size distribution.

First,

$$F = H\varphi + e \tag{6}$$

is defined where F is the vector of the deviations of the measured data, that is,

$$F = \begin{pmatrix} I_{dir} - I^*_{dir} \\ I_{dif} - I^*_{dif} \\ I_{aur} - I^*_{aur} \end{pmatrix} \tag{7}$$

[*] denotes the measurement data. H is a Jacobian, and can be expressed as,

$$H = \begin{pmatrix} I'_{dir}(\nu 1) & \dots & I'_{dir}(\nu m) & I'_{dir}(\kappa) & I'_{dir}(\eta) \\ I'_{dif}(\nu 1) & \dots & I'_{dif}(\nu m) & I'_{dif}(\kappa) & I'_{dif}(\eta) \\ I'_{aur}(\nu 1) & \dots & I'_{aur}(\nu m) & I'_{aur}(\kappa) & I'_{aur}(\eta) \end{pmatrix} \tag{8}$$

where I*dir* is Solar direct irradiance, *IdifI* is Solar diffuse irradiance and *Iaur* is aureole irradiance. $I'_{dir}, I'_{dif}, I'_{aur}$ individually indicate a factor of the matrix when the relation between the direct and diffuse solar irradiance and aureole, and the refractive index and size distribution of aerosol is represented as a matrix.

It is also expressed that $E = E_0 \exp(-\tau/\mu_0)$, where E0 is the exoatmospheric solar irradiance. According to previous equation, we can replace the direct solar irradiance with aerosol optical depth. From now on, discussion will be focused on aerosol optical depth instead of the direct solar irradiance. 0*E*

In the formulation of the inverse problem the vector ϕ is defined as follows,

$$\varphi^T = \{\varphi_{\nu 1} \dots \varphi_{\nu m}, \varphi_\kappa, \varphi_\eta\}$$

$$\varphi_{\nu m} = s - s^*$$

$$s \in \nu 1, \dots, \nu m, \kappa, \eta \tag{9}$$

where *m*νν,...,1 represent size distribution of aerosol per air column. ηκ, are the real part and the imaginary part of the refractive index.

Because the aerosol optical depth, diffuse solar irradiance and aureole can be measured on the ground, the Eq.(5.2) can be given. It is possible to estimate the unknown parameters of the refractive index and the size distribution of aerosol in the Eq.(5.3). However, because the number of the unknown parameters that represent the size distribution and the real part and the imaginary part of the refractive index is far more than the number of the measured data, it is an ill-posed problem. Hence, it can be solved with commonly used inversion solution based on minimizing norm of estimation error then,

$$\varphi = H^T [HH^T]^{-1} F \tag{10}$$

It is well known that the retrieval accuracy of the minimized norm method is not good enough because the number of the unknown parameters is more than it of the equations given. Since the influence of the imaginary part of the refractive index on aureole is so small that the accuracy improvement of the imaginary part of refractive index cannot be expected from this method.

Assuming the aerosol size distribution as Junge distribution, according to Eq.(3.22), the size distribution can be represented as only one Junge parameter(a). Therefore, the Eq.(5.3) can be rewritten as,

$$H = \begin{pmatrix} \tau'_{aer}(a) & \tau'_{aer}(\kappa) & \tau'_{aer}(\eta) \\ I'_{dif}(a) & I'_{dif}(\kappa) & I'_{dif}(\eta) \\ I'_{aur}(a) & I'_{aur}(\kappa) & I'_{aur}(\eta) \end{pmatrix} \tag{11}$$

The number of the unknown parameters is three which is totally identical to the number of the equations to be given, so that

$$\begin{pmatrix} \kappa-\kappa^* \\ \eta-\eta^* \\ a-a^* \end{pmatrix} = \begin{pmatrix} \tau'_{aer}(a) & \tau'_{aer}(\kappa) & \tau'_{aer}(\eta) \\ I'_{dif}(a) & I'_{dif}(\kappa) & I'_{dif}(\eta) \\ I'_{aur}(a) & I'_{aur}(\kappa) & I'_{aur}(\eta) \end{pmatrix}^{-1} \begin{pmatrix} \tau_{aer}-\tau^*_{aer} \\ I_{dif}-I^*_{dif} \\ I_{aur}-I^*_{aur} \end{pmatrix} \tag{12}$$

The refractive index and Junge parameter can be retrieved simultaneously

In accordance with Shebrooke University group, aureole can be expressed in equation (1), empirically.

$$L = \Phi_0 \sec\theta_0 \exp(-\tau_T \sec\theta_0)$$
$$[(\tau_M + \tau_{MS})P_M + \tau_{PS}P_P + \tau_A P_M(0^\circ)] \tag{13}$$

where

$$\tau_A = \frac{A\tau_2(\tau_{SS},\mu_0)}{1 - A\tau_3(\tau_{SS})},$$

$$\tau_{MS} = 0.02\tau_{SS} + 1.2\tau_{SS}^2\mu_0^{-1/4}$$

$$\tau_A = \frac{A\tau_2(\tau_{SS},\mu_0)}{1 - A\tau_3(\tau_{SS})}$$

$$\tau_2 = 1.34\tau_{SS}\mu_0[1.0 + 0.22(\tau_{SS}/\mu_0)^2]$$

$$\tau_3 = 0.9\tau_{SS} - 0.92\tau_{SS}^2 + 0.54\tau_{SS}^3$$

$$\tau_{SS} = \tau_M + \tau_{PS} \qquad \mu_0 = \cos\theta_0 \tag{14}$$

Thus aureole can be estimated with the above empirical equation.

C. Methiod for Refinement of Measured Aureole

Figure 2 shows the proposed method for refinement of measured aureole with estimated aureole based on MODTRAN. Method for aureole estimation refinement through comparisons between observed aureole and estimated aureole based on Monte Carlo Ray Tracing: MCRT is proposed.

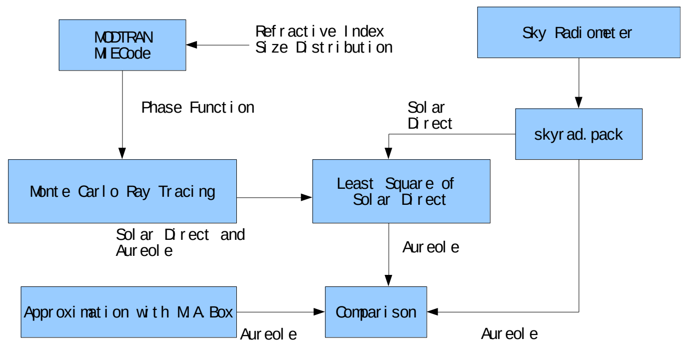

Fig. 2. shows the proposed method for refinement of measured aureole with estimated aureole based on MODTRAN.

Essentially, aureole can be measured with sky radiometer which is shown in Figure 3.

Fig. 3. Outlook of the sky radiometer manufactured by PREDE Co. Ltd. Japan

POM-1 of Sky radiometer manufactured by Prede Co. Ltd. Japan is used for measurements of solar direct and diffuse irradiance including aureole. In order for improvement of irradiance measurement accuracy, the proposed method minimizes the difference between measured and model derived aureole. Mie code of MODTRAN of atmospheric code allows estimating phase function (scattering angle dependency) which depends on aerosol refractive index and size distribution. MCRT, on the other hand, allows estimation of refractive index and size distribution with the other atmospheric parameters including optical depth. Meanwhile, solar direct, diffuse including aureole can be measured with POM-01. Through minimizing square difference between the measured and estimated solar direct irradiance, estimation accuracy for aureole can be improved. After that aureole can be refined through comparison between empirical aureole calculated by using model proposed by Box et al. and measured aureole.

D. Monte Carlo Ray Tracing Model

Figure 4 shows flow chart of MCRT.

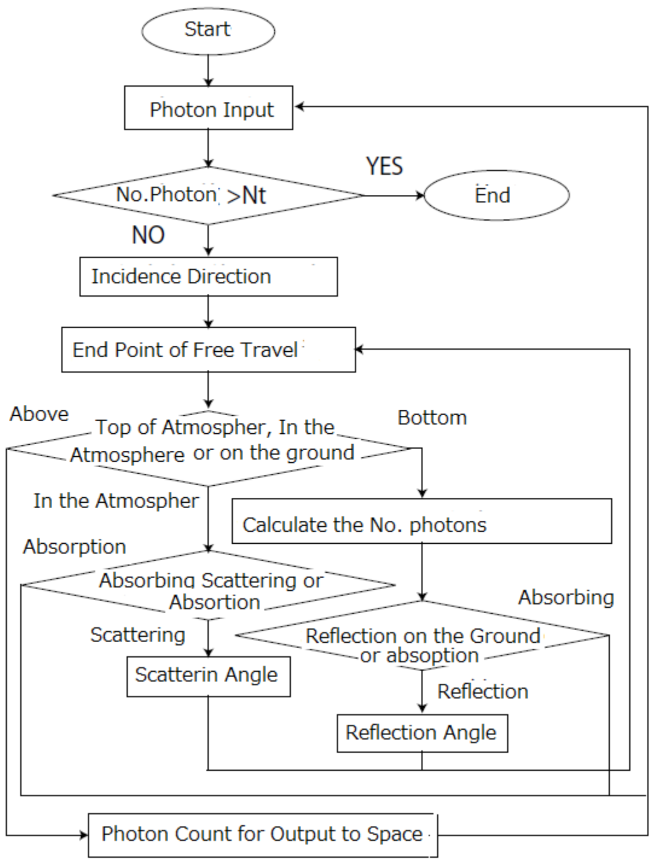

Fig. 4. Flowchart of MCRT

Scattering angle is defined in Figure 5.

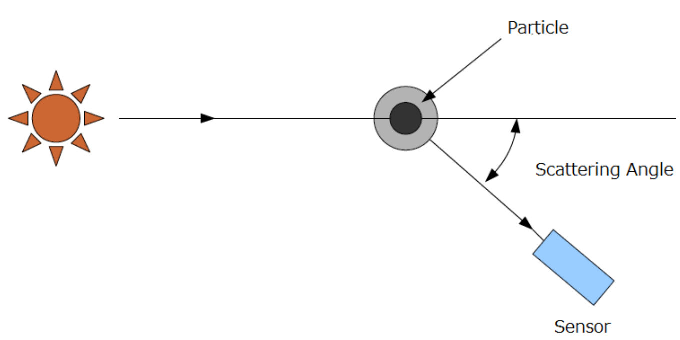

Fig. 5. Definition of scattering angle

Examples of phase function is shown in Figure 6.

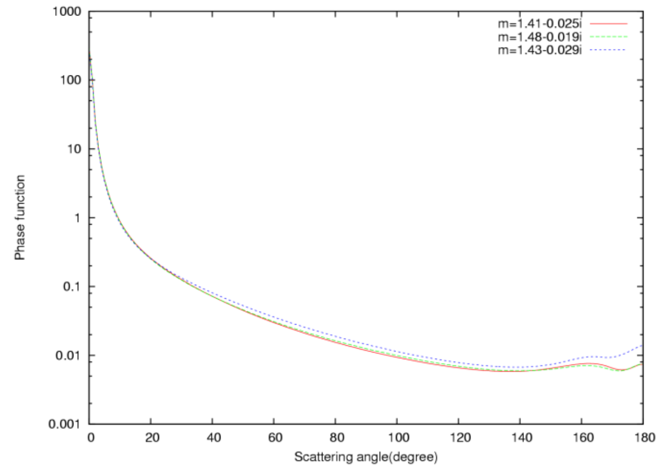

Fig. 6. Examples of phase functions

Refractive indexes of the examples are as follows,

m=1.41-0.025i
m=1.48-0.019i
m=1.43-0.029i

A photon is put in the simulation cell from the top of the cell with the incidence angle that depends on the specified solar zenith angle. The position of which the photon is put in is changed by time by time in accordance with the uniformly distributed random numbers.

Depending on the optical depth of the atmosphere, free travel length L of photon is determined as follows,

$$L = -L_0 \log(Rnd) \tag{15}$$

$$L_0 = \frac{h}{\tau_{all}} \tag{16}$$

where L_0 is called free travel length, denoting the average distance of interaction of a photon from one position to another. Rnd is uniformly distributed random numbers ranges from 0 to 1. h denotes the physical height of the atmosphere (50km in this case) while τ_{all} denotes the optical depth of the atmosphere which is determined as follows,

$$\tau_{all} = \tau_{aero} + \tau_{mol} \tag{17}$$

where the subscript $aero$ is associated with aerosols while mol with molecules. Here, it is assumed that atmosphere consists of aerosols and air molecules. Because the wavelength in concern ranges from 450 to 1050nm so that optical depth of ozone and water vapors are assumed to be negligible except 936nm of water vapor absorption band. A small absorption due to ozone is situated from 500 to 650nm around.

The photon meets aerosol particles or molecule when the photon travels in the atmosphere then scattering due to the aerosols or molecules occurs. The probability of the collision to the aerosols or molecules depends on their optical depths. If the endpoint of photon travel is in the atmosphere, the photon meets aerosol or molecule. The probability of the photon meets aerosol is τ_{aero}/τ_{all} while that of the photon meets molecule is τ_{mol}/τ_{all}. In accordance with the phase function of aerosols or molecules, the photon is scattered. Strength of scattering as a function of scattering angle θ is determined by the phase function, *P(θ)*, the Rayleigh for molecules, equation (4) and Heyney-Greestein function, equation (5) (it is just an approximation function of which the phase function is monotonically decreasing) for aerosols. Actual phase function can be determined with MODTRAN 4.0 of Mie code with the measured refractive index of aerosols through field experiments. By using uniformly distributed random numbers, scattering direction is determined. The phase function as $P(\theta)$, where θ is the angle between the incident direction and the scattering direction.

For molecules, the Rayleigh phase function is as follows,

$$P(\theta) = (3/4)(1+\cos^2\theta) \tag{18}$$

while that for aerosols, we use the Heyney-Greenstein approximation function of the following,

$$P(\theta) = \frac{1-g_\lambda^2}{(1+g_\lambda^2-2g_\lambda\cos\theta)^{3/2}} \tag{19}$$

where g_λ is the asymmetry factor of the aerosol phase function which depends on the wavelength of the radiation and the compositions, sizes, and the shapes of the aerosol particles.

In the calculation of TOA radiance, the number of photons, *N* which comes out from the top of the atmosphere within the angle range which corresponds to the Instantaneous Field of View: IFOV of the sensor in concern is used thus the normalized TOA radiance, *Rad* is determined as follows,

$$Rad = \frac{\mu_0\mu\Delta\mu}{2}\left(\frac{N}{N_{total}}\right) \tag{20}$$

where $\mu_0 = \cos\theta_0$, $\mu = \cos\theta$, θ_0 is the solar zenith angle and θ is a viewing solid angle. $\Delta\mu$ is a view solid angle, i.e., FOV (field of view).

N_{total} is the number of photons which are put in the cell in total. If you multiply solar irradiance to *Rad* in unit of (W/m^2/str/μm), then the TOA radiance in the same unit is calculated.

III. EXPERIMENTS

A. Measured Data

Table 1 shows measured data which are obtained at Saga University, Japan at 11:35 Local Time in Japan on April 25 2004. It was fine day. Solar zenith angle was 22.5 degree at that time.

TABLE I. PARAMETRRS MEASURED AT EXPERIMENTS

Wavelength(um)	0.400	0.500	0.675	0.870	1.020
Real_Refractive_Index	1.430	1.410	1.430	1.490	1.450
Imaginary_Refractive_Index	0.028	0.017	0.024	0.006	0.018
Aerosol_Optical_Depth	0.295	0.220	0.170	0.140	0.125
Molecule_Optical_Depth	0.360	0.143	0.024	0.015	0.008

Solar irradiances estimated with Sky Rad Pack, empirical equation (Box), and Monte Carlo is shown in Figure 7. Although the proposed method utilizing Monte Carlo Ray Tracing simulation shows better accuracy rather than Sky Rad Pack and empirical equation for shorter wavelength, the proposed method shows poorer accuracy than the conventional methods for longer wavelength. The reason for this is atmospheric optical depth is too thin.

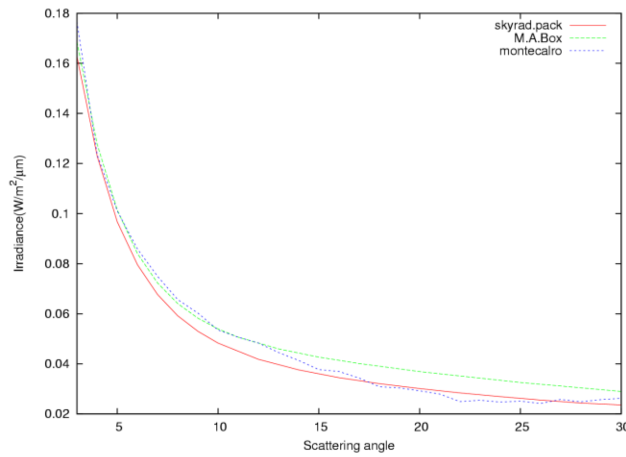

(a)400nm

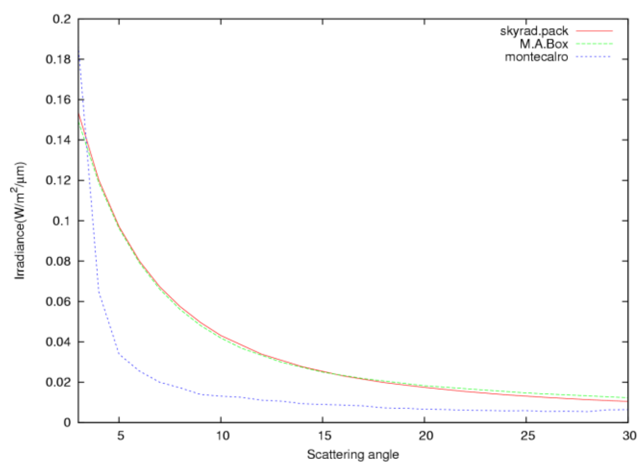

(b)500nm

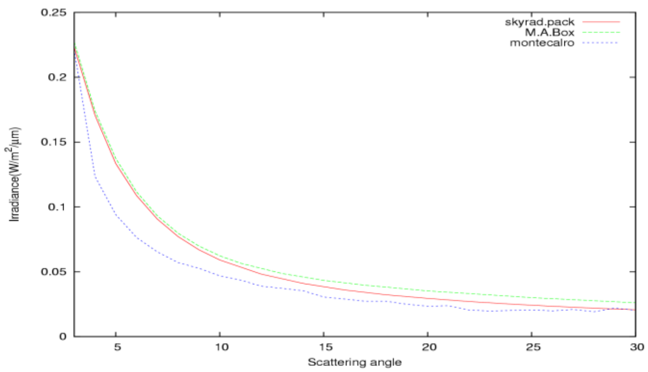

(c)675nm

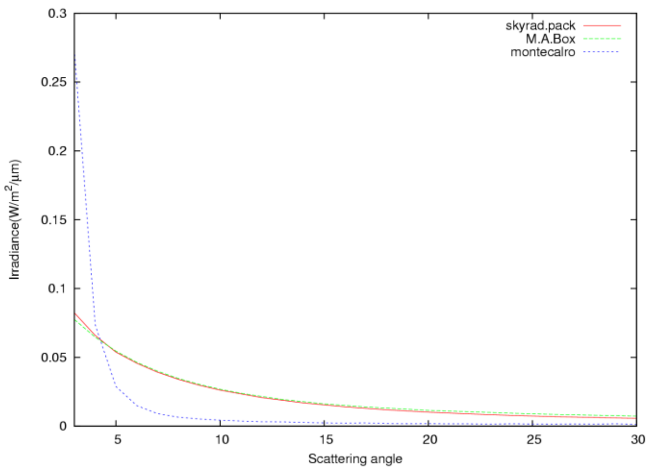

(d)875nm

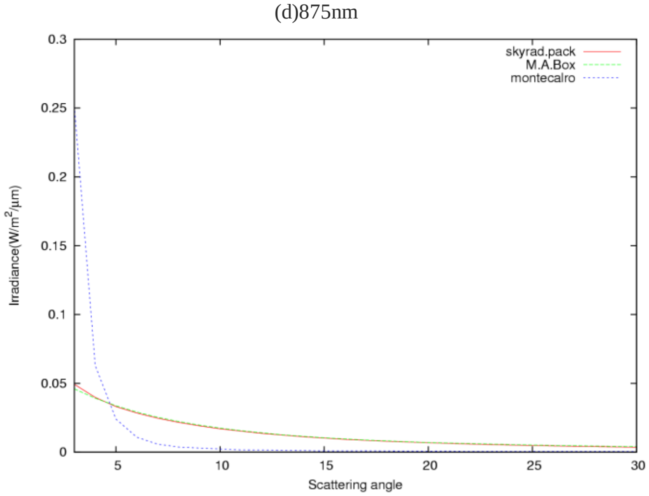

(e)1020nm

Fig. 7. Solar irradiances estimated with (a) Sky Rad Pack, (b) empirical equation (Box) and (c) Monte Carlo simulation.

Estimation error is defined with equation (15).

$$\text{Error}\,(\%) = \sqrt{\frac{\sum\left(\frac{X_n - x_n}{X_n}\right)^2}{N}} \times 100 \qquad (15)$$

Estimation errors of real and imaginary parts of refractive index, aerosol optical depth, molecule optical depth and surface reflectance are shown in Table 2.

TABLE II. ESTIMATION ERRORS OF REAL AND IMAGINARY PARTS OF REFRACTIVE INDEX, AEROSOL OPTICAL DEPTH, MOLECULE OPTICAL DEPTH AND SURFACE REFLECTANCE

Wavelength(um)	0.400	0.500	0.675	0.870	1.020
Refractive_Index	0.9%	22.7%	67.0%	78.5%	81.0%
Aerosol_Optical_Depth	26.4%	57.9%	83.3%	93.6%	96.1%
Molecule_Optical_Depth	17.4%	69.8%	99.0%	97.1%	95.6%
Surface_Reflectance	27.4%	50.3%	82.3%	90.4%	92.5%

B. Sensitivity Analysis

Sensitivity analysis is conducted for validation of the proposed method. Designated parameters for sensitivity analysis are shown in Table 3. Meanwhile, Table 4 shows the results from the sensitivity analysis.

TABLE III. PARAMETERS FOR SENSITIVITY ANALYSIS

		Min.	Max.	Step
Refractive Index	Real	1.350	1.600	0.010
	Imaginary	0.000	0.030	0.001
Optical Depth	Aerosol	0.000	1.000	0.050
	Molecule	0.000	1.000	0.050
Surface Reflectance		0.000	1.000	0.050

TABLE IV. THE RESULTS FROM THE SENSITIVITY ANALYSIS.

Wavelength(μm)		0.400	0.500	0.675	0.870	1.020
Refractive Index		4.9%	-12.0%	-64.5%	-72.3%	-78.0%
Optical Depth	Aerosol	-11.8%	-47.2%	-80.8%	-87.5%	-93.1%
	Molecule	-2.8%	-59.1%	-96.5%	-90.9%	-92.6%
Surface Reflectance		-12.8%	-39.6%	-79.8%	-84.3%	-89.5%

It is found that only real and imagery parts of refractive index at 400 nm shows relatively good estimation accuracy. The other parameters show under estimated situation. One of the reasons for this is that the number steps for real and imaginary parts are greater than the others. Estimation accuracy at 1020nm is not so good relatively. There are small absorptions due to water vapor and ozone at the 1020nm slightly.

Estimation accuracy for the shorter wavelength is better than that for longer wavelength. Therefore, the sensitivity for the shorter wavelength is greater than that for the longer wavelength.

C. Relation between estimation errors of aureole and refractive index

Aureole estimation accuracy may affect to estimation of refractive index. Relation between estimation error of aureole and refractive index is investigated with the parameters listed in Table 2. The relation between aureole and real part of refractive index is shown in Figure 8 (a) while that between aureole and imaginary part of refractive index is shown in Figure 8 (b).

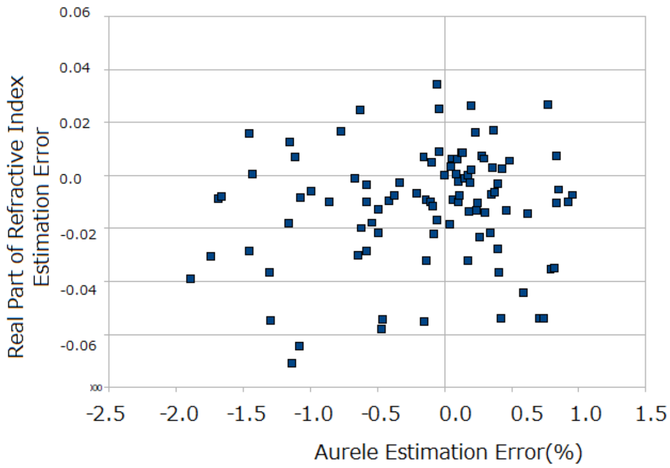

(a)Real part

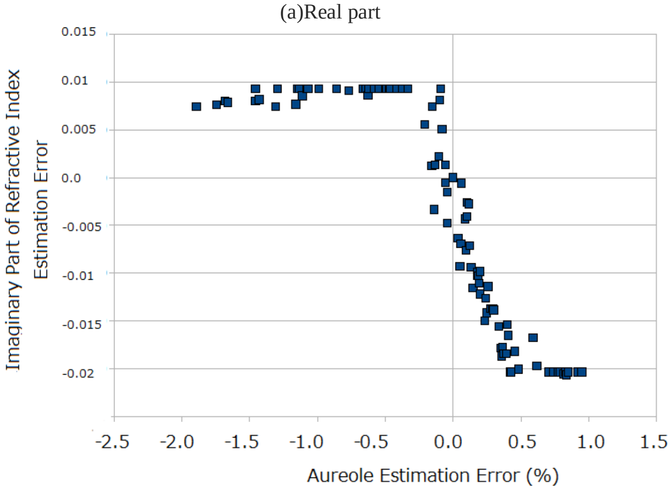

(b)Imaginary part

Fig. 8. Relation between aureole estimation error and that of refractive index.

The relation between aureole estimation error and that of real part of refractive index shows somewhat positive trend, correlation coefficient is not high though. Meanwhile, the relation between aureole estimation error and that of imaginary part of refractive index shows somewhat systematic and shows negative trend. Imaginary part of refractive index is corresponding to absorption. Therefore, negative trend of the relation is reasonable.

IV. CONCLUSION

Method for aureole estimation refinement through comparisons between observed aureole and estimated aureole based on Monte Carlo Ray Tracing: MCRT is proposed. Through some experiments, it is found that the proposed method does work for refinement of aureole estimation. The experimental results also show the proposed method is validated through comparison with empirical aureole estimation equation which is proposed by Shebrooke University research group.

Although the proposed method utilizing Monte Carlo Ray Tracing simulation shows better accuracy rather than Sky-Rad-Pack and empirical equation for shorter wavelength, the proposed method shows poorer accuracy than the conventional methods for longer wavelength. The reason for this is atmospheric optical depth is too thin.

The relation between aureole estimation error and that of real part of refractive index shows somewhat positive trend, correlation coefficient is not high though. Meanwhile, the relation between aureole estimation error and that of imaginary part of refractive index shows somewhat systematic and shows negative trend. Imaginary part of refractive index is corresponding to absorption. Therefore, negative trend of the relation is reasonable.

ACKNOWLEDGMENT

The author would like to thank Mr. Yu Odeishi for his efforts through experiments and simulations.

REFERENCES

[1] Arai K., Xing Ming Lian, aerosol refractive index and size distribution estimation usinbg solar direct and diffuse irradiance based on simulated annealing, Journal of Japan Society of Remote Sensing, 23, 2, 11-20,2003.

[2] K.Arai and Xing Ming Liang, Method for estimation of refractive index and size distribution of aerosol using direct and diffuse solar irradiance and aureole by means of simulated annealing, Advances in Space Research, Vol.32, No.11, pp.2165-2174, 2003.

[3] K.Arai and Xing Ming Liang, Method for estimation of refractive index and size distribution of aerosol using direct, diffuse and aureole by means of simulated annealing. Proceddings of the COSPAR (Committee on Space Research) Congress, p.10 (Solicited Paper), Texas, USA, Oct., 2002.

[4] K.Arai, Y.Iisasa and Xing Ming Liang, Aerosol parameter estimation with changing observation angle of ground based polarization radiometer, Proc.of the COSPAR Congress (Paris), A-00579,A3.1-0037-04, July 2004.

[5] K.Arai and Xing Ming Liang, Characterization of aerosols in Saga city areas in Japan with direct and diffuse solar irradiance and aureole observations, Proc.of the COSPAR Congress(Paris), A-00582, A1.1-0130-04, July 2004.

[6] Arai, K., Xing Ming Liang, Aerosol refractive index and size distribution estimation using solar direct and diffuse irradiance by means of nonlinear insion method, Proceedings of the 33rd General Assembly of the Japan Remote Sensing Society, 145-146, 2002.

[7] Aarai K., Xing Ming Lian, Aerosol refractive index and size distribution estimation using solar direct, aureole, and solar diffuse irradiance based on nonlinear inversion, Proceedings of the 34th General Assembly of the Japan Remote Sensing Society, 209-210, 2003.

[8] Romanov, P., Norman T.O'Neill and A.Royer, Simultaneous retrival of aerosol refactive index and particle size distribution from ground-based measurements of direct and scattered solar radiation, Applied Optics, Vol. 38, No. 36, pp.7305-7320,1999.

[9] Aarai K., Fundamental Theory on Remote Sensing, Gakujutsu-Tosho-Shuppan Publishing Co. Ltd., 2001

[10] Multispectral Remote Sensing of Earth's Atmosphere, N. Takeuchi Edt., Gakkai-Shuppan-Senta Publishing Co. Ltd., 2001.

[11] Guang-Yu Shi, Ground-based measurements of aerosol parameters, Institute of atmospheric Physics, Chinese Academy of Science, G-0063 second progress report,1998

[12] I.Lenoble, Radiative transfer in scattering and absorption atmospheres, A. DEEPAK Publishing, 1985.

[13] Shunlin liang, Quantitative remote sensing of land surface, John Wiley & Sons, Inc, 2004.

[14] Box,M.A. and A.DEEPAk, An approximation to multiple scattering in earth's atmosphere: Almucantar irradiance formulation, Journal of atmospheric science,Vol.38, pp.1037-1048,1981.

[15] eirmendjian,D., Theory of solar aureole, Part I ,application to atmospheric models, ann. Geophys., vol.15, pp.218-249,1959.

[16] McClatchey,R.A.,R.W.Fenn,J.E.A.Selby,F.E.Volz and J.S.Garing, Optical properties of the atmosphere(3rd ed.). AFCRL Envirn.Res.Papers No.411, pp108.,1972.

[17] Arai,K and Y.Minematsu, Image restoration based on maximum entropy method with parameter estimation by annealing, Journal of the Japanese photogrammetry and remote sensing society, Vol. 37, No. 2, pp.15-22,1998.

AUTHORS PROFILE

Kohei Arai, He received BS, MS and PhD degrees in 1972, 1974 and 1982, respectively. He was with The Institute for Industrial Science and Technology of the University of Tokyo from April 1974 to December 1978 also was with National Space Development Agency of Japan from January, 1979 to March, 1990. During from 1985 to 1987, he was with Canada Centre for Remote Sensing as a Post Doctoral Fellow of National Science and Engineering Research Council of Canada. He moved to Saga University as a Professor in Department of Information Science on April 1990. He was a councilor for the Aeronautics and Space related to the Technology Committee of the Ministry of Science and Technology during from 1998 to 2000. He was a councilor of Saga University for 2002 and 2003. He also was an executive councilor for the Remote Sensing Society of Japan for 2003 to 2005. He is an Adjunct Professor of University of Arizona, USA since 1998. He also is Vice Chairman of the Commission "A" of ICSU/COSPAR since 2008. He wrote 30 books and published 492 journal papers

Multifidus Muscle Volume Estimation Based on Three Dimensional Wavelet Multi Resolution Analysis: MRA with Buttocks Computer-Tomography: CT Images

Kohei Arai [1]
Graduate School of Science and Engineering
Saga University
Saga City, Japan

***Abstract*—Multi-Resolution Analysis:. MRA based edge detection algorithm is proposed for estimation of volume of multifidus muscle in the Computer Tomography: CT scanned image The volume of multifidus muscle would be a good measure for metabolic syndrome rather than internal fat from a point of view from processing complexity. The proposed measure shows 0.178 of R square which corresponds to mutual correlation between internal fat and the volume of multifidus muscle. It is also fund that R square between internal fat and the other possible measures shows smaller than that of multifidus muscle.**

***Keywords*—Edge detection; MRA; Multifidus muscle**

I. Introduction

A measure for representing metabolic syndrome based on Computer Tomography: CT value of multifidus is proposed by Professor Eguchi of Saga University. It is still difficult to treat CT value for expressing levels of metabolic syndrome. The proposed method allows representation of volume of multifidus easily by using discrete wavelet transformation. I have calculated the ratio of the subcutaneous fat CT value and this intra-abdominal fat volume, multifidus CT value / fat CT value ratio, the waist muscle CT value / fat CT value ratio. As a result, I asked that the subcutaneous fat CT value ratio of multifidus waist muscle correlates with muscle fatty.

Iinterspinous muscle, the transversospinalis muscle, etc. , multifidus of transversospinalis muscle especially susceptible to stress, it is effective in preventing the pain that occurs by stimulating the peripheral nerves of the fascia and hyperemia in psoas muscle, swelling, inflammation and. Further, to train the multifidus leads to enhancing the motor functions of the spinal column as a whole. Further, it is possible volume of multifidus can be used as an index of abdominal fat high correlation with it, to give an indication of when recovering from metabolic syndrome based on this indication. Volume of the multifidus muscle can be estimated from X-ray CT images. Further, it is also possible to obtain from 3D Discrete Cosine Transformation: DCT image directly the volume of intra-abdominal fat, the time and more effort is applied to this,

It is not possible to achieve practical processing time. Further, important method of estimating the multifidus volume by reducing the artifacts from the image obtained with a small dose in this analysis [1]-\[7]. Contour extraction method using a differential operator conventionally has been widely used for this analysis. The contours extracted by the differential operator, there are drawbacks such as low in general, the contour does not (1) intended to be extracted is more, resistance to (2) noise. Since the extracted contour by differential operator would extract the component regarded as a contour in the entire frequency range, contour unintended and would be extracted, for extracting a contour high frequency components of the noise uniformly distributed in frequency, noise immunity is low.

Determining the intra-abdominal fat volume from the abdominal CT images using the "Fat Scan." is proposed Furthermore,, to examine the relationship between intra-abdominal fat to obtain a CT value of multifidus and buttocks volume. In order to determine the relationship between the multifidus and abdominal fat, the method is performed with (Multi Resolution Analysis: MRA) 3D wavelet multi-resolution analysis and two-dimensional MRA. In order to avoid this, this paper deals with wavelet multi-resolution analysis: propose contour extraction with MRA [8],[9]. Since MRA is equivalent to the filter bank, it is possible to extract the contour of a desired frequency component. I seek the MRA up to four levels in each dimension. I determine the value of intra-abdominal fat and multifidus number of multifidus at each stage. Furthermore, I ask each of the value of intra-abdominal fat and multifidus number of multifidus performs morphological analysis after performing each MRA. The following section describes the research background and the proposed method followed by some experimental data analysis with acquired CT images of patients. Then conclusion is described together with some discussions.

II. Proposed Method

A. Moltifidus

Multifidus is a muscle that runs on inner side of the upper vertebra of "spinous process" between the "horizontal projection" and transversospinalis muscle is. I divided into

① semispinalis,
② multifidus, to
③ rotator

and further divided the transversospinalis muscle. Semispinalis spread to vertebrae of five to six. Multifidus is located deeper than the semispinalis muscle spread vertebrae three or four, as shown in Figure 1.

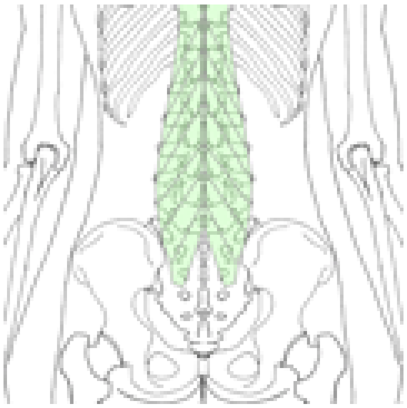

Fig. 1. Multifidus muscle

Furthermore,, rotator spread between two vertebrae from one, is located in the deepest. With the contraction of the transversus abdominis, multifidus is activated; pull the spinous process, to rotate to the other side. There is a rotation movement turn around the back, such as turning the waist. (Slope , the latter is tilted backward sacral sacrum before the former) to control the position of the sacrum, the transverse abdominal muscle contraction increases the tension of the back muscles chest film outside, iliococcygeus muscle- coccyx muscle and multifidus to increase intra-abdominal pressure to stabilize the lumbar spine by you. Furthermore, by using in conjunction with the outer unit, and increase the tension of the rear sacroiliac ligament through the chest spine film, transversus abdominis contributes to closing strengthen pelvic girdle. Load of 12 pieces of work in each facet. Is a translation of the six rotatory motion of six around XYZ axes and (Mo), along the axes. (Spinal muscle, the longest streak, iliocostalis muscle (rotator muscles, semispinalis, multifidus) erector spinae transversospinalis muscle called the intrinsic muscles of the back's move freely at will exercise the 12 interspinous muscle, is a intertransversalis,). Muscle short mileage as located in the deep, to be involved in the finer movement.

B. *Edge extraction and buttocks CT image*

Figure 2 shows an example of edge extraction Laplacian operator hip and CT images. As shown in Figure 2, the edge of the desired other than, well, there is a tendency for noise as well as to emphasize edge extracted Sobel, the Laplacian operator or the like.

C. *Wavelet Multi Resolution Analysis: MRA*

2D and 3D wavelet transformation is illustrated in Figure 3 (a) and (b), respectively. Original image can be divided into four components LL_1, LH_1, HL_1, and HH_1 where L and H denote Low frequency and High frequency components and the order of L and H is Horizontal and Vertical directions (Pixel and Line directions).

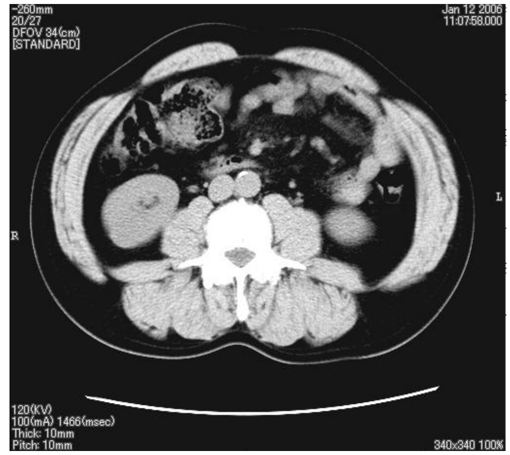

(a) Original CT image

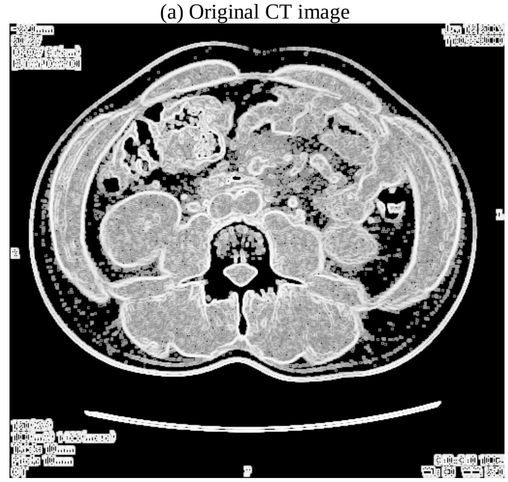

(b) Edge detected image with Laplacian operator

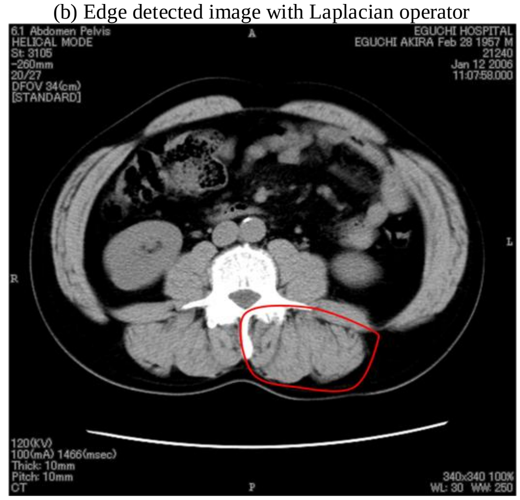

(c)Mu8ltifidus Lo9cation (red lines shows)

Fig. 2. Original image and edge detected image with Laplacian operator.

On the other hand, suffix denotes level. LL_1 component can be divided into LL_2, LH_2, HL_2, and HH_2. Furthermore, LL_2 can also be divided into LL_3, LH_3, HL_3, and HH_3. Generally, LL_n can be divided into LL_{n+1}, LH_{n+1}, HL_{n+1}, and HH_{n+1}. Importantly, original image can be reconstructed with all these components perfectly.

Meanwhile, an example of edge detected image based on 2D Multi-Resolution Analysis: MRA is shown in Figure 3(c).

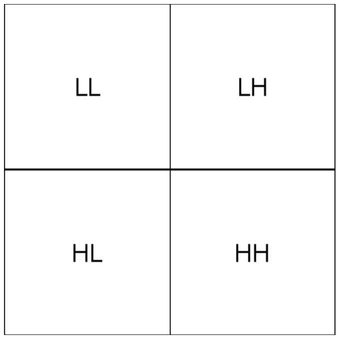

(a) 2D wavelet transformation

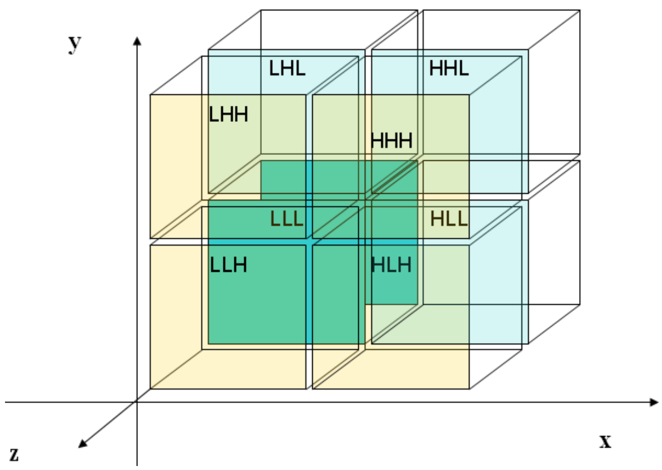

(b) 3D wavelet transformation

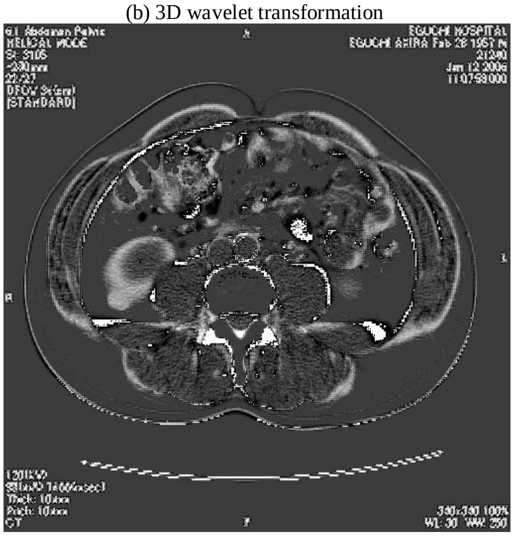

(c) An example of edge detected image based on 2D Multi-Resolution Analysis: MRA

Fig. 3. 2D and 3D wavelet transformation and an example of edge detected image based on 2D MRA

Multifidus in concern is composed with a number of ellipsoidal shapes of muscles. Therefore, string types of edges are seen at the multifidus. These edges are detected by 2D and 3D MRA. Edge is essentially high frequency components. Therefore, edges are detected by reconstructing image using LH, or HL, or HH components after MRA. If reconstruction is made with LH component only, then horizontal edges can be detected while vertical edges can be detected by reconstructing image using HL component only. Both horizontal and vertical edges can also be detected by reconstructing using HH component only. Some other combinations among LH, HL, HH are also available and useful in some cases.

III. EXPERIMENGTS

A. *Evaluation function*

It has been proposed can be an indicator of the function of the multifidus the size of the multifidus indicators proposed, it is intended that the risk of metabolic syndrome and the like and to provide a measure of the recovery degree from this. Therefore, the index is necessary that correlation between the abdominal fat is high. Body Mass Index: BMI, etc. (the ratio of the CT values of visceral fat and multifidus) fat volume, subcutaneous fat volume, waist muscle volume, multifidus volume, CT value ratio is proposed as an indicator whole:

Body Mass Index: BMI as an indicator of the traditional are. R-square value of the intra-abdominal fat is as high as among these indicators, and selects the one that can be extracted relatively easily from hip CT images. It is obtained by dividing the square of the height of the body weight, BMI can find out very easily. Obtained from buttock CT image but otherwise, CT value of the ratio can be calculated relatively easily identify the pixels if possible. Psoas volume, multifidus volume can be calculated relatively easily since only factor of the pixel if you can even contour extraction.

Specific fat cells difficulties subcutaneous fat, whole fat as well as intra-abdominal fat. Thus, by comparing the calculation result of the multifidus volume based MRA is proposed indices as correct the result of the stochastic by expert judgment indicators conventionally. These were of the proposed indicator in this paper. Judgment result of experts determined from the CT images for subjects of 362 names, up to 81 years from 25 years in Figure 4, ie, shows the relationship of the conventional index and intra-abdominal fat as a correct answer. For each of the posies muscle volume fat volume, subcutaneous fat volume, CT value ratio, and multifidus whole volume, it has become 0.408, 0.045, 0.001, 0.178, and 0.111, R-square values, correlation with overall fat volume I know that but the highest. However, since the time and effort-consuming in order to determine the volume as described above, multifidus volume obtained processing time in less relatively high R-square value is then this judgment indicative of suboptimal was Level and 3.2.

B. *Example of wavelet transformation*

Figure 4 shows examples of the original CT image, and 2D as well as 3D wavelet transformed images. Obviously, 3D wavelet transformed image has much edge related information rather than 2D wavelet.

C. *Tested People*

The following four patients are participated to the experiments,

Age: 72,63,59,41

Height(cm):Weight(kg)

164:71, 170:75, 160:76, 156:62

Body Mass Index: BMI: 26.21, 25.95, 29.69, 24.22

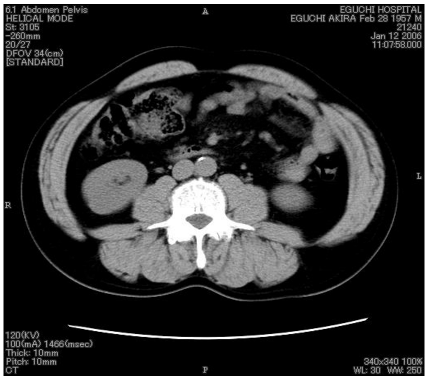

(a)Original

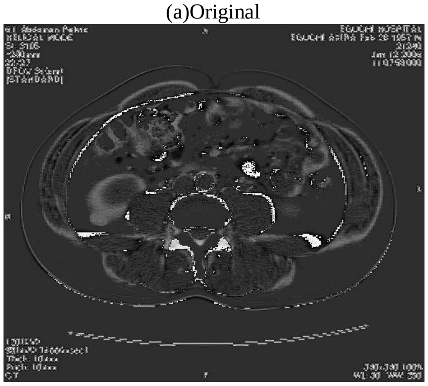

(b)2D wavfelet transformation (level 1)

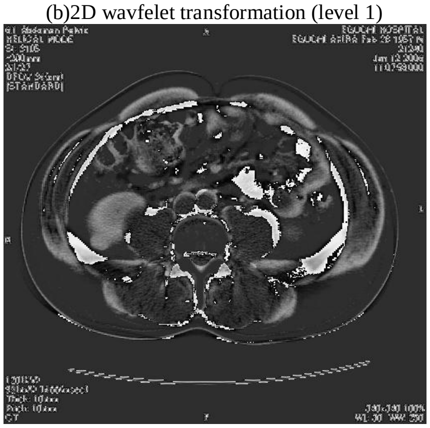

(c)3D wavelet transformation

Fig. 4. Examples of wavelet t5ransfo0rmed images

D. Process flow

In order to extract much clear edge information, pixel labeling followed by morphological filtering (dilation and erosion) is applied to the wavelet transformed images. Figure 5 shows illustrative view of pixel labeling. Meanwhile, Figure 6 shows morphological filtering.

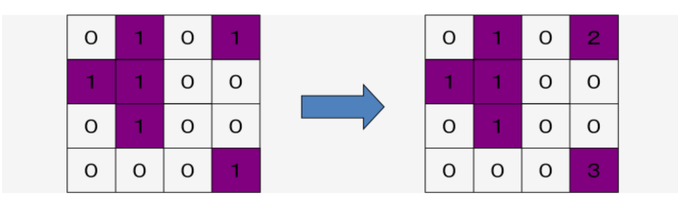

Fig. 5. Pixel labeling

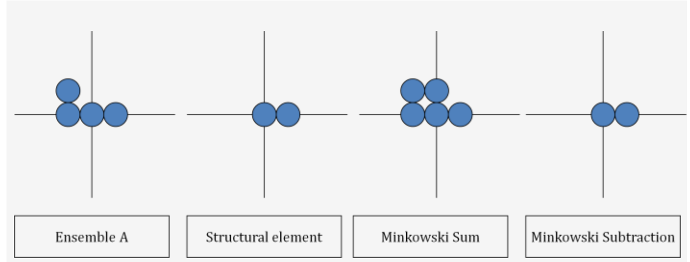

(a)Fundamentals

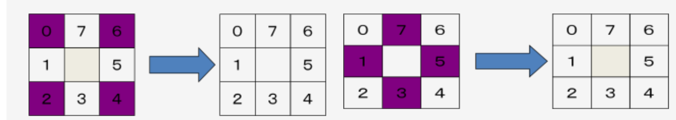

(b)Dilation (c)Erosion

Fig. 6. Morphological filtering

E. MRA basis function

Using the Daubechies and Haar as a basis function, is subjected to MRA for the buttocks CT image by changing to level 1, 2, 3, and 4, we attempted to outline extraction of multifidus. It is shown in Figure 5 an example of the result. (a), (b), (c) is a rump CT original image at different sites, respectively. (d), (e), (f) is a contour image reconstructed except for the LL component 2DMRA at two levels. (g), (h), (i) is a contour image reconstructed with the exception of the LLL component of 3DMRA in level 2. It is as 1 Table to extract the contour from the contour image that is obtained in this manner, to examine the R -square value of the intra-abdominal fat volume by calculating the (number of pixels ie) multifidus volume was found. That is, the difference between R-square value by the base functions is hardly observed, levels for specifying the frequency contour is found that 2 or, 3 is good.

TABLE I. R-SQUARE VALUE BETWEEN STOMACH FAT AND VOLUME OF MULTIFIDUS MUSCLE ESTIMATED THROUGH MRA WITH 1-4 LEVELS

Level	1	2	3	4
Haar	0.160	0.175	0.177	0.169
Duabechies	0.162	0.178	0.178	0.172

F. Experimental Results

Figure 7 shows examples of edge detected images through reconstruction without LL component (2D MRA) and LLL (3D MRA) from 1 to 4 levels of the wavelet transformed images.(a), (b) and (c) are original CT images at the different height (portion). (d), (e) and (f) are edge detected images reconstructed without LL component. (g), (h) and (i) are edge detected images reconstructed without LLL component.

Meanwhile, Figure 8 shows relations between stomach fat and the other measured factors.

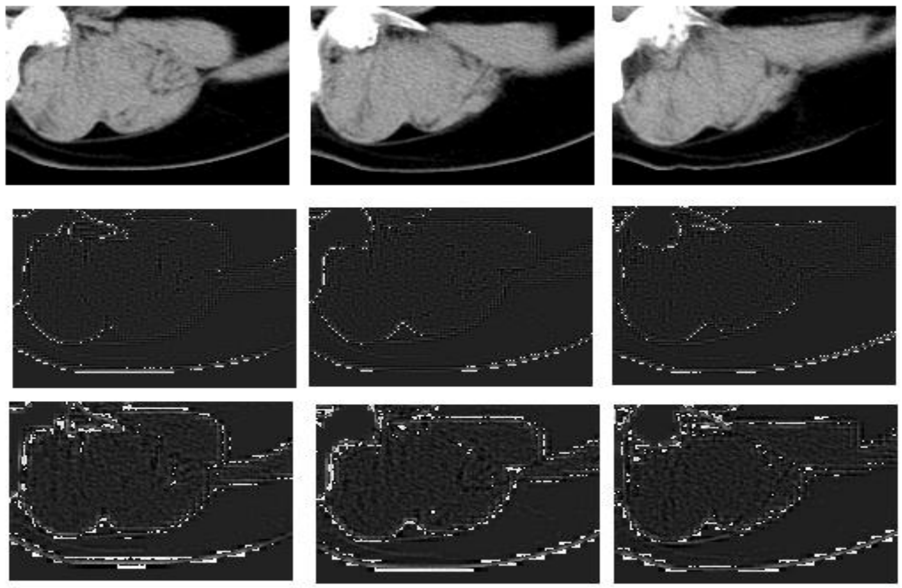

(a)2D wavelet transformed images

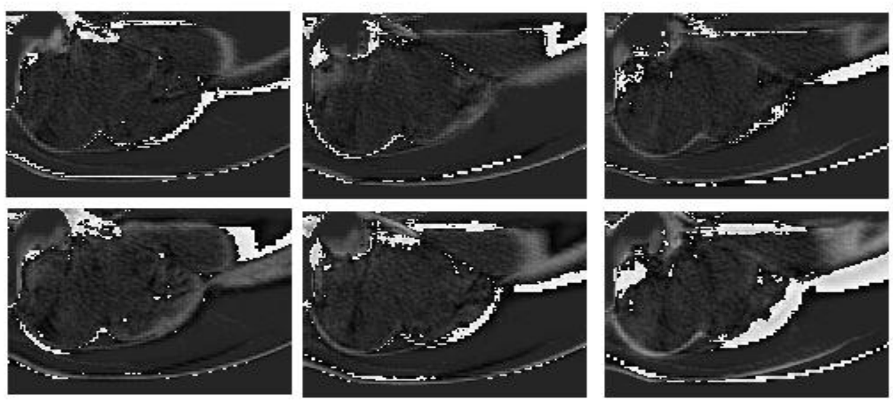

(b)3D wavelet transformed images

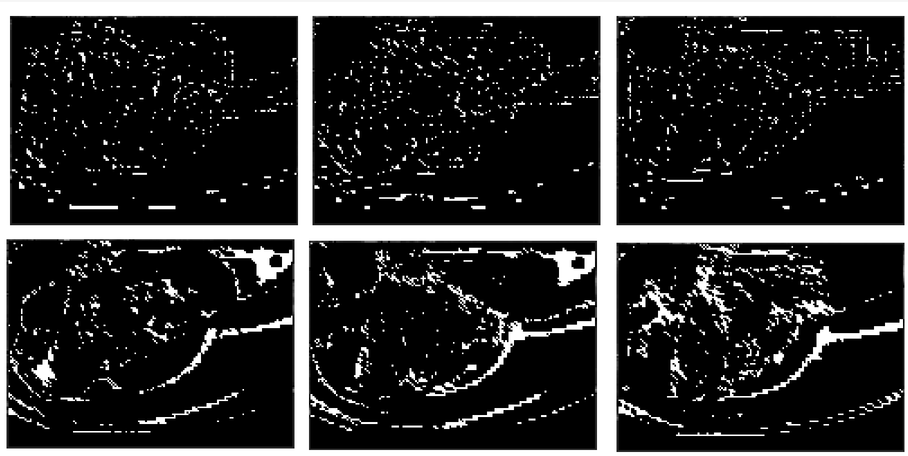

(c)After morphological filteringt

Fig. 7. Examples of edge detected images through reconstruction without LL component (2D MRA) and LLL (3D MRA) from 1 to 4 levels of the wavelet transformed images.(a), (b) and (c) are original CT images at the different height (portion). (d), (e) and (f) are edge detected images reconstructed without LL component. (g), (h) and (i) are edge detected images reconstructed without LLL component.

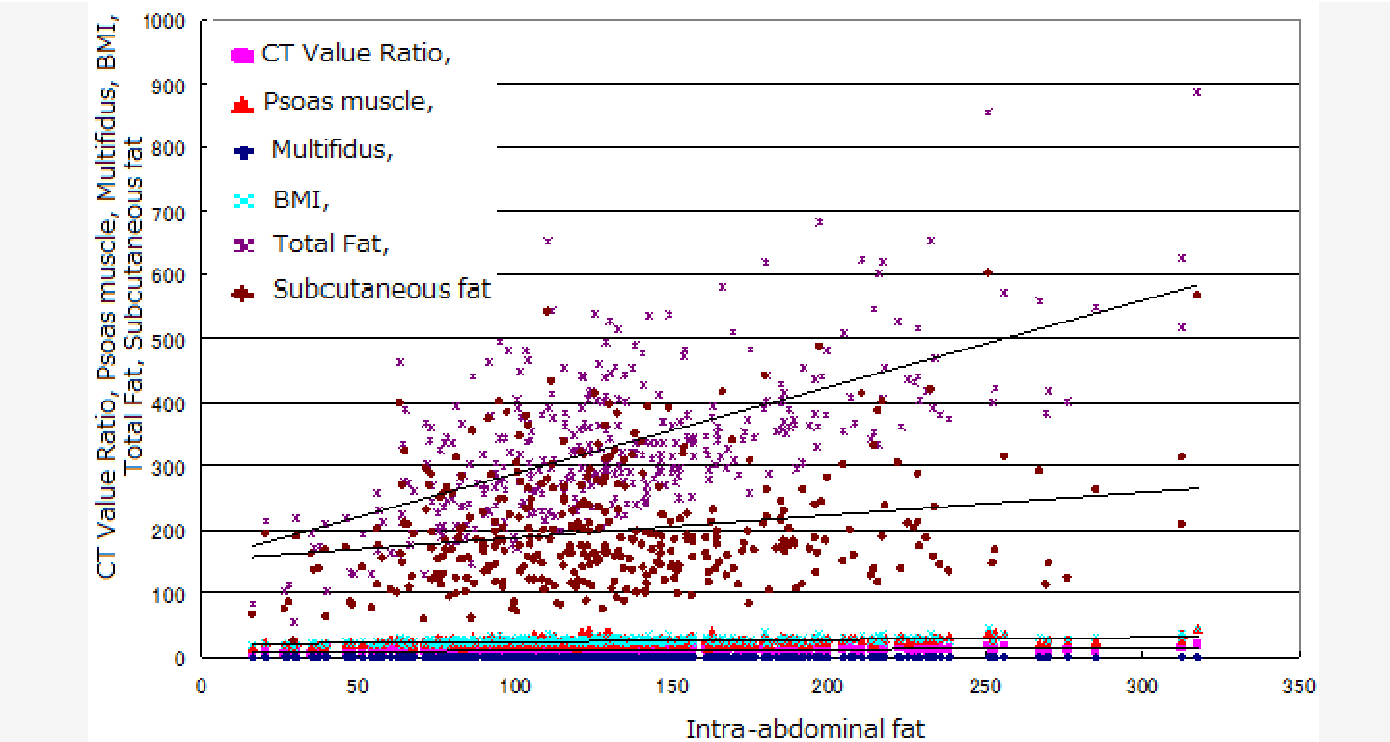

Fig. 8. Relations between stomach fat and the other measured factors

For intra-abdominal fat and multifidus volume, an increase of intra-abdominal fat is observed volume of the multifidus muscle is reduced. It is also found that multifidus adipose CT value ratio increases with increasing of abdominal fat.

If you look at the value of intra-abdominal fat and number of multifidus on the basis of the value of intra-abdominal fat and CT value ratio, these are not seen feature in both 2D DWT, 3D DWT of each stage when you do not subjected to morphological analysis. It is believed that unchanged edges of multifidus are observed in a certain value in order to present numerous. However, if you have applied twice morphological analysis, for the closing and closing, 3D DWT case shows much better relation between intra-abdominal fat and multifidus volume than the 2DW cases.

In particular, it can be obtained a high value by performing a two-step MRA of 3D DWT, is applied twice closing. Furthermore, since it is the result of as if they are subjected twice when closing subjected three times more than the closing, closing it is found that it may be subjected to two times.

Although not observed in the characteristic value if 2 times erosion together with dilation. This is presumably because the edges of the multifidus should not lead. By performing two times until dilation are captured

IV. Conclusion

It is found that multifidus volume of intra-abdominal fat can be estimated with CT image through 3D wavelet transformation much clearly than 2D wavelet transformation. Traditionally, although intra-abdominal fat can be estimated with CT value, it is found that the relation between CT value and intra-abdominal fat is not so high. Meanwhile, relation between intra-abdominal fat and total fat is obviously high followed by subcutaneous fat, multifidus, BMI, psoas muscle,and CT value ratio. Therefore, multifidus volume can be an indicator of intra-abdominal fat. Because of 3D wavelet MRA allows estimation of multifidus volume, it is useful for measure intra-abdominal fat with CT image derived multifidus volume.

Acknowledgment

The author would like to express a sincere gratitude to Professor Dr. Eguchi Yuichiro of the Faculty of Medicine in Saga University for his courtesy the data subject at the beginning of this study. Furthermore, author also would like to thank Mr. Mitsuo Mochida for his cooperation through experiment.

References

[1] CT Performance Evaluation Committee : Standard for Performance Evaluation of X-ray computer tomography apparatus (second recommendation) , the Japan Medical Association Journal , 88 (8) ,759 -771, 1998.

[2] Technical Committee X-ray CT system performance evaluation study group : Standard for X-ray CT system performance evaluation (draft) , Nippo technology magazine Science , 47 (1) ,56 -63 , (1991)

[3] Suzuki Kenji other technical problem of helical CT system , Nippo skill science magazine , 52 (3) 384 -388 (1996)

[4] TSUJIOKA Katsumi : Nippo skill science magazine , operation - and the actual technical problems - performance evaluation of helical CT system , 52 (3) ,389 -396 (1996)

[5] Muramatsu, Tadashi Hisashi other basic performance of helical scan CT, Nippo skill science magazine , 52 (1) ,81 -85 (1996)

[6] Keiko Kubota other applications of helical scan in the base of the brain , Nippo skill science magazine , 52 (9) , 1066 , (1996)

[7] other Shun Kuwahara Sada : performance evaluation of HiSpeed AdvantageRp, ,56,51-58 (1996) technology magazine -release north

[8] Kohei Arai : basic theory of wavelet analysis , Morikita publication (2000)

[9] Kohei Arai : self-study wavelet analysis , modern science , Inc. (2006)

AUTHORS PROFILE

Kohei Arai, He received BS, MS and PhD degrees in 1972, 1974 and 1982, respectively. He was with The Institute for Industrial Science and Technology of the University of Tokyo from April 1974 to December 1978 also was with National Space Development Agency of Japan from January, 1979 to March, 1990. During from 1985 to 1987, he was with Canada Centre for Remote Sensing as a Post Doctoral Fellow of National Science and Engineering Research Council of Canada. He moved to Saga University as a Professor in Department of Information Science on April 1990. He was a councilor for the Aeronautics and Space related to the Technology Committee of the Ministry of Science and Technology during from 1998 to 2000. He was a councilor of Saga University for 2002 and 2003. He also was an executive councilor for the Remote Sensing Society of Japan for 2003 to 2005. He is an Adjunct Professor of University of Arizona, USA since 1998. He also is Vice Chairman of the Commission "A" of ICSU/COSPAR since 2008. He wrote 30 books and published 472 journal papers

Discrimination Method between Prolate and Oblate Shapes of Leaves Based on Polarization Characteristics Measured with Polarization Film Attached Cameras

Kohei Arai [1]
Graduate School of Science and Engineering
Saga University
Saga City, Japan

***Abstract*—Method for discrimination between prolate and oblate shapes of leaves based on polarization characteristics is proposed Method for investigation of polarization characteristics of leaves by means of Monte Carlo Ray Tracing: MCRT is also proposed. Validity of the proposed discrimination method is confirmed with MCRT simulations. Also field experiments are conducted. Through field experiments at the tea estates situated in Saga prefecture, a validity of the proposed method is confirmed. Also discrimination between prolate and oblate shapes of leaves is attempted. The results show that the proposed method is valid and discrimination can be performed.**

***Keywords*—polarization; Monte Carlo Ray Tracing; prolate and oblate shapes of leaves**

I. INTRODUCTION

Plant identification is very complex and required an appropriate background with significant experience. Also the number of researchers who can identify medicinal plants is very limited. Generally, identification process of medicinal plants has been done manually by a herbarium taxonomist using guidebook of taxonomy/dendrology. The proposed method is designed to help taxonomist to identify leaf medicinal plant automatically using a computer aided system.

In particular, it would be better to identify leaves by using airborne based radiometer data Although spectral reflectance can be estimated with the radiometer data, it is difficult to identify the leaves in concern by using only the spectral reflectance. The method proposed here is to use spectral polarization camera or radiometer. It is obvious that polarization characteristics are different between needle leaves and broad leaves [1]-[10]. Therefore, it may be possible to identify the leaves in concern based on the polarization characteristics.

There is another strong demand to discriminate between vertically standing leaves and horizontally laying leaves. For instance, new borne and young leaves are vertically standing leaves while elder leaves are horizontally laying leaves. In order to determine the most appropriate harvesting timing for tealeaves, such the discrimination is needed. Spectral characteristics between both young and elderly tealeaves are not so easy to discriminate. Obviously, although Bi-Directional Reflectance Distribution Function: BRDF are different between young and elderly tealeaves [5], it does costly for measurement. Therefore, the proposed discrimination method with polarization characteristics measurements is useful. It is effective and relatively easy as well as comparatively cheap. Only instrument required for this is cheap camera with polarization film.

As the first step, the method which allows discriminate needle leaves and broad leaves is proposed. The proposed method is also possible to distinguish between prolate and oblate shapes of leaves even if the size and scale of the leaves in concern are same.

The following section describes the proposed method and system including basic concept of the proposed method, scientific background together with Monte Carlo Ray Tracing: MCRT simulation method for validation of the proposed method [2],[7],[9]. Then simulation results and field experiment results are described followed by conclusion with some discussions.

II. PROPOSED METHOD AND SYSTEM

A. Proposed System

Only thing required for the proposed system is polarization film attached camera. Major specification of the camera Cannon S-100 used for the experiment is shown in Table 1.

TABLE I. MAJOR SPECIFICATION OF S-100

Resolution	13.3million
Detector	CMOS
F_No.	2-5.9
Shutter_Speed	1-1/2000
Sensitivity	ISO80-6400
Focal_Length	30mm

At the optical entrance of the camera, polarization film has to be attached. The camera has to be set-up at the relatively high pole or tower. Most of farm areas have lighting poles or fan attached tower for air convections for avoidance from the frosting damage. In particular, tea farm areas have fan attached poles with electricity supply. Therefore, the camera can be amounted on at a high position. The recommendable observation angle is 55 degrees. Tealeaves surface is used to be covered with oily materials and water. In order to acquire their polarization characteristics, Brewstar angle between air and water or oily materials (55 degrees) is recommendable. Camera acquired data can be transferred through WiFi or wireless LAN communication links. Figure 1 shows the proposed system.

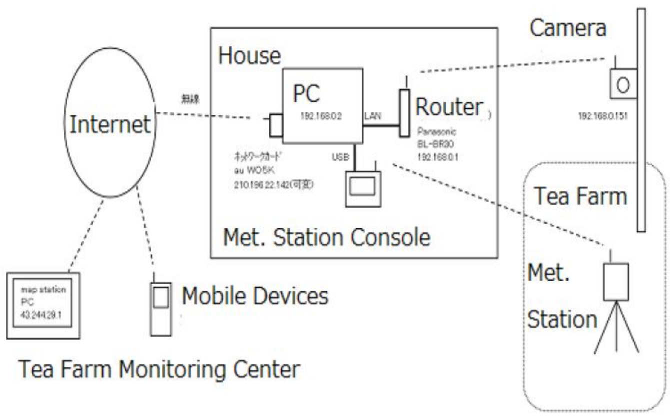

Fig. 1. Proposed system with polarization film attached camera mounted on the relatively high position which allows look down the farm area with 55 degree of Brewstar angle.

Proposed system consists of the polarization film attached camera mounted on the relatively high position which allows look down the farm area with 55 degree of Brewstar angle and meteorological station. Camera data and meteorological data are gathered through WiFi or wireless LAN communication links at farmers' houses and the farm area monitoring center through Internet

B. Process Flow

The proposed method in this paper uses polarization radiometer data of leaves in concern which is acquired with airborne based polarization radiometer. p and s polarization of reflectance of the leaves in concern is observed. Then Degree of Polarization: DP which is represented as equation (1) is calculated.

$$DP=(Rp-Rs)/(Rp+Rs) \quad (1)$$

where Rp and Rs denote surface reflectance for p polarization and that for s polarization, respectively. DP depends on the shape of leaves in concern obviously.

Therefore, discrimination between prolate and oblate shapes of leaves as well as distinguishes between needle leaf and broad leaf becomes available results in identification of medicinal leaves. In order to validate the proposed method, simulation study with Monte Carlo Ray Tracing model is conducted together with field experiments.

C. Monte CarloRay Tracing Simulation

In order to validate the proposed method, MCRT simulation study and field experimental study is conducted. MCRT allows simulation of polarization characteristics of sea surface with designated parameters of the atmospheric conditions and sea surface and sea water conditions. Illustrative view of MCRT is shown in Figure 2. Photon from the sun is input from the top of the atmosphere (the top of the simulation cell). Travel length of the photon is calculated with optical depth of the atmospheric molecule and that of aerosol. There are two components in the atmosphere; molecule and aerosol particles while three are also two components, water and particles; suspended solid and phytoplankton in the ocean. When the photon meets molecule or aerosol (the meeting probability with molecule and aerosol depends on their optical depth), then the photon scattered in accordance with scattering properties of molecule and aerosol.

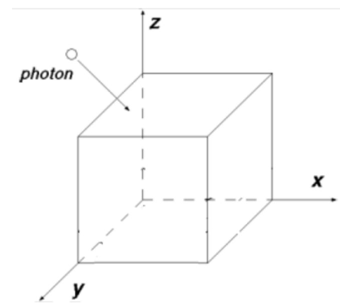

Fig. 2. Illustrative view of MCRT for the atmosphere and sea water

The scattering property is called as phase function[1]. In the visible to near infrared wavelength region, the scattering by molecule is followed by Rayleigh scattering law [11] while that by aerosol is followed by Mie scattering law [11]. Example of phase function of Mie scattering is shown in Figure 3 (a) while that of Rayleigh scattering is shown in Figure 3 (b).

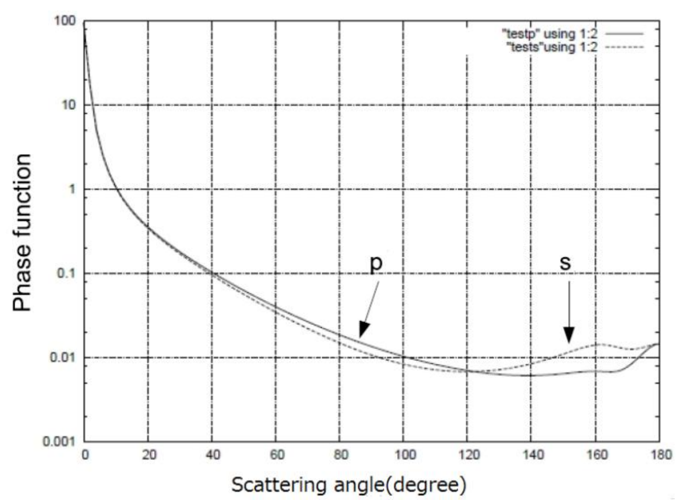

(a)Mie scattering (aerosol)

[1] http://ejje.weblio.jp/content/phase+function

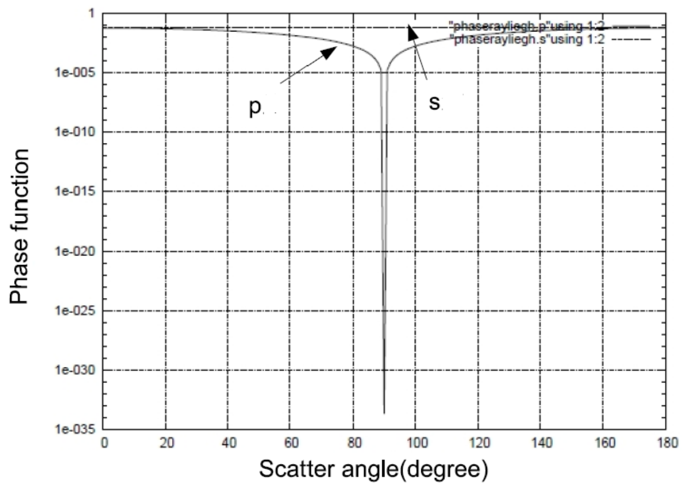

(b)Rayleigh scattering (Molecule)

Fig. 3. Phase functions for Mie and Rayleigh scattering

In the atmosphere, there are absorption due to water vapor, ozone and aerosols together with scattering due to the atmospheric molecules, aerosols. Atmospheric Optical Depth: AOD (optical thickness) in total, Optical Depth: OD due to water vapor (H2O), ozone (O3), molecules (MOL), aerosols (AER), and real observed OD (OBS) are plotted in Figure 4 as an example.

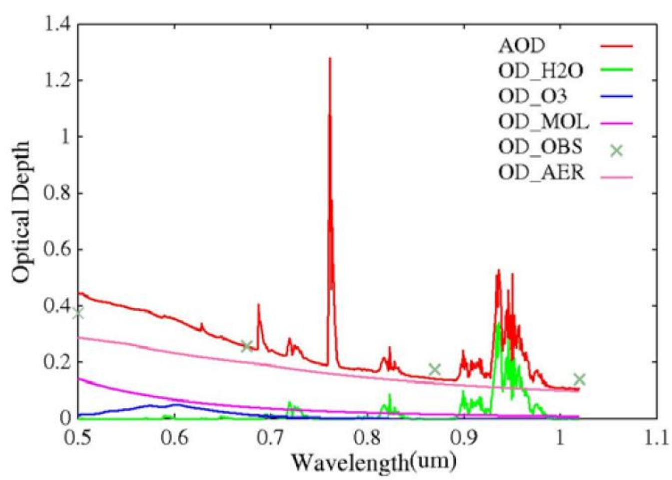

Fig. 4. Example of observed atmospheric optical depth in total and the best fit curves of optical depth due to water vapor, ozone, molecules, and aerosols calculated with MODTRAN of atmospheric radiative transfer software code..

For simplifying the calculations of the atmospheric influences, it is assumed that the atmosphere containing only molecules and aerosols. As shown in Figure 4, this assumption is not so bad. Thus the travel length of the photon at once, L is expressed with equation (2).

$$L = L0 \, \mathrm{RND}(i) \tag{2}$$
$$L0 = Zmax/\tau \tag{3}$$

where $Zmax$, τ, RND(i) are maximum length, altitude of the atmosphere, optical depth, and i-th random number, respectively. In this equation, τ is optical depth of molecule or aerosol. The photon meets molecule when the random number is greater than τ. Meanwhile, if the random number is less than τ, then the photon meats aerosol. The photon is scattered at the molecule or aerosol to the direction which is determined with the aforementioned phase function and with the rest of the travel length of the photon.

D. Ground Surface with Slopes

When the photon reaches on the ground, the photon reflects at the ground surface to the direction which is determined by random number. Lambertian surface [11] is assumed. Therefore, reflectance is constant for all the directions (from all the aspects). The reflected photon travels with the rest of travel length. Flat Lambertian surfaces are assumed.

E. Top of the Atmosphere: TOA Radiance Calculation

If the photon reaches on the wall of the simulation cell, the photon disappears at the wall and it appears from the corresponding position on the opposite side wall. Then it travels with the rest of travel length. Eventually, the photons which are reached at the top of the atmosphere are gathered with the Instantaneous Field of View: IFOV of the Visible to Near Infrared Radiometer: VNIR onboard satellite. At sensor radiance, I+ with direction and IFOV of μ, $\mu 0$ can be calculated with equation (4)

$$I+(\mu, \mu 0) = I \, N+(\mu, \mu 0)/Ntotal \tag{4}$$

where $N+$ is the number of photons which are gathered by VNIR, $Ntotal$ denotes the number of photons input to the simulation cell. Also I denotes extraterrestrial irradiance at the top of the atmosphere.

F. Leaf Surface Model

Prolate and oblate shapes of leaf surface models are created as shown in Figure 5.

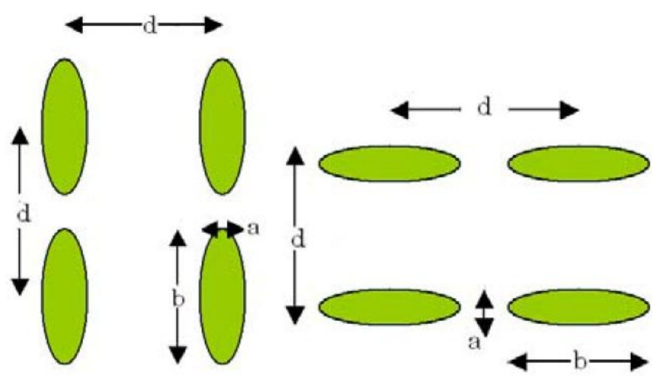

Fig. 5. Prolate and oblate shapes of leaf surface models

These leaves are aligned with d of interval. New borne and young tealeaves are vertically standing leaves while elder tealeaves are horizontally laying leaves. Prolate leaves are assumed to be new borne and relatively young tealeaves while oblate leaves are also assumed to be comparatively well grown elderly tealeaves. The surfaces of the prolate and oblate leaves are modeled with Lambertian surface. The reflectance of the leaves is determined by empirical models. In order to determine the most appropriate harvesting timing for tealeaves, such the discrimination is needed.

III. SIMULATION AND EXPERIMENTAL RESULTS

A. Simulation Results with MCRT

MCRT based simulation is conducted for p and s polarizations individually. The sizes of prolate and oblate shapes of tealeaves are ranged from 5 cm to 20 cm with 5 cm step. 10 million of photons are input to the atmosphere with optical depth of 0.15 for aerosols and 0.3 for atmospheric molecules at the wavelength of 500 nm as well as 0.2 for atmospheric molecules and 0.02 for aerosols at the 730 nm. The reflectance of the tealeaves are set at 0.215 for p polarization and 0.46 for s polarization in the case of oblate shape while 0.22 for p polarization and 0.21 for s polarization in the case of prolate shape), respectively. The reflectance is provided by Grant, L. (Polarized and non-polarized components of leaf reflectance, Doctoral Dissertation, Purdue University, 1985).

Figure 6 shows the number of photons reached at the top of the atmosphere at the wavelength of 730 nm.

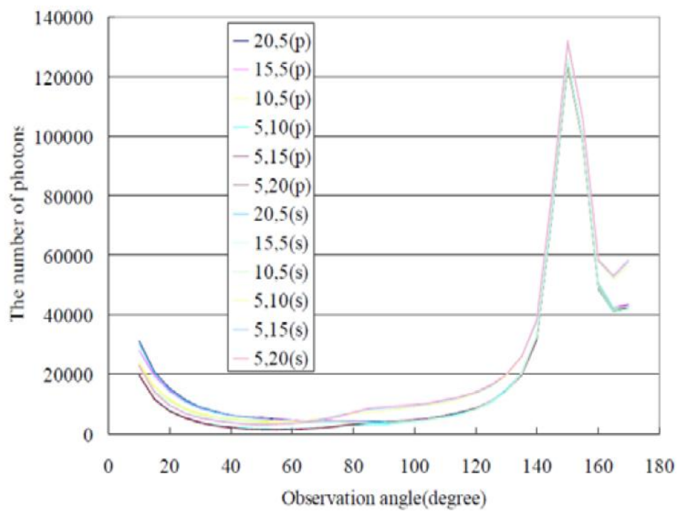

Fig. 6. Example of MCRT simulation results of the number of photons reached at the top of the atmosphere at the wavelength of 730 nm.

Although it is not clear the differences, DP which is shown in Figure 7 shows clear difference between prolate and oblate shapes of tealeaves.

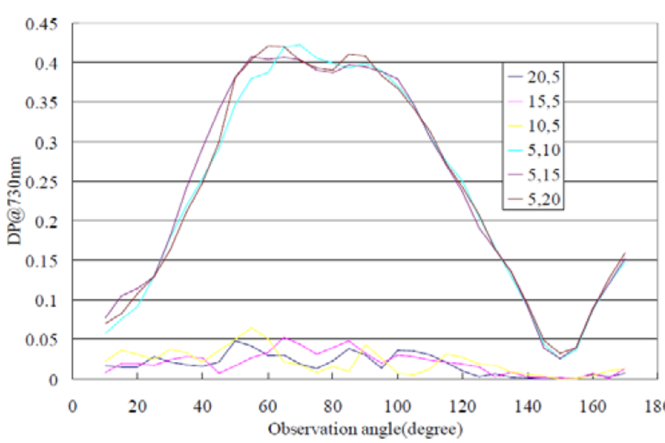

Fig. 7. DP calculated for prolate and oblate shapes of tealeaves at 730 nm

Meanwhile, the reflectance of the tealeaves is 0.1 for p polarization and 0.5 for s polarization for prolate shape while 0.08 for p polarization and 0.21 for s polarization for oblate shape at the wavelength of 550 nm, respectively. MCRT results for 550 nm which is shown in Figure 8 shows almost twice much DP in comparison to those for 730 nm.

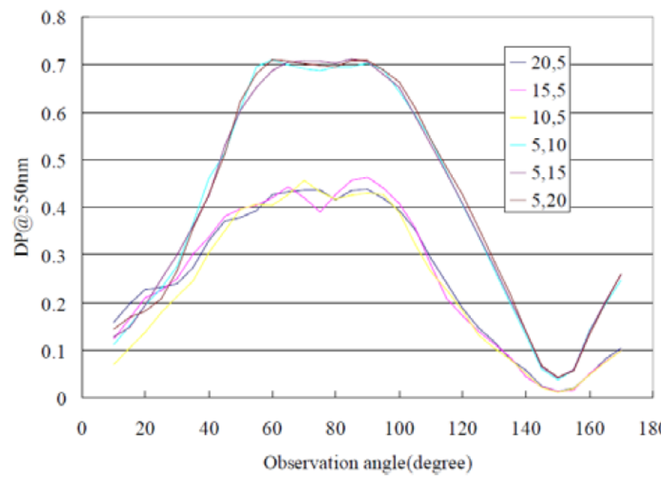

Fig. 8. DP calculated for prolate and oblate shapes of tealeaves at 550 nm

It is clearly found that the calculated DPs for prolate and oblate shapes of tealeaves are quite different. Approximately twice much DP is shown for prolate shape of tealeaves in comparison to the DP for oblate shape of tealeaves. Therefore, it is possible to discriminate between prolate and oblate shapes of tealeaves.

B. Experimental Results at Saga Prefectural Tea Institute

Field experiments are conducted at the Saga Prefectural Tea Institute: SPTI situated at 33:07:03.9 N, 129:59:47.0 E on June 1 2008. The first harvesting is finished in the begging of May. After the harvesting of tealeaves, the top tea trees are used to be cut out. Then new tealeaves appear after that. June 1 is middle moment between the first and the second harvests. There are four tea farm areas which are situated North, East, South, and West sides of the SPTI main building as shown in Figure 9.

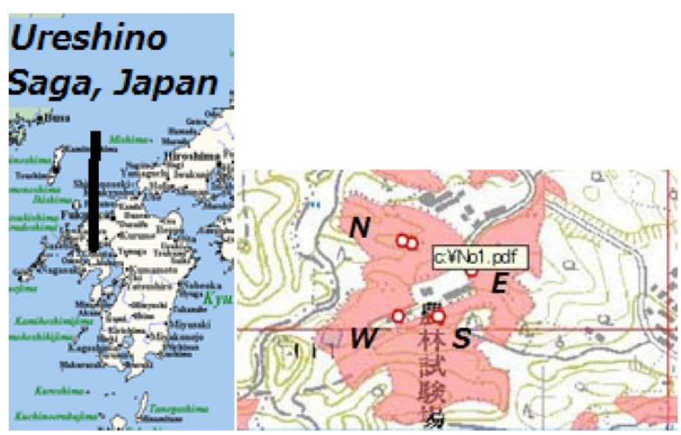

Fig. 9. Tea farm areas in concern situated at SPTI 33:07:03.9 N, 129:59:47.0 E

Figure 10 (a) shows an example of camera monitor images of north tea farm area of SPTI acquired with the proposed tea farm area monitoring system. There are fan mounted poles as shown in Figure 10 (a). The polarization film attached camera is attached to the fan pole. Figure 10 (b) also shows same example image displayed onto mobile phone. Therefore, tea farmers can take a look at their farm area with their mobile phone. Figure 10 (c) shows an example of meteorological data displayed onto mobile phone as well.

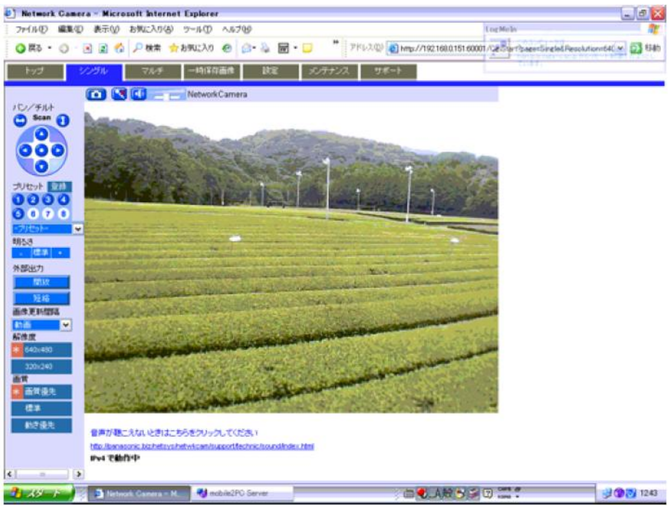

(a)

(b)

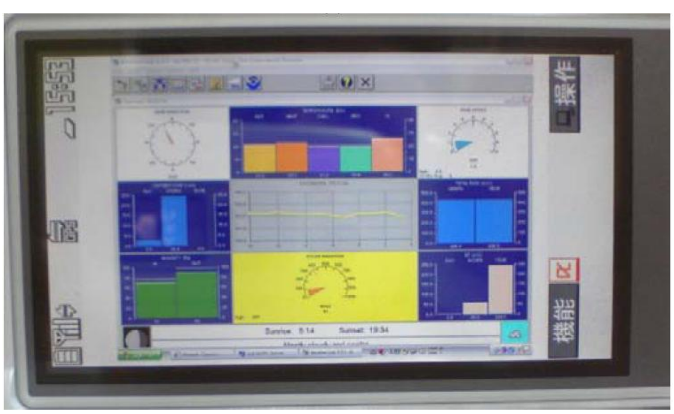

(c)

Fig. 10. Examples of photos of the tea farm area of SPTI and meteorological data which area situated at just beside the tea farm areas

Figure 11 shows top view of the tealeaves at the four different tea farm areas together with the grass situated at just beside of east tea farm area. Although it is hard to distinguish among these visually, reflectance in near infrared wavelength region of tealeaves is different each other as shown in Figure 12. Figure 12 also shows not only spectral reflectance but also calculated spectral DP. In this case, spectral DP is measured with spectral radiometer of MS-720 manufactured by Eiko Co. Ltd, Japan. Major specification of MS-720 is shown in Table 2.

TABLE II. MAJOR SPECIFICATION OF MS-720

Wavelength_coverage	350 ~ 1,050nm
Wavelength_Interval	3.3nm
Wavelength_Resolution	10nm
Wavelength_accuracy	Less_than_0.3nm
Aperture_angle	180°
Stray_light	Less_than_0.15%
Temperature_dependency	±5%

(a)East(Yabukita) (b)South(Ohiwase)

(c)West(Benifuki) (d)North(Yabukita)

(e)Grass in East Tea Farm Area

Fig. 11. Top views of tealeaves of the tea farm areas of SPTI. Bracket indicates species of the tealeaves

Only the reflectance of the leaves at the wavelength of 550 and 730 nm are given by Grant. Although the reflectance at are similar.

Figure 12 Measured spectral reflectance and DP at tea farm areas which are situated at north, east, south and west tea farm areas of SPTI. Much appropriate wavelengths for discrimination of prolate and oblate shapes of tealeaves are

500 nm, 675 nm and 800 nm as shown in Table 3. As shown in Table 3, DP of the grass is always small in comparison to the others. On the other hand, DP of the tealeaves at north tea farm area and that at east tea farm area shows specific features.

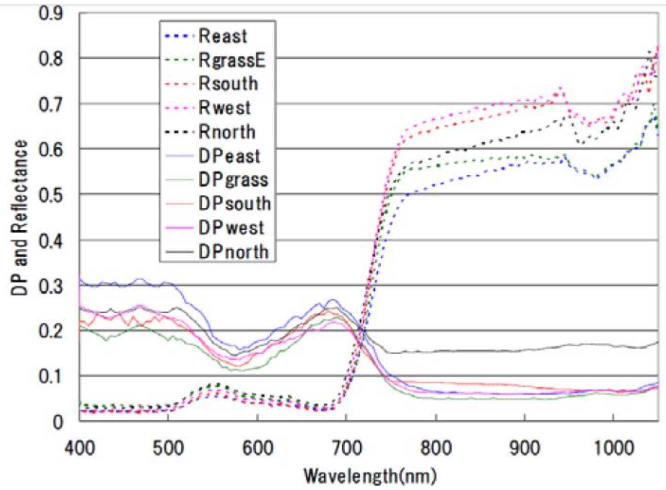

Fig. 12. Measured spectral reflectance and DP at tea farm areas which are situated at north, east, south and west tea farm areas of SPTI

TABLE III. DP CALCULATED WITH MEASURED SPECTRAL P AND S POLARIZED REFLECTANCE AT EAST,WEST, SOUTH AND NORTH TEA FARM AREAS AS WELL ASGGRASS SITUATED JUST BESIDE THE EAST TEA FARM AREA ON JUNE 1 2008

Wavelength(nm)	East	West	South	North	Grass
500	0.3	0.23	0.23	0.24	0.19
675	0.288	0.286	0.218	0.288	0.18
800	0.08	0.09	0.09	0.16	0.05

Namely, DP of the tealeaves at east tea farm area is quite large in comparison to the others while DP of the tealeaves at north tea farm area shows also remarkably large comparing to the others. Sizes and shapes as well as grow up rates of tealeaves are different from each other species, obviously. Both species of east and north tea farm areas are same, Yabukita. In the begging of July, just two weeks later of field experiments, the second tealeaves harvest is conducted. Best harvesting time periods are different by species by species, farm area by farm area. Measured DP would be useful to determine best harvesting time period.

IV. CONCLUSION

Method for discrimination between prolate and oblate shapes of leaves based on polarization characteristics is proposed Method for investigation of polarization characteristics of leaves by means of Monte Carlo Ray Tracing: MCRT is also proposed. Validity of the proposed discrimination method is confirmed with MCRT simulations. Also field experiments are conducted. Through field experiments at the tea estates situated in Saga prefecture, a validity of the proposed method is confirmed. Also discrimination between prolate and oblate shapes of leaves is attempted. The results show that the proposed method is valid and discrimination can be performed. As the results from simulation study and field experiments, it is found that the proposed method is useful for tealeaves harvesting time period. It also can be used validated. The proposed tea farm area monitoring system does works well. Tea farmers may take a look at their farm area with their mobile phone together with meteorological data.

ACKNOWLEDGMENT

The author would like to thank Dr. Hideo Miyazaki and Mr. Masayuki Akaishi of SPTI and Ms. Long Li Li for their effort to conduct field experiments

REFERENCES

[1] Kohei Arai, Y.Iisaka and X.Linag, Aerosol parameter estimation with changing observation angle of hround based polarization radiometer, Advances in Space Research, 39, 1, 28-31, 2007

[2] Ding Ya Liu, Kohei Arai, Forest parameter estimation based on radiative transfer model of Monte Carlo Simulation taking into account crown closer models, Journal of Japan Society of Remote Sensing, 27、2、141-152、2007

[3] Yaliu Ding, Kohei Arai, Forest parameter estimation, by means of Monte- Carlo simulations with experimental consideration of estimation of multiple reflections among trees depending on forest parameters, Advances in Space Research, 43, 3, 438-447, 2009.

[4] Kohei Arai and Yui Nishimura, Polarization model for discrimination of broad and needle shaped leaves and estimation of LAI using polarization measurements, Advances in Space Research, 44, 510-516, 2009.

[5] Kohei Arai, Method for estimation of grow index of tealeaves based on Bi- Directional reflectance function: BRDF measurements with ground based network cameras, International Journal of Applied Science, 2, 2, 52-62, 2011.

[6] Kohei Arai, Method for estimation of total nitrogen and fiber contents in tealeaves with ground based network cameras, International Journal of Applied Science, 2, 2, 21-30, 2011.

[7] K.Arai, Monte Carlo ray tracing simulation for bi-directional reflectance distribution function and grow index of tealeaves estimations, International Journal of Research and Review on Computer Science, 2, 6, 1313-1318, 2012.

[8] K.Arai, Fractal model based tea tree and tealeaves model for estimation of well opened tealeaf ratio which is useful to determine tealeaf harvesting timing, International Journal of Research and Review on Computer Science, 3, 3, 1628-1632, 2012.

[9] K.Arai, Y.Terayama, Monte Carlo ray tracing simulation of polarization characteristics of sea water which contains spherical and non-spherical shapes of suspended solid and phytoplankton, International Journal of Advanced Computer Science and Applications, 3, 6, 85-89, 2012.

[10] Kohei Arai, Hideo Miyazaki, Masayuki Akaishi, Determination method for tealeaves harvesting with visible to near infrared cameras, Journal of Japanese Society for Remote Sensing and Photogrammetry 51, 1, 38-45, 2012

[11] Kohei Arai, Lecture note on Remote Sensing, Morikita Shuppan Publishing Co. Ltd., 2001.

AUTHORS PROFILE

Kohei Arai, He received BS, MS and PhD degrees in 1972, 1974 and 1982, respectively. He was with The Institute for Industrial Science and Technology of the University of Tokyo from April 1974 to December 1978 also was with National Space Development Agency of Japan from January, 1979 to March, 1990. During from 1985 to 1987, he was with Canada Centre for Remote Sensing as a Post Doctoral Fellow of National Science and Engineering Research Council of Canada. He moved to Saga University as a Professor in Department of Information Science on April 1990. He was a councilor for the Aeronautics and Space related to the Technology Committee of the Ministry of Science and Technology during from 1998 to 2000. He was a councilor of Saga University for 2002 and 2003. He also was an executive councilor for the Remote Sensing Society of Japan for 2003 to 2005. He is an Adjunct Professor of University of Arizona, USA since 1998. He also is Vice Chairman of the Commission "A" of ICSU/COSPAR since 2008. He wrote 30 books and published 322 journal papers.

Experimental Approach of Reflectance Based Vicarious Calibration Method for Solar Reflectance Wavelength Region of Sensor Onboard Remote Sensing Satellites

Kohei Arai [1]
Graduate School of Science and Engineering
Saga University
Saga City, Japan

***Abstract*—Experimental approach of reflectance based vicarious calibration of solar reflectance wavelength region of mission instruments onboard remote sensing satellites is conducted. As an example, vicarious calibration of ASTER/VNIR with estimated aerosol refractive index and size distribution that depends on atmospheric conditions is discussed. Strange solution of estimated refractive index and size distribution may occurred due to the fact that solution fell into one of local minima in the inversion process for phase function fitting between measured and estimated with assumed refractive index and size distribution. This paper describes atmospheric conditions that may induce such a situation. Namely, it may occur when the atmospheric optical depth is too thin and or Junge parameter is too small. In such case, refractive index and size distribution estimation accuracy is poor. A relation between refractive index and size distribution estimation accuracy and estimation accuracy of the Top of the Atmosphere (TOA) radiance (vicarious calibration accuracy) is also clarified in particular for ASTER/VNIR vicarious calibration. It is found that 10% of the refractive index and size distribution estimation error causes approximately 1.3% of TOA radiance estimation error.**

Keywords—Vicarious calibration; Top of Atmosphere Radiance, At sensor Radiance; refractive index; size distribution; Junge parameter; optical depth

I. INTRODUCTION

Visible and Near Infrared mounted on earth observation satellites and the short-wavelength infrared radiation thermometer, Alternative calibration using measurement data on the ground and onboard calibration by the calibration mounting system is performed. For example, Marine Observation Satellite-1 [1], Landsat-7 Enhanced Thematic Mapper Plus [2], SeaWiFS [3], High Resolution Visible: HRV/SPOT-1 and 2 [4], Hyperion [5], POLDER [6], etc. by ASTER [7]. The calibration results and the like have been reported. Further, report according to reciprocity with a uniform ground surface [8] over a wide area such as desert radiometer each other overlapping of the observation wavelength range have been made [9].

Vicarious calibration can be divided into approaches that are based on the radiance method based on reflectivity. The former to compute the calibration coefficients by the basis of the measurement data of the thickness atmospheric optical instruments from the ground surface reflectance and was placed on the ground, to estimate the atmospheric upper radiance, and compared with satellite radiometer data the contrast, estimates the upper atmospheric radiance also using the vertical measurement data of the thickness atmospheric optical equipped aircraft or the like, the latter is compared with satellite radiometer data. Since the latter requires a lot of costs, there is also a problem of the calibration accuracy of the radiometer mounted on an aircraft, the former is generally used.

Therefore, vicarious calibration is referred to as an alternate calibration simply alternative calibration based on reflectance unless otherwise specified hereinafter. Vicarious calibration method (Bi-Directional Reflectance Distribution Function if it is not the nadir: BRDF [10]) land surface reflectance measurement of optical thickness water vapor that contributes to dissipate in this wavelength range and measurement of aerosol, ozone, dry air "Alternative calibration based on reflectivity" profile calibrated by done, estimates the top of atmosphere radiance by solving the radiative transfer equation based on these satellite visible and near infrared and is compared with the short wavelength infrared radiometer data mostly is. Further, alternative calibration and calibration source which months do not have to consider the influence of the atmosphere is also conducted [11].

Furthermore, same or calibration, etc. through mutual comparison of sensor data of the same kind that are overlapping observation wavelength mounted on the other satellites are also performed [12]. [13], [14]. To conduct the error analysis in the vicarious calibration of visible and near infrared radiometer, Arai et al. made it clear dominant error factors of vicarious calibration accuracy [15]. According to it, error factors most dominant is the ground surface reflectivity, then found to be in the order of aerosol complex refractive index profile deduced from this, the estimation error of the particle size distribution and measurement errors in thickness atmospheric optical are. In addition, Root Sum Square of these factors: It is concluded that vicarious calibration accuracy of the RSS [1] and is about 4%. In addition, the complex refractive index and detailing the effect that estimation accuracy of the particle size distribution on the alternative calibration accuracy. Estimated thickness precision air optical, aerosol complex refractive index, the particle size distribution is dependent on the measurement accuracy sun direct light, rim light, of scattering light, I described in detail the calibration accuracy of the sky radiometer to measure these [16], [17].

Saga University in April 2003, Arai et al. have been doing the observation of aerosol by Sky radiometer. POM-1 sky radiometer you are using is (PREDE Co.) [18]. A device for measuring the scattered light and direct sunlight, to obtain the particle size distribution and the complex refractive index of the aerosol, it is necessary to estimate the scattered light and direct light sky radiometer. It is necessary to solve the inverse problem in this estimation. Is allowed to fit with the aerosol scattering phase function was calculated based on the volume particle size distribution and the complex refractive index observed scattered light is assumed [19], Nakajima propose a method of estimating the volume particle size distribution and the complex refractive index [20]. In addition, Arai we have proposed a method for using the Simulated Annealing: SA as inverse problem solution [21]. Furthermore , improved Langley method as the calibration method of sky radiometer and a method for estimating the top of atmosphere radiance using a method not only downward already proposed, solves the radiative transfer equation by dividing p, the s -polarized light component upward radiance I suggested a corrected and improved Langley method to introduce the concept of late Langley method [22].

Winning, reveal the particle size distribution and the complex refractive index in the case of focusing on the convergence of the particle size distribution and aerosol complex refractive index , which is a problem when the thin optical thickness , particularly fall into local minima , the alternative in this paper I to clarify the effects of calibration accuracy [23]. In addition, the complex refractive index and empirical complex refractive index and (volume particle size distribution) particle size distribution based solar direct, peripheral light, the scattered light measurement and the number of power law distribution, which is calculated from the spectral characteristics of the thick atmosphere optical have performed a comparison of the top of atmosphere radiance when used. The latter requires only instrument small and light whereas the former require heavy instrument relatively large. Therefore, it becomes able to determine the error in case of performing a top of atmosphere radiance estimation by the latter in the test site measurements such as the former is not feasible. In addition, at this time, to clear solar zenith angle of the top of atmosphere radiance, also the observation zenith angle characteristics, I have generalized the discussion.

We introduce a method for estimating the particle size distribution and the complex refractive index in the second chapter, the relationship between the estimation accuracy of the particle size distribution and the complex refractive index and the calibration accuracy of the sky radiometer, particle size distribution and the complex refractive index in the third chapter. I describe the relationship between the vicarious calibration accuracy and the estimation accuracy of the particle size distribution the convergence of the estimation method, the complex refractive index.

II. Method For Estimatingthe Particle Size Distribution and the Complex Refractive Index

I described in this section from the particle size distribution and the complex refractive index of aerosols, the radiative transfer equation [24] to calculate the intensity of the ambient light and direct sun light. Expression of τ_t optical thickness from (1), the optical thickness of the atmosphere can be calculated from the top of atmosphere incident illumination of F_0 and solar observation illumination F of direct sun light.

$$F = F_0 \exp(-m_0\tau_t) \quad (1)$$

where the air mass (θ_0), θ_0 shows the solar zenith angle $m_0 = 1$ / cos. Furthermore, the optical thickness of the atmosphere is represented by the formula (2).

$$\tau_t = \tau_a + \tau_m = \tau_{as} + \tau_{aa} + \tau_{ms} + \tau_{ma} \quad (2)$$

where, τ represents the optical thickness. S index of molecule, the second character scattering, a is the absorption, the entire atmosphere, a is shown a dissipation factor of each aerosol, and m t is the index of the first character. Effects of water molecules and ozone are large optical thickness by molecular absorption.

It is set so as to avoid the intense wavelength of molecular absorption they observed wavelength of the sky radiometer, the observation wavelength of 675nm and 500nm band ozone absorption, 1020nm receive slightly the effect of water molecules absorbed. Next, observation of the solar irradiance scattered light is represented by the formula (3).

$$E(\theta_0, \varphi) \equiv E(\Theta) = F_{m0}\Delta\Omega\,[\omega\tau_t P(\Theta)\, q(\Theta)] \quad (3)$$

where, (the difference between the solar azimuth angle and observation azimuth) relative azimuth, Θ shows a sounding scattering angle with respect to the zenith angle of the sun φ. Relational expression (4) holds between the respective angles.

$$\cos(\Theta) = \cos^2\theta_0 \sin^2\theta_0 \cos\varphi \quad (4)$$

In addition, observation of solar illumination direct light, it is $\Delta\Omega$ $(\tau_{as}\ \tau_{ms}) / \tau_t$ single scattering albedo, P is (Θ) scattering phase function of the atmosphere, F observation solid angle of the sky radiometer, $\omega = q(\Theta)$ I show the contribution of multiple scattering. Then, I think the (Θ) element R to stable independent of the calibration coefficient of the sky radiometer.

[1] RSS = SQRT (dR2 dO2 dA2 dS2 ...),is a value expressed in percentage impact on the top of atmosphere radiance reflectance measurement error, the error measured optical thickness, complex refractive index estimation error of the particle size distribution estimation error dR2, dO2, dA2, dS2 wherein .

R (Θ) = E (Θ) / F_{m0}ΔΩ = ωτ_tP (Θ) q (Θ) ≡ β (Θ) q (Θ) (5)

Divided by the solid angle ΔΩ observation illumination F of direct light, air mass m0, Sky radiometer observations illumination E of solar scattered light (Θ), R represented by the formula (4) (Θ) is or change each it is obtained by suppressing the error with respect to calibration. Therefore, it is a physical quantity which depends on only the state of the atmosphere.

Further, replacing the (Θ), β (Θ) denotes the intensity of single scattering (Θ) = β ωτ_tP. By equation (5), it can be decomposed into the scattering phase function of aerosol scattering P_a (Θ) molecular scattering and P_m (Θ) scattering phase function is P (Θ).

P (Θ) = {$\tau_{ms}P_m$ (Θ) $\tau_{as}P_a$ (Θ)} / (τ_{ms} τ_{as}) (6)

Compared to the observed wavelength λ of the sky radiometer r_m particle size of the molecule is very small (πr_m / λ <0.4). Therefore , the molecular scattering can be represented by Rayleigh scattering , the optical thickness τ_{ms} scattering phase function Pm Rayleigh scattering (Θ), obtained by (8) and (7) , respectively equation .

P_m (Θ) = (3/4) (1/ $\cos^2$ Θ) (7)
τ_{ms} = {0.008569λ-4 (1+ 0.0113λ-2 0.00013λ-4)} (p/p_0) (T_0 / T) (8)

Ground temperature, T, P is the pressure, (288.15K, 1013.25hPa) T0, p0 is a standard temperature, pressure here. The particle size of the aerosol r_a, 0.4 <πr_a the observed wavelength λ of the sky radiometer / λ is in a relationship <3. Therefore, I can be considered by the Mie theory scattering by aerosol.

Aerosol scattering intensity β_a and τ_{as} optical thickness due to Mie scattering (Θ), is determined by (9) each formula.

$$\beta_a(\Theta) = \frac{\lambda^2}{2\pi}\int_{r_{min}}^{r_{max}}[i_1(\Theta,x,\tilde{m}) + i_2(\Theta,x,\tilde{m})]n(r)dr$$
$$\tau_a = \int_{r_{min}}^{r_{max}} \pi r^2 Q_{ext}(x,\tilde{m})n(r)dr \quad (9)$$

where, r the radius of the particle , the maximum radius r_{max} and r_{min} complex refractive index minimum radius and a ~ m, size parameter , n (r) = dN x = (2π / λ) r to (r) / dr is number particle size distribution included in the unit of the air column aerosol particles [1/cm^2/μm], scattering efficiency , which is determined by Mie theory , Q_{ext} (x, ~ m) and i_1 i_2 Me intensity function in (Mie Intensity Function) some . Is used number particle size distribution n and (r) as the particle size distribution of aerosols, using a volume particle size distribution v (r) = dV / d ln r a [cm3/cm2] as a particle size distribution of the aerosol here. There is a relationship of formula (10) (r) n v and (r).

v (r) = (4/3) πr4n (r) (10)

When defined in formula (11) (x, ~ m Θ,) the kernel function and K_{ext} K (x), equation (9) is replaced by equation (12) .

$$K_{ext}(x,\tilde{m}) = \frac{3}{4}\frac{Q_{ext}(x,\tilde{m})}{x},\ K(\Theta,x,\tilde{m}) = \frac{3}{2}\frac{i_1(\Theta,x,\tilde{m}) + i_2(\Theta,x,\tilde{m})}{x^3} \quad (11)$$

$$\beta_a(\Theta) = \frac{2\pi}{\lambda}\int_{r_{min}}^{r_{max}} K(\Theta,x,\tilde{m})v(r)d\ln r$$
$$\tau_a = \frac{2\pi}{\lambda}\int_{r_{min}}^{r_{max}} K_{ext}(x,\tilde{m})v(r)d\ln r \quad (12)$$

In addition, P_a (Θ) = β_a is a (Θ) / $\omega_a\tau_a$, ω_a is the single scattering albedo of the aerosol.

Then, I think the contribution of multiple scattering. Is approximated by the equation (13) observed luminance L of the sun scattered light considering multiple scattering (Θ). Becomes equation (14) can be represented by observing illumination E (Θ) this.

$$L(\Theta) \simeq F_0 m_0 \exp(-m\tau_t)[(\tau_{ms} + \tau_{MS})P_m(\Theta) + \tau_{as}P_a(\Theta) + \tau_A P_m(0°)] \quad (13)$$
$$E(\Theta) \simeq F_0 m_0 \Delta\Omega \exp(-m\tau_t)[(\tau_{ms} + \tau_{MS})P_m(\Theta) + \tau_{as}P_a(\Theta) + \tau_A P_m(0°)] \quad (14)$$

The observation illumination, of light by multiple scattering in the atmosphere is $\tau_{MS}P_m$ (Θ), Rayleigh scattering minutes, further, $\tau_{aS}P_m$ (Θ) is the aerosol scattering minutes $\tau_{mS}P_m$ is (Θ) here. Indicate the observation illumination of light multiple scattering more ground reflected light (0 ˚) $\tau_A P_m$. Therefore,

F_0 m_0 ΔΩ exp (-mτ_t) (τ_{ms} τ_{MS}) P_m (Θ): illumination of the light scattered by molecules:,

F_0 m_0 ΔΩ exp (-mτ_t) τ_{as} P_a (Θ): illumination of the light scattered by aerosol:,

F_0 m_0 ΔΩ exp (-mτ_t) τ_A P_m (0 °): the sum of the illumination of the light scattered in the air further to the ground surface reflection is the observation illumination. In addition, τ_A and τ_{MS} is a component corresponding to the optical thickness of each. In addition, τ_A and τ_{MS} represented by the formula (15), respectively formula empirically [25].

$$\tau_{MS} = 0.02\tau_{SS} + 1.2\tau_{SS}^2\mu_0^{-\frac{1}{4}}$$
$$\tau_A = \frac{A\tau_2}{1 - A\tau_3} \quad (15)$$

where, the optical thickness of the single scattering, μ_0 = cos (θ_0), τ_{SS} = τ_{ms} τ_{sa} the surface albedo , τ_2 = 1.34$\tau_{SS}\mu_0$ [1+ 0.22 (τ_{SS}/μ_0)^2], τ_3 = 0.9τ_{SS} - 0.54τ_{SS}^2 + 0.92τ_{SS}.

When adapting the formula (15) in equation (2), Formula (16) wherein q contribution of multiple scattering (Θ).

q (Θ) ≒ $\tau_{MS}P_m$ (Θ) + $\tau_A P_m$ (0 ˚) (16)

So far, describing the method of calculating R illumination of solar light scattering and direct sun light the F(Θ) particle size distribution of v (r) and the complex refractive index ~ m of aerosol. Then, I calculate the complex refractive index ~ m of aerosol particle size distribution: v (r) R illumination of solar light scattering and direct sun light from F(Θ). For this purpose, it is necessary to solve a non-linear inverse problem. You are using an iterative method based on the equation (17) as the solution of inverse problem in. Skyrad.Pack ver.4.2.

β_a (1) (Θ) = R_{mean} (Θ) β_a (n +1) (Θ) = R_{mean} (Θ) R (n) (Θ) β_a (n) (Θ) (17)

where, the number of iterations superscript of R and β_a is (n), R_{mean} shows the scattered light illumination was observed.

Equation (4), with respect to the scattered light illumination R_{mean} was observed, optimal single scattering illumination β This technique is a method for calculating multiple scattering contribution and q(Θ) and (Θ). Further, to obtain R(n) and (Θ), it is necessary to estimate the complex refractive index ~ m aerosol corresponding to β(n) particle size distribution and v (n) (n) and (r). It is necessary to solve the inverse problem further in order to calculate particle size distribution and v(n) (n) and (r) ~ m. The use of Moore-Penrose generalized inverse matrix in this paper. First, g a matrix consisting of (n-1) (τ_a (0) is the observed value) of τ_a optical thickness of the aerosol scattering illumination β_a aerosol (n) and (Θ), particle size distribution v unknown (I place with the vector v n) of (r). Given g of calculation than a v to contain error ε, g is expressed by equation (18).

$$g = Av + \varepsilon \quad (18)$$

where, A is a linear polynomial matrix for calculating the g from v. At this time, v that minimizes ε can be calculated by the formula (19) using the least-squares type generalized inverse matrix, $(A^TA+ \gamma H)^{-1}A^T$ [26].

$$v= (A^TA+ \gamma H)^{-1}A^Tg \quad (19)$$

where, A^T is the transposed matrix of A, γ indicates a smoothing matrix Lagrange multiplier , and H, of course, downward based on Arai · Ryo model in upward radiance calculation, is calculated by dividing p, the s-polarized light component.

It is possible to set the initial particle size distribution v(n) and (r) In this manner, the provision of R(n) and (Θ). In addition, I τ_a(n) and the Aerosol Optical Thickness sought new at this time. By making repeated until convergence (18) in this way, complex (r) and particle size distribution v aerosol corresponding τ_{mean} optical thickness illumination R_{mean} of scattered light was observed, and (Θ) to (λ_k) it is possible to calculate the refractive index ~ m. It is considered to have converged when it meets one of the conditions of the conditional expression (20).

$$\begin{aligned} \varepsilon^{(1)} &< 0.01 \\ |\varepsilon^{(n)} - \varepsilon^{(n-1)}| &< 0.001 \\ n &\geq 5 \end{aligned} \quad (20)$$

The ε (n) RMSE is a Root Mean Square Error, is expressed by equation (21) here.

$$\varepsilon^{(n)} = \sqrt{\frac{1}{2J}\sum^{J}\left(\frac{R^{(n)}(\Theta_j)}{R^{mean}(\Theta_j)}\right) - 1)^2 + \frac{1}{2K}\sum^{K}\left(\frac{\tau^{(n)}(\lambda_k)}{\tau^{mean}(\lambda_k)}\right) - 1)^2} \quad (21)$$

The index of the observation wavelength, J is the number of observation wavelength total number of scattering angle, K-index of the scattering angle, k is the j here. Further, when the cutlet ε (n)> 0.5, the complex refractive index and ends the estimation of the particle size distribution is determined β(n) not to converge (Θ) with n ≥ 2. Therefore, I will not converge optical thickness becomes very thin. Furthermore, as described below, do not guarantee a global optimum, it is falling into local minima may in this iterative method. That is, since less originally the difference between the estimated scattering phase function measurement and scattering phase function estimation error increases and is considered the solution has converged in the state they do not a best fit when the optical thickness is thin .

III. Experiments

A. *Relationship complex refractive index and the calibration factor, and the particle size distribution*

Direct sun light, rim light and I is shown in Figure 1.

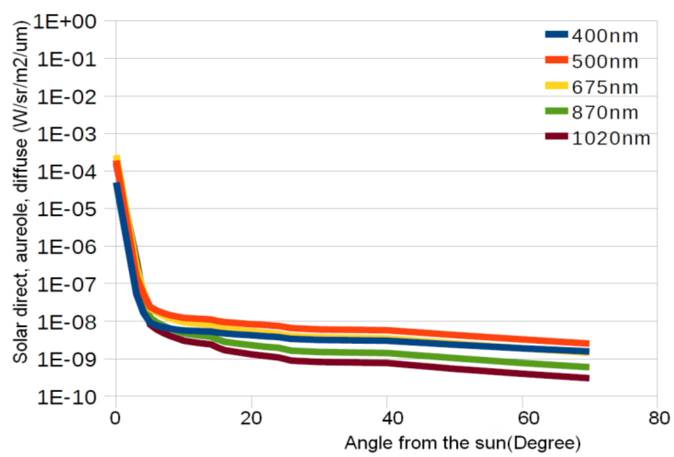

Fig. 1. Example of solar direct, aureole, diffuse irradiance measured on the ground (Angle from the sun =0 means direct solar light, 5 to 20 degree of range of angle from the sun means aureole and the other angle means diffuse light)

An example of the scattered light was calibrated by using the data of sky radiometer that is observed by Saga University. Arai · Ryo model [27] correction improved Langley method based on algorithm was used for calibration. The calibration coefficient of daily observation, error observation error of sky radiometer and the estimation error of the atmospheric conditions, by regression error of the Langley plot at the time included. Therefore, it is necessary to think statistically calibrate the radiometer sky. Figure 2 shows the change in the calibration factor of the sky radiometer. I seen twice is a large change in the calibration factor for each wavelength. 1 time is June 2004; the second time is July 2008. Is referred to as the " third term " changes since " two stage " , the second time period between the second " stage 1 " , and the first time the first time earlier in this paper. July 2008 a second time (period 2 → 3 phase) is the time you have made the (test) maintenance of sky radiometer, the calibration factor is increased compared with that before.

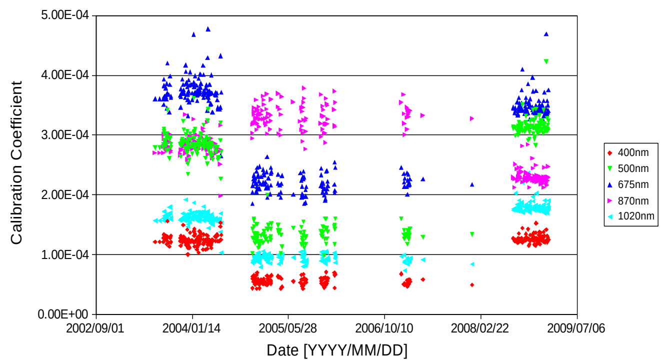

Fig. 2. Trend of calibration coefficient of the skyradiometer of POM-01 manufactured by Prede Co. Ltd. equipped at Saga University

Verify Error Analysis by the variation of the estimation result when an error is included in the calibration factor. The estimated particle size distribution and aerosol complex refractive index using the observation data, October 15, 2008. Using the average value of the three phase, it calibration factor was estimated in addition to deliberately error to 10% -10 %.

First, recalculate the optical thickness by filling in the radiative transfer equation the volume particle size distribution and the complex refractive index was estimated using a sky radiometer data and the optical thickness was observed by sky radiometer. I was comparing the optical thickness that was observed this optical thickness was recalculated. At this time, if you are able to correctly estimate the particle size distribution and the complex refractive index, optical thickness that was observed with the optical thickness that is recalculated are equal. Therefore, it was thought that if the trust radiative transfer equation[2] [29], the estimation accuracy of the particle size distribution and the complex refractive index could be evaluated.

Figure 3 shows the results. Aerosol complex refractive index and solved the inverse problem so as to fit the observed values scattered light intensity and the optical thickness when estimating the particle size distribution , the optical thickness 's can fit more Figure 3 is, I can be seen that the error is only a few % range about ±. Specifically, other ranges can be seen that the solution of the inverse problem cannot be obtained satisfactorily. The reason for this is because the conflict began to arise in the relationship of the scattered light intensity and optical thickness from that error of the calibration factor is large.

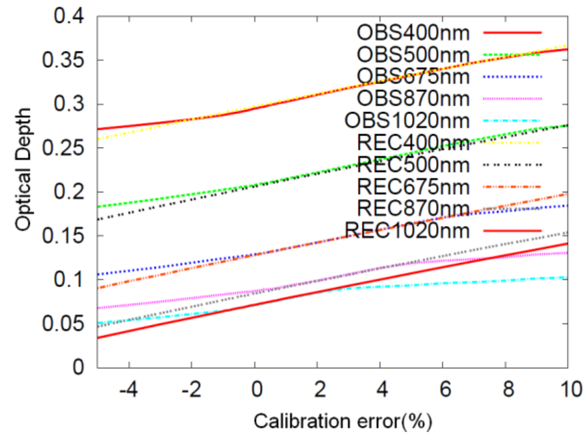

Fig. 3. Measured and re-estimated optical depth as a function of calibration error of the skyradiometer used of which the measurements is conducted at Saga University on October 15 2008.

Here, since the particle size distribution in terms of the number (number distribution) can be approximated by a power distribution is called the number of power distribution. This paper was assumed (Truncated Power Law) censoring power law distribution based on the Junge parameters shown in the following as (r) number of power law distribution n.

$$n(r) = C10^{\nu+1} \qquad (r \le 0.1\mu m) \qquad (22)$$

$$n(r) = Cr^{-(\nu+1)} \qquad (r > 0.1\mu m) \qquad (23)$$

where, r indicates the diameter. The upper limit of r depends on the above equation. I expressed by the aerosol concentration coefficient C and Junge parameter ν is censoring power law distribution. C represents the overall height of the piece power distribution precisely. The concentration of aerosol varies with Junge parameter ν even though constant C that does not mean that C represents the concentration itself. However, it is referred to as the C concentration for convenience in this paper. To derive the optical thickness from the complex refractive index and particle size distribution, I calculate the Mie theory. I was used mie2new.f is attached software of MODTRAN is Mie theory calculations.

As shown in (experimental data in Saga University on October 15, 2008) Figure 4, in general, bimodal characteristic is a (bimodal) but volume particle size distribution is uni-modal characteristics by the number power law distribution to be represented by the Junge parameter is a (uni-modal). Further, because of the use of a Junge parameter indexed to the best approximation coefficients are not suitable only average and particle size distribution of reality. Therefore, the volume particle size distribution by the log-normal distribution expression is appropriate if you are a strict discussion. However, Junge parameter is characterized by to be approximated from (can be obtained from the spectral characteristics of the optical thickness of the atmosphere) angstroms exponential mathematical is easy to handle a single

[2] As can be seen from reference [29] of Lenoble, according to the mutual comparison of the top of atmosphere radiance calculated by the radiative transfer equation previously proposed most of the ground surface conditions and the same atmosphere, those differences are 1% to be less than is known.

parameter. As will be described later, the difference of the estimated top of atmosphere radiance assuming the number of power distribution single parameter by (Junge parameter) and assuming a volume particle size distribution by a lognormal expression 1 in typical atmospheric conditions, it is about 2%. Therefore, it is necessary to allow the error when employing the number of power distribution. In other words, if it is brought into the crowded test site instruments large and heavy, such as Sky radiometer is difficult there are many alternative calibration, there is no choice but to allow the error of 1,2%.

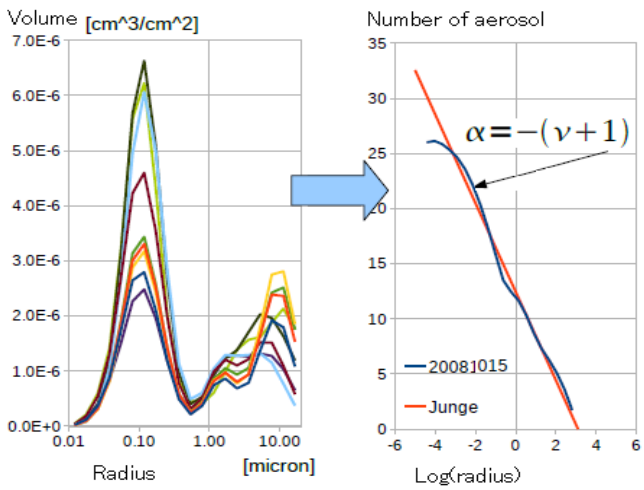

(a) Volume spectrum, Size distribution (b) Number of aerosol particle distribution (vdenotes Junge parameter)

Fig. 4. An example of relation between volume spectra and Junge distribution that are observed at Saga University on October 15 2008.

Complex refractive index that is estimated based on the sky radiometer data acquired in Saga on October 15, 2008 and is shown in Figure 5 the variation of Junge parameter. Complex refractive index real part is found to be nearly invariant to changes in the calibration factor. In addition, Junge parameter is also increased calibration coefficient becomes larger. In addition, the complex refractive index imaginary part has significant change with respect to changes in the calibration factor; the imaginary part is smaller remarkably calibration factor becomes larger. Complex refractive index imaginary part become smaller calibration factor becomes larger, it is because the optical thickness of the atmosphere becomes thick calibration factor is increased; the absorption of the aerosol would have been estimated large.

From the above, errors of 2-3% is included in the calibration factor, I found that the estimated value of the complex refractive index imaginary part is affected most greatly. In addition, I found that Junge parameter varies about 3%, the complex refractive index real part hardly changes. This, I am suggesting from the fact that the error of the calibration factor is increased, the optical thickness estimated the optical thickness that was observed cannot be fit.

Complex refractive index and using the mean of the estimates of 12:00 to 11:00 when evaluating estimation accuracy of the particle size distribution. This time zone is the time zone is the shortest air mass; it is also a time zone Terra satellite passes over the saga further. The observed number of days estimated successful in the time range of 12:00 to 11:00, Phase 1 period 95 days, Phase 2 139 days, Phase 3 period is 68 days.

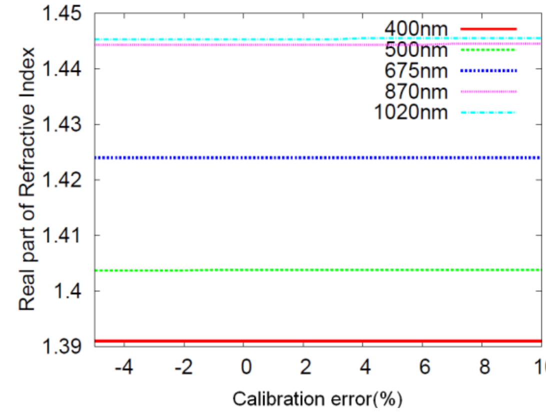

(a) Real part of refractive index

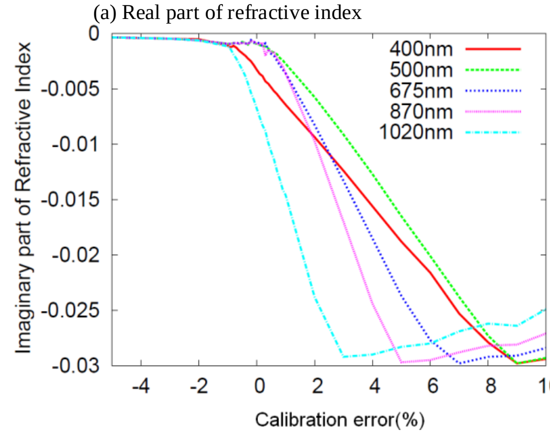

(b) Imaginary part of refractive index

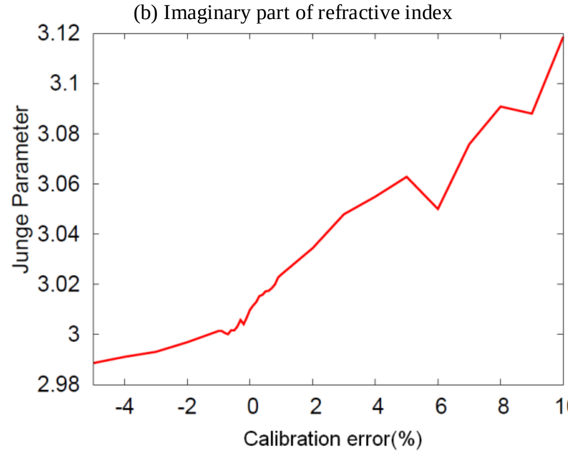

(c) Junge parameter

Fig. 5. Relations between calibration error and refractive index and Junge parameter measured at Saga University on October 15 2008.

Physical amount estimated is three volume particle size distribution of the total aerosol in the air columns complex refractive index real part of the aerosol, the complex refractive index imaginary part, of the unit area [cm^3/cm^2]. I is shown in Figure 6 (a) an estimate of the Junge parameter and asymmetry parameters complex refractive index real part, imaginary part, the phase function. Complex refractive index that was estimated, based on the particle size distribution, to obtain the phase function using (mie2new.f) Mie scattering code that is provided software MODTRAN, was determined Junge parameters and asymmetry parameter. In the figure, upper complex refractive index real part, middle asymmetry parameter, diamond symbol is shown (negation, x100) the complex refractive index imaginary part data of cold color and Junge parameter. In order to investigate the trends in the estimates for calibration factors will be considered as limited to only the data that satisfies the following conditions.

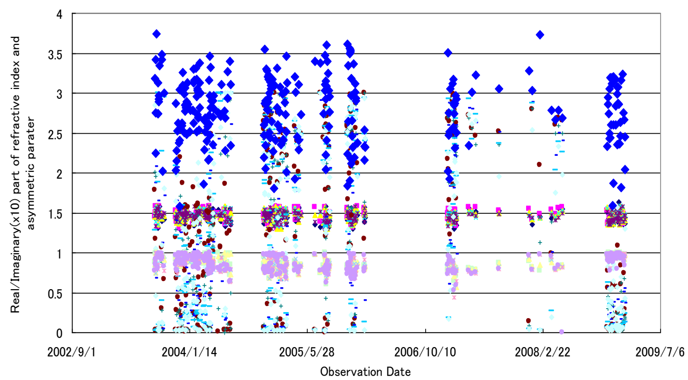

(a) Trends of the estimated real part (around 1.5) and minus imaginary part x 100 (ranges from 0 to 3) of refractive index as well as asymmetric parameter (around 1) together with Junge parameter (◆) (271 of data in total are plotted).

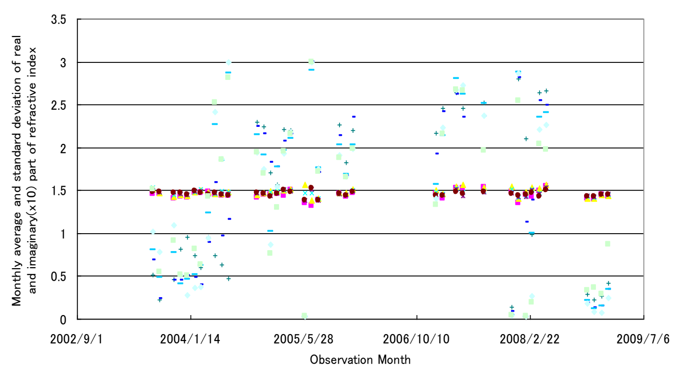

(b) Monthly average of real and minus imaginary (x 100) part of refractive index

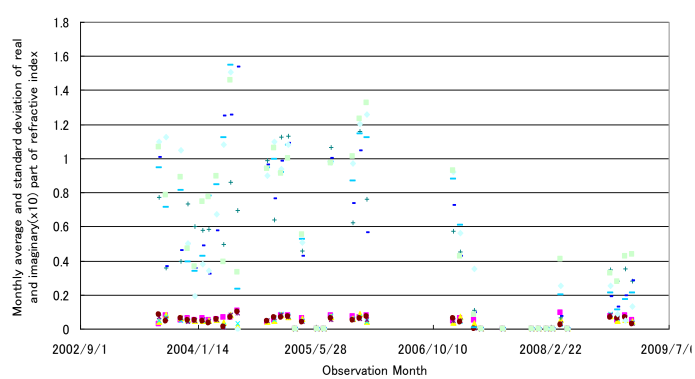

(c) Monthly standard deviation of real and minus imaginary (x 100) part of refractive index.

Fig. 6. Trends of the estimated refractive index and asymmetric parameter with measured skyradiometer data at Saga University during August 2003 and February 2009 (The number of samples a month ranges from 0 to 20). (Warm colored dots show standard deviation of real part (around 0.08) while cold colored dots show imaginary part of refractive index).

Conditions: Sunny, from 11:00 12:00 (average), 1 or less cloud cover 9:00, visibility 10km, Dongfeng[3]

Weather conditions of these were with reference to the observations by the Japan Meteorological Agency. For the day of fine weather there is no effect of clouds on the observation of the sky radiometer, (the same applies to cloud cover) that can be expected estimate of aerosol stable. It is a period of time where you can expect the estimated stable since the time zone is the shortest air mass is 12:00 to 11:00. Visibility indicates the amount of aerosols and air molecules indirectly. Aerosol come is carried on the wind. It is considered to be shown (complex refractive index, Junge parameters) like features aerosol coming carried aboard the easterly, because the same wind, same time zone, aerosol in the same season. Complex refractive index real part of the estimated is shown in Figure 6 (b), in Table 1, and (c) and the standard deviation and the monthly average of the imaginary part. Warm data is complex refractive index real part, cold color data shows the imaginary part in the figure. Complex refractive index imaginary part also shows seasonal variation with a tendency corresponding to the calibration accuracy. I also showed confidence intervals at 95% confidence level as a result of the t-test of the average value of the complex refractive index estimated in Table 1.

TABLE I. MONTHLY AVERAGE, STANDARD DEVIATION AND CONFIDENCE INTERVAL AT 95% OF CONFIDENCE LEVEL OF ESTIMATED REAL AND IMAGINARY PART OF REFRACTIVE INDEX WITH MEASURED SKYRADIOMETER DATA DURING AUGUST 2003 AND FEBRUARY 2009.

Real part	400nm	500nm	675nm	870nm	1020nm
Average	1.4458	1.4806	1.4737	1.4663	1.4579
Standard Deviation	0.04919	0.04814	0.03018	0.03131	0.02748
Confidence Interval@95%	0.0003557	0.0003482	0.0002183	0.0002264	0.0001988
Imaginary part	400nm	500nm	675nm	870nm	1020nm
Average	-0.01453	-0.01417	-0.01442	-0.01392	-0.01411
Standard Deviation	0.09518	0.09337	0.09579	0.09799	0.08828
Confidence Interval@95%	0.0006884	0.0006753	0.0006928	0.0007087	0.0006385

Confidence interval as compared to the average, two orders of magnitude smaller is also the wavelength difference between the estimation of the complex refractive index of the measurement day different is significant with 5 % level. Therefore, it is considered that the complex refractive index of the measurement date was selected as described above, and is similar to the nature of the aerosol parameters, etc. Junge. Further, the average trend of the complex refractive index imaginary part of Figure 6 (b) is the complex refractive index and the imaginary (calibration coefficients tendency similar trend calibration factor Sky radiometer in Figure 2 As is clear from this table there is shown portion is high in the first phase, and low in the second phase, and a) shows high values in the third phase, estimation of the complex index of refraction can be seen that it has much to do with the calibration factor. That is, as described above, I assumed that fall into a local solution

[3] http://www.jma.go.jp/jma/index.html

in iterative methods for calibration accuracy is insufficient; the estimation accuracy of the complex refractive index imaginary part is reduced.

B. The effect on the top of atmosphere radiance

I examined the change in the top of atmosphere radiance to changes in particle size distribution and the complex refractive index of the aerosol. Vicarious calibration target is ASTER / VNIR of Terra satellite. Pick up the field campaign was carried U.S.A. in Nevada Railroad Valley Playa on September 21, 2008 and July 30, 2006 as an example, the complex refractive index and the effect of particle size distribution shows an effect on the top of atmosphere radiance. The test site, Railroad Valley Playa, there is a permanent direct sun light, rim light and the equipment to measure the scattered light as well as the sky radiometer Aureolemeter as part of AERONET [28]. Figure 7, 8 shows the particle size distribution and the complex refractive index estimated from the sky radiometer data and optical thickness, respectively.

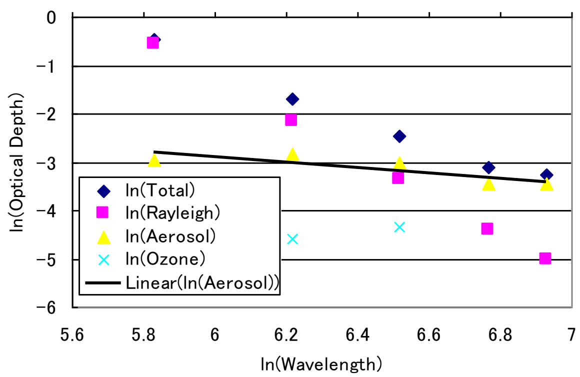

(a) Angstrome exponent and optical depth (21 September 2008)

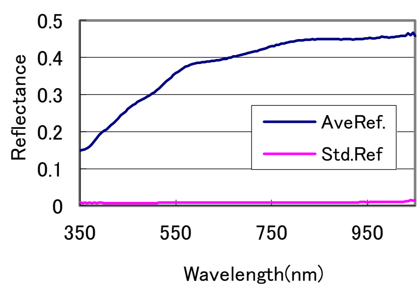

(b)Average and standard deviation of surface reflectance (21 September 2008)

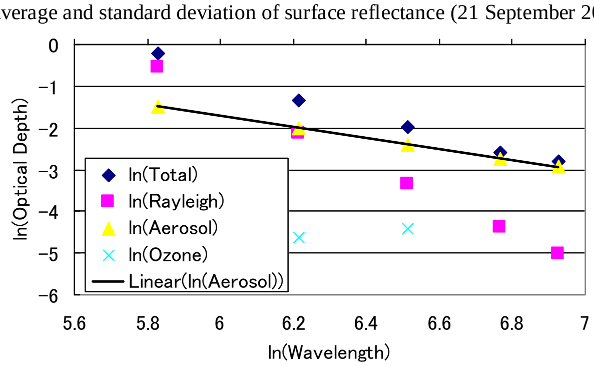

(c) Angstrom exponent and optical depth (30 July 2006)

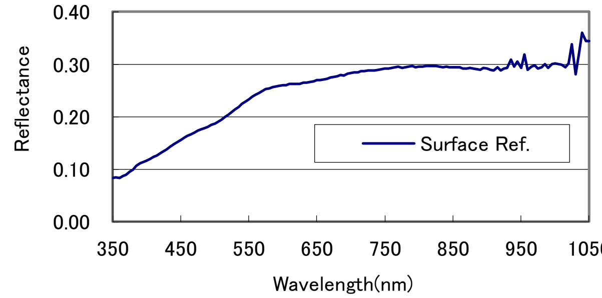

(d)Averaged surface reflectance (30 July 2006)

Fig. 7. Measured optical depth (as well as Angstrom exponent) at Railroad valley playa on (a) 21 September 2008 and at Railroad valley playa on (b) 30 July 2006 (ln(wavelength) of 5.8, 6.2, 6.5, 6.75 and 6.87 is corresponding to the wavelength of 340,500,675,870 and 1020nm, respectively).

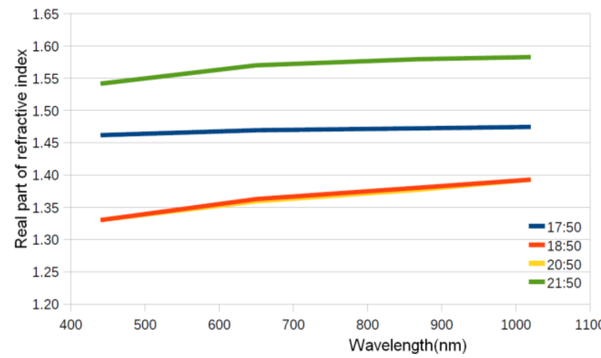

(a) Real part of refractive index (30 July 2006)

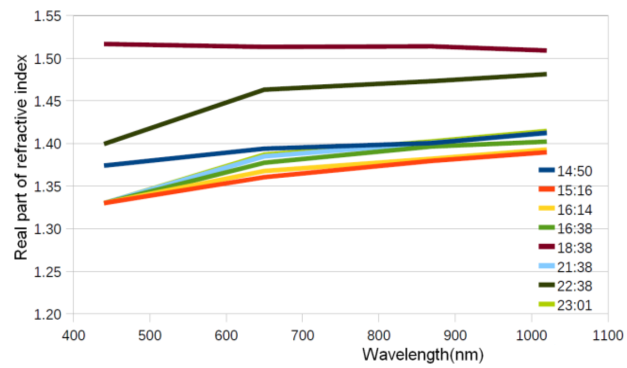

(b) Real part of refractive index (21 September 2008)

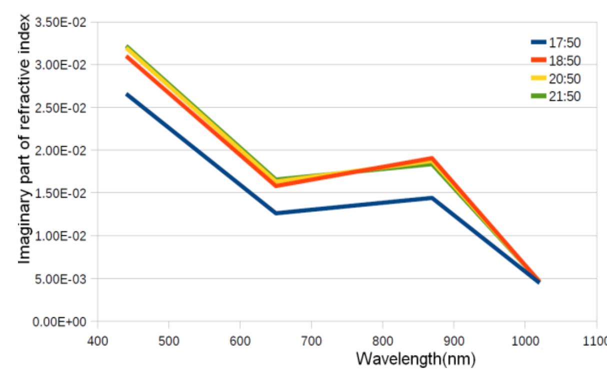

(c) Imaginary part of refractive index (30 July 2006)

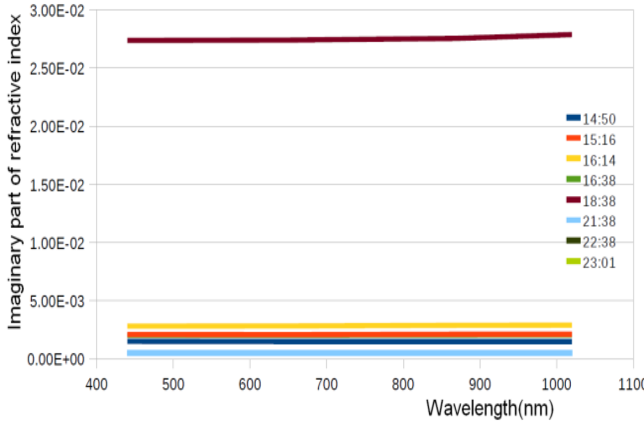

(d) Imaginary part of refractive index (21 September 2008)

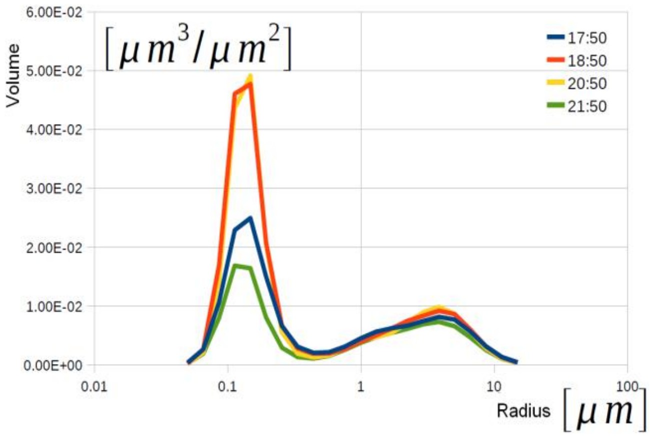

(e) Size distribution (Junge parameter=3.108, 30 July 2006)

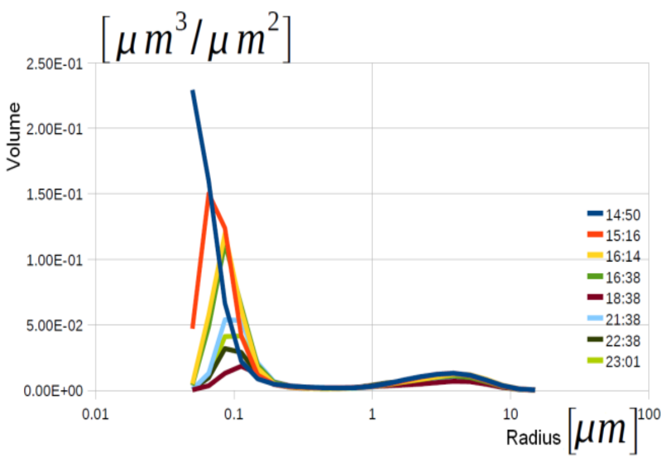

(f) Size distribution (Junge parameter=1.287, 21 September 2008)

Fig. 8. Estimated refractive index and size distribution with the measured skyradiometer data provided by Dr.K.Thome of NASA/ GSFC calculated based on the modified skyrad.pack ver.4.2.

Junge parameters calculated from Angstrom exponent of 2008 and 2006 are 3.108 and 1.287; the estimated complex refractive index was 1.51-i0.028 and 1.35-i0.025. I show the estimation error of the thick atmosphere and optical scattering solar illumination (21) expressions that make up the complex refractive index real part and the imaginary part in Figure 9.

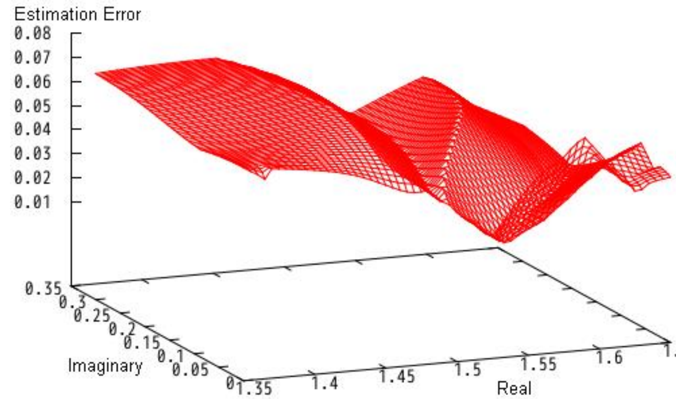

Fig. 9. An example of global minimum and local minima in estimation of refractive index which minimizes estimation errors of solar diffuse irradiance and atmospheric optical depth

There is a global optimal solution in the space of the solution , but the solution converges in local solution has a local solution of many other , and to satisfy the convergence condition (20) in the local solution, global you want to get truly optimal solution, that is, I would be complex refractive index is not found .

The optical thickness of the entire atmosphere in 500nm of 2008 and 2006 are 0.186 and 0.261. Complex refractive index of 2008 and 2006 is almost the same, but the 2006 has a small parameter Junge, who in 2008 is thin optical thickness. We also measured by (20m intervals 60m x 60m) ground surface of the test site is a Playa covered by a substantially uniform silica-based clay for several 10 km square or more, it was estimated ground reflectivity average . Using the EKO Instruments Co. MS720, measures the ground surface reflectance at 1nm wavelength interval based on standard diffusion plate spectralon of LabSphere manufactured by (certified), and carried out the convolution integral of the spectral sensitivity characteristics of ASTER / VNIR I have to calculate the reflectance of each band of VNIR Te. These reflectance and solar zenith angle (18:32:05 UTM respectively, 18:33:34 UTM) in the satellite pass time of observation date, the sun azimuth angle, observation zenith angle, ground surface pressure (hPa), total ozone (DN), I is shown in Table 2 (cm) the total amount of water vapor. Moreover, the volume particle size distribution that ground surface reflectance was measured, was determined from the sky radiometer data, the top of atmosphere radiance Last calculated from ASTER / VNIR data, to obtain the phase function with a complex refractive index, MODTRAN multiple scattering is calculated by, further, the top of atmosphere radiance Lave obtained by considering these computed by MODTRAN absorption total ozone by steam total, the number of data of the thickness atmospheric optical only complex refractive index and particle size distribution volume particle size distribution was estimated from Aureolemeter data and L_{jung} to obtain the coefficients of the power distribution , was modified to use a complex refractive index empirical and compared with L_{aero} using a complex refractive index. I show the comparison results in Table 3. (7) , the band according to its deviation a biased manner have been identified between the calibration factor according to an alternative calibration that is performed here with the calibration factor obtained by using the data of the on-board calibration system ASTER / VNIR is to be 10,5,3 percent in the order 1, 2, 3 [30].

TABLE II. ATMOSPHERIC AND SURFACE CONDITIONS AT THE TEST SITE OF RAILROAD VALLEY PLAYA ON JULY 30 2006 AND SEPTEMBER 21 2008

Observation Date	Solar zenith	Solar azimuth	Atmospheric pressure	Off-Nadir angle	Column ozone	Column water	R_{band1} 560nm	R_{band2} 675nm	R_{band3} 810nm
2006/7/30	25.37	136.1	857	0	248.8	2.52	0.242	0.276	0.297
2008/9/21	40.22	156.3	858	0	232.5	0.82	0.367	0.403	0.446

TABLE III. COMPARISON AMONG ASTER DERIVED TOA RADIANCE (LAST), ESTIMATED TOA RADIANCE WITH THE AVERAGED VOLUME SPECTRA AND REFRACTIVE INDEX (LAVE), ESTIMATED TOA RADIANCE WITH POWER LAW SIZE DISTRIBUTION WITH EMPIRICAL REFRACTIVE INDEX (LJUNG) AND ESTIMATED TOA RADIANCE WITH AERONET DATA (LAERO)

Observation Date	ASTER / VNIR	Last	Ljung	%diff. Ljung	Lave	%diff. Lave	Laero	%diff. Laero
July 30 2006	Band1	137.74	122.40	12.529	124.50	10.631	122.76	12.197
	Band2	116.07	113.89	1.912	115.39	0.592	114.64	1.245
	Band3	89.43	83.48	7.130	82.79	8.026	83.89	6.602
September 21 2008	Band1	168.96	153.66	9.958	153.00	10.431	154.26	9.526
	Band2	140.63	141.85	-0.860	140.98	-0.251	142.54	-1.344
	Band3	105.65	109.60	-3.601	107.30	-1.540	110.04	-3.991

Deviation of the July 30, 2006 L_{aero} and L_{ave} and L_{ast} of Table 3 is almost the same, there is a gap of around 5% deviation of September 21, 2008. In addition, I have shown that people of L_{ave} deviation and L_{ast} to close (7) to (18) between the bias of the alternative calibration factor with the on-board calibration factor over 10 years than the deviation from the $L_{ae\ o\ r}$

Asked the complex refractive index and volume particle size distribution (sun direct light, rim light, scattered light) from the sky radiometer data of September 21, 2008, (xxxVolume, xxx represents the wavelength nm here) top of atmosphere radiance estimated. Determined Junge parameters of the number power distribution from the spectral characteristics of the thick atmosphere optically. As a result, the atmosphere (xxxPlMea) when using a complex refractive index calculated on the (xxxPlEnp) when using the experience in the complex refractive index.

I compared to the top radiance. That is, a comparison for evaluating the error when estimating the upper atmospheric radiance using Junge parameters obtained relatively easily. At this time, the solar zenith angle and was assessed as a function of the observation zenith angle other times, as can also be applied to other sensors of this evaluation result. As shown in Figure 10, (0 degrees observation zenith angle), the difference of the top of atmosphere radiance and (1.44-i0.005 experience value) number of power distribution and volume particle size distribution of 0.1 if the nadir results. I found that also 2.3W/m^2/sr, from, the difference number of the power law distribution (measured value 1.51-i0.028) is 1.3W/m^2/sr from 0.8.

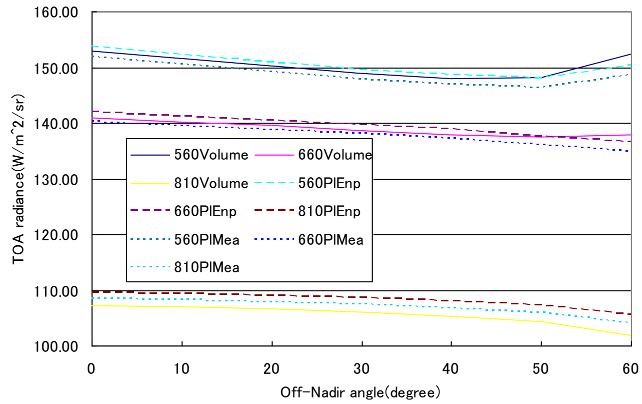

(a) Observation zenith angle dependency

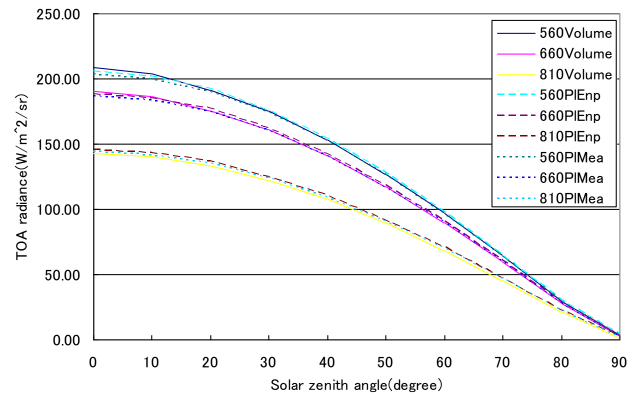

(b) Solar zenith angle dependency

Fig. 10. Difference of estimated top of the atmosphere radiance with volume spectra of size distribution and power law distributions and their off-nadir angle dependency as well as solar zenith angle dependency for the field campaign at Railroad Valley playa on September 21 2008. Where xxxVolume denotes TOA radiance calculated with volume spectra and measured refractive index at xxx(nm) of wavelength while xxxPlEnp denotes that with power law of size distribution with the empirical refractive index(1.44-i0.005) and xxxPlMea denotes that with power law size distribution with the measured refractive index(1.51-i0.028).

In addition, I found that this difference is larger observation zenith angle increases. Think anyone who wants to estimate solar direct light, rim light, by scattering light measurement value the complex refractive index and volume particle size distribution is the best to the top of atmosphere radiance estimated that these measurements are not possible, atmospheric optical it was found that the difference is 1,2 % to estimate the parameters of the number of power distribution only from the measurement data of the thickness, even if the estimated top of atmosphere radiance using a complex refractive index empirical. It was also found that if it is possible to measure the complex refractive index difference between the two is less than 1%. Therefore, estimation of the complex index of refraction in the case of using the Junge parameter is important, but the method for measuring the polarization component of the atmospheric scattering light using a portable handy polarized radiometer small and lightweight even for this is also proposed by the authors 30 you have). At this time, I is shown in Figure 11 the difference in phase function.

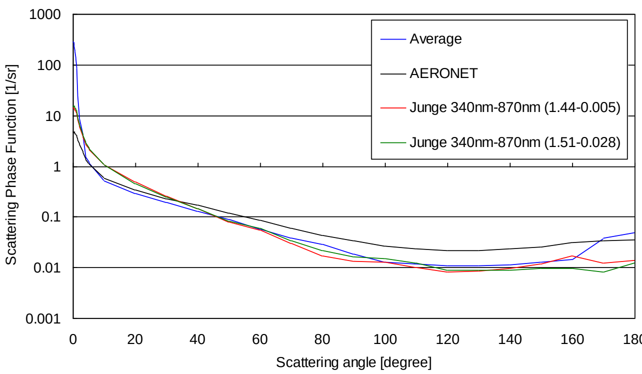

Fig. 11. Difference of phase function at 675nm with volume spectra and power law based size distributions for the field campaign at Railroad Valley playa on September 21 2008. Average denotes the phase function with volume spectra derived from skyradiometer data while AERONET denotes that with size distribution derived from AERONET data. "Junge" denotes phase function with Junge parameters derived from optical depth at 340nm and 870nm and with 1.44-0.005i of empirical refractive index as well as with measured index of 1.51-0.028i.

Symbol Average in the figure is a phase function that was calculated using the complex refractive index and the volume particle size distribution was determined using a sky radiometer data, AERONET is a volume particle size distribution and the complex refractive index obtained from the AERONET data is a phase function determined by mie2new.f earlier using. Is a phase function that determines the Junge [29] Junge parameters from aerosol optical thickness of 870 nm and 340 nm, was determined using the empirical values and measured values of the complex refractive index thereto. I found that towards the phase function of Junge is larger than the forward scattering AERONET, also, represents the backscattering is small, and the difference between the experiences with the actual value of the complex index of refraction is insignificant. Therefore, the person in the case of Junge, the greater the top of atmosphere radiance than AERONET. However, the difference between the top of atmosphere radiance is about 3%, as described below.

Complex refractive index respectively and Figure 12, 13 shows the variation of the top of atmosphere radiance to changes in particle size distribution. Was calculated assuming the observed brightness of ASTER is the top of atmosphere radiance. I can be seen from these, the top of atmosphere brightness is less complex refractive index imaginary part is increased; the top of atmosphere brightness also increases Junge parameter increases. However, the tendency is small, it is 153 ± 2 [W/m^2/sr/μm] the real part of the complex refractive index can be made to change 1.5 ± 0.15, i.e., an error of 10% even occurred I see that. In addition, the imaginary part is a 153 ± 0.5 [W/m^2/sr/μm] also be 0.015 ± 0.0015 change, further, in the case of the Junge parameter is varied and 3 ± 0.3 153 ± 2 [W/m^2/sr / was found to vary with μm]. That is, it is understood that it is not only an error of 1.31% to the top of atmosphere radiance also expects 10% ± the estimation error thereof.

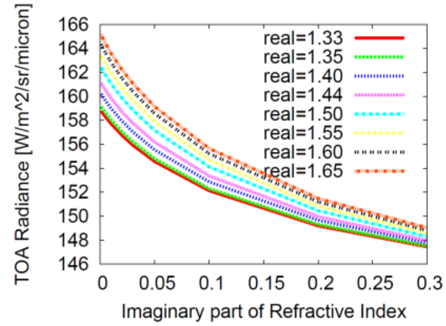

(a) Band 1(560nm)

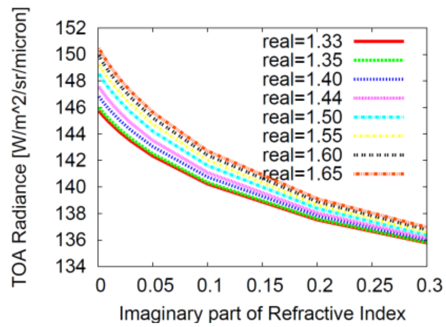

(b) Band 2(660nm)

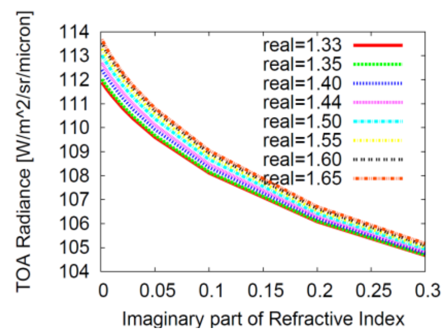

(c) Band 3N (810nm)

Fig. 12. Calculated TOA radiance derived from the field campaign at Railroad valley on September 21 2008 with the parameters of real and imaginary parts of refractive index.

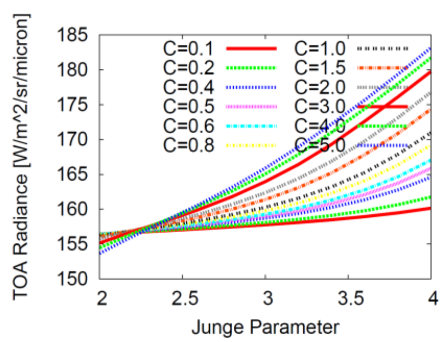

(a) Band 1(560nm)

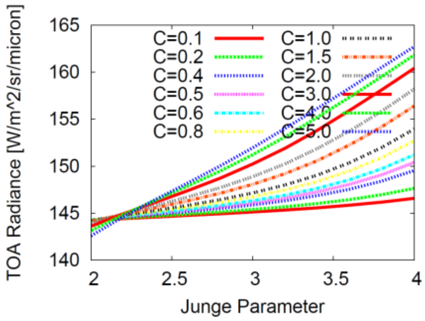

(b) Band 2(660nm)

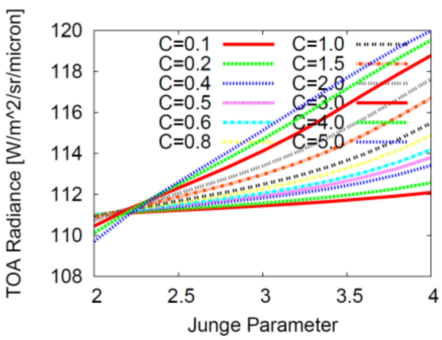

(c) Band 3N (810nm)

Fig. 13. Calculated TOA radiance as a function of Junge parameter derived from the field campaign at Railroad valley on September 21 2008 with the parameters of real and imaginary parts of refractive index where $n(r) = C10^{\nu+1}$ ($r \leq 0.1\mu m$) and $n(r) = Cr^{-(\nu+1)}$ ($r > 0.1\mu m$).

IV. CONCLUSION

Complex refractive index empirical and complex index of refraction and (volume particle size distribution) particle size distribution based solar direct, peripheral light, the scattered light measurement and I used the number power law distribution, which is calculated from the spectral characteristics of the thick atmosphere optical result of comparing the top of atmosphere radiance case, it was found to be 1,2 %. Therefore, tolerances that must be assumed in the alternative calibration bringing the test site instruments heavy relatively large as Aureolemeter and sky radiometer is difficult revealed.

Further, the estimated scattering phase function complex refractive index to aerosol complex refractive index in the case Junge parameter, or if the thickness atmosphere optically thin small and errors of particle size distribution estimation has assumed measured scattering phase function and using a particle size distribution it was found that due to the convergence of iterative solution when to fit with.

Further, we estimate error analysis of the particle size distribution and aerosol complex refractive index , the estimation error of the top of atmosphere radiance, i.e., as in the alternative calibration error is about 1.3% Even 10% even if an error of these I made it clear to. Therefore, if such an alternative calibration test site thin thickness atmospheric optical particularly understood that a (solution does not converge if more) 2,3 % request for calibration accuracy of the sky radiometer .

ACKNOWLEDGMENT

The author would like to thank Dr. Kenta Azuma for his efforts through experiments and simulations.

REFERENCES

[1] Arai K., Preliminary assessment of radiometric accuracy for MOS-1 sensors, International Journal of Remote Sensing, 9, 1, 5-12, 1988.

[2] Barker, JL, SK Dolan, et al., Landsat-7 mission and early results, SPIE, 3870, 299-311, 1999.

[3] Barnes, RA, EEEplee, et al., Changes in the radiometric sensitivity of SeaWiFS determined from lunar and solar based measurements, Applied Optics, 38, 4649-4664, 1999.

[4] Gellman, DI, SF Biggar, et al., Review of SPOT-1 and 2 calibrations at White Sands from launch to the present, Proc. SPIE, Conf.No.1938, 118-125, 1993.

[5] Folkman, MA, S.Sandor, et al., Updated results from performance characterization and calibration of the TRWIS III Hyperspectral Imager, Proc. SPIE, 3118-17, 142, 1997.

[6] Hagolle, O., P.Galoub, et al., Results of POLDER in-flight calibration, IEEE Trans. On Geoscience and Remote Sensing, 37, 1550-1566, 1999.

[7] Thome, K., K. Arai, S. Tsuchida and S. Biggar, Vicarious calibration of ASTER via the reflectance based approach, IEEE transaction of GeoScience and Remote Sensing, 46, 10, 3285-3295, 2008.

[8] Cosnefroy, H., M.Leroy and X.Briottet, Selection and characterization of Saharan and Arabian Desert sites for the calibration of optical satellite sensors, Remote Sensing of Environment, 58, 110-114, 1996.

[9] Arai, K., In-flight test site cross calibration between mission instruments onboard same platform, Advances in Space Research, 19, 9, 1317-1328, 1997.

[10] Nicodemus, FE, "Directional Reflectance and Emissivity of an Opaque Surface", Applied Optic (1965), or FE Nicodemus, JC Richmond, JJ Hsia, IW Ginsber, and T. Limperis, "Geometrical Considerations and Nomenclature for Reflectance, ", NBS Monograph 160, US Dept. of Commerce (1977).

[11] Slater, PN, SFBiggar, RGHolm, RDJackson, Y.Mao, MSMoran, JMPalmer and B.Yuan, Reflectance-and radiance-based methods for the in-flight absolute calibration of multispectral sensors, Remote Sensing of Environment, 22, 11-37, 1987.

[12] Kieffer, HH and RL Wildey, Establishing the moon as a spectral radiance standard, J., Atmosphere and Oceanic Technologies, 13, 360-375, 1996.

[13] Arai, K., Atmospheric Correction and Residual Errors in Vicarious Cross-Calibration of AVNIR and OCTS Both Onboard ADEOS, Advances in Space Research, 25, 5, 1055-1058, 1999.

[14] Liu;. JI, Z. Li, YL Qiao, Y.-J. Liu, and Y.-X. Zhang, A new method for cross-calibration of two satellite sensors, Int J. of Remote Sensing, 25 , 23 5267-5281 , 2004 .

[15] Kohei Arai , error analysis of vicarious calibration of satellite visible and near infrared radiometer based KJThome, reflectance , Japan Photogrammetry Journal , Vol.39, No.2, pp.99-105, (2000) .

[16] Arai, K., Vicarious calibration for solar reflection channels of radiometers onboard satellites with deserted area of data, Advances in Space Research, 39, 1, 13-19, 2006.

[17] Arai, K. and X.Liang, Characterization of aerosols in Saga city areas, Japan withy direct and diffuse solar irradiance and aureole observations, Advances in Space Research, 39, 1, 23-27, 2006.

[18] Kohei Arai , vicarious calibration of ASTER / VNIR based on long-term observations of the optical properties of aerosols in Saga , Journal of the Remote Sensing Society of Japan , 28,3,246 over 255,2008

[19] Kohei Arai , applied linear algebra , modern science , Inc. , 2006

[20] Nakajima, T., M.Tanaka and T. Yamauchi, Retrieval of the optical properties of aerosols from aureole and extinction data, Applied Optics, 22, 19, 2951-2959, 1983.

[21] Kohei Arai , complex refractive index of aerosol using direct sun beams Xing Ming , by simulated annealing , and a peripheral light scattering and simultaneous estimation of particle size distribution , Journal of the Remote Sensing Society of Japan , Vol.23, No.1, pp .11-20,2003 .

[22] Arai K. and X.Liang, Method for the top of the atmosphere radiance estimation taking into account the polarization in down and up welling radiance calculations, Journal of the Japanese Society for Photogrammetry and Remote Sensing, 44, 3, 4 - 12 , 2005 . Sun direct -based

[23] Kohei Arai , Liang Xing Ming , to improve Langley method and improve the calibration accuracy of the ambient light meter , ,47,4,21 - 28 , 2008 Japan Society of Photogrammetry

[24] Teruyuki Nakajima, Glauco Tonna, Ruizhong Rao, Paolo Boi, Yoram Kaufman, and Brent Holben, Use of sky brightness measurements from ground for remote sensing of particulate polydispersions, "Appl. Opt. 35, 2672-2686, 1996.

[25] Box and Deepak, An Approximation to Multiple Scattering in the Earth's Atmosphere: Almucatar Radiance Formulation, Journal of the Atmospheric Sciences, 38, 1037-1048, 1981.

[26] Kohei Arai , self-study remote sensing , Morikita publication , 2004

[27] Kohei Arai , Basic theory of remote sensing , academic book publishing , 2001 .

[28] Aoki, K., T. Takamura, and T. Nakajima, Aerosol optical properties measured by SKYNET skyradiometer validation network. Proc. Of the 2nd EarthCARE Workshop, 133-134, 2005.

[29] Lenoble, J. edt, Radiative transfer in scattering and absorbing atmospheres:. Standard computational procedures, A.Deepak Publishing, 1985.

[30] Kohei Arai, Aerosol refractive index estimation with ground based polarization measurement data, Abstract of the 50th COSPAR (Committee on Space Research / ICSU) Congress, A3.1-0092-08 \, 985, Montreal, Canada, July, 2008

AUTHORS PROFILE

Kohei Arai, He received BS, MS and PhD degrees in 1972, 1974 and 1982, respectively. He was with The Institute for Industrial Science and Technology of the University of Tokyo from April 1974 to December 1978 also was with National Space Development Agency of Japan from January, 1979 to March, 1990. During from 1985 to 1987, he was with Canada Centre for Remote Sensing as a Post Doctoral Fellow of National Science and Engineering Research Council of Canada. He moved to Saga University as a Professor in Department of Information Science on April 1990. He was a councilor for the Aeronautics and Space related to the Technology Committee of the Ministry of Science and Technology during from 1998 to 2000. He was a councilor of Saga University for 2002 and 2003. He also was an executive councilor for the Remote Sensing Society of Japan for 2003 to 2005. He is an Adjunct Professor of University of Arizona, USA since 1998. He also is Vice Chairman of the Commission "A" of ICSU/COSPAR since 2008. He wrote 30 books and published 492 journal papers

Sensitivity Analysis and Error Analysis of Reflectance Based Vicarious Calibration with Estimated Aerosol Refractive Index and Size Distribution Derived from Measured Solar Direct and Diffuse Irradiance as well as Measured Surface Reflectance

Kohei Arai [1]
Graduate School of Science and Engineering
Saga University
Saga City, Japan

***Abstract*—Sensitivity analysis and error of reflectance based vicarious calibration with estimated aerosol refractive index and size distribution derived from measured solar direct and diffuse irradiance as well as measured surface reflectance is conducted for solar reflective channels of mission instruments onboard remote sensing satellites. Through these error analyses, it is found that the most influencing factor is surface reflectance. The most significant 75 to 91% of vicarious calibration coefficients error is due to surface reflectance followed by atmospheric optical depth and Junge parameter. Therefore, we have to care about surface reflectance measuring accuracy followed by atmospheric optical depth (aerosol refractive index, and water vapor and ozone absorption) and Junge parameter (aerosol size distribution). As a conclusion, it is confirmed that surface reflectance is most influencing factor on TOA radiance. When the atmospheric optical depth is small, then Junge parameter is influencing.**

Keywords—Vicarious calibration; Top of Atmosphere Radiance; At sensor Radiance; refractive index; size distribution; Junge parameter; optical depth

I. INTRODUCTION

Vicarious calibration for solar reflective channels of mission instruments onboard remote sensing satellites, visible and Near Infrared radiometers and short-wavelength infrared radiometers is widely ation thermometer, Alternative calibration using measurement data on the ground and onboard calibration by the calibration mounting system is performed. For example, Marine Observation Satellite-1 [1], Landsat-7 Enhanced Thematic Mapper Plus [2], SeaWiFS [3], High Resolution Visible: HRV/SPOT-1 and 2 [4], Hyperion [5], POLDER [6], etc. by ASTER [7]. The calibration results and the like have been reported. Further, report according to reciprocity with a uniform ground surface [8] over a wide area such as desert radiometer each other overlapping of the observation wavelength range have been made [9].

Vicarious calibration can be divided into approaches that are based on the radiance method based on reflectivity. The former to compute the calibration coefficients by the basis of the measurement data of the thickness atmospheric optical instruments from the ground surface reflectance and was placed on the ground, to estimate the atmospheric upper radiance, and compared with satellite radiometer data the contrast, estimates the upper atmospheric radiance also using the vertical measurement data of the thickness atmospheric optical equipped aircraft or the like, the latter is compared with satellite radiometer data. After the latter requires a lot of costs, there is also a problem of the calibration accuracy of the radiometer mounted on an aircraft, the former is generally used.

In order to clarify sensitivities of the parameters which are influencing to vicarious calibration accu5racvy, sensitivity analysis is conducted. It is well reported that the most influencing parameter on vicarious calibration accuracy is surface reflectance. Therefore, an error analysis is conducted for surface reflectance on vicarious calibration accuracy.

The next section describes the method for sensitivity analysis and error analysis together with specific parameters of vicarious calibration in particular for ASTER/VNIR which is onboard on Terra satellite of the first earth observation satellites of EOS project which is lead by NASA. Then the results from sensitivity analysis and error analysis are described followed by conclusion and some discussions.

II. PROPOSED METHOD

A. Reflectance based vicarious calibration method

This section briefly describes the reflectance-based method used in this work and reminds the reader how this method is applied to solar reflection spectral channels of mission instruments onboard remote sensing satellite. Most of calibration teams use the reflectance-based approach, but differences in the specific application of the method exist. The basic philosophy of the reflectance-based approach relies on ground-based, surface reflectance measurements of a selected site. These test sites are described in the following section. The results of the ground-based measurements are input into a radiative transfer code. Inherently, the radiative transfer codes are solar irradiance models that allow for the conversion of relative radiance (can be viewed as reflectance) to absolute radiance. The solar model for the current work is based on the World Radiation Center (WRC) model. This solar model was selected by most of calibration teams. The importance of this is that results can differ significantly based on the solar model that is chosen. Once the at-sensor, hyperspectral, absolute radiances are determined; they are band-averaged across the sensor spectral response to give a predicted, at-sensor, spectral radiance for the specific band of interest. This absolute radiative transfer code output is compared to that from the sensor to derive the calibration or to validate the reported at-sensor radiance.

The target mission instrument for sensitivity analysis and error analysis is ASTER/VNIR which is onboard on Terra satellite. ASTER/VNIR is visible to Near Infrared Radiometer with 15 meter of Instantaneous Field of View: IFOV. Wavelength coverage of each spectral wavelength band is shown in Table 1. Table 2 lists the high and normal gains as well as the band-averaged center wavelength for the VNIR bands of ASTER. Also unit conversion coefficients which allow convert from Digital Number: DN of ASTER/VNIR output to radiance in unit of W/m^2 str μm are listed in Table 3.

TABLE I. WAVELENGTH COVERAGE OF ASTER/VNIR

Spectral Band	Wavelength Coverage
Band1	0.52 ~ 0.60μm
Band2	0.63 ~ 0.69μm
Band3	0.76 ~ 0.86μm

TABLE II. LIST THE HIGH AND NORMAL GAINS AS WELL AS THE BAND-AVERAGED CENTER WAVELENGTH FOR THE VNIR BANDS OF ASTER.

Band No.	Maximum Radiance (W/m^2 str μm)			
	High Gain	Normal Gain	Low Gain 1	Low Gain 2
1	170.8	427	569	N/A
2	179.0	358	477	N/A
3	106.8	218	290	N/A

TABLE III. CALCULATED UNIT CONVERSION COEFFICIENTS: UCC

Band No.	Conversion Coefficients (W/m^2 str μm)			
	High Gain	Normal Gain	Low Gain 1	Low Gain 2
1	0.676	1.688	2.25	N/A
2	0.708	1.415	1.89	N/A
3	0.423	0.862	1.15	N/A

B. *Test sites*

The joint field campaigns for ASTER took place at Ivanpah Playa, California and Railroad Valley Playa in Nevada. These test sites have been described in detail elsewhere and their descriptions are not given here. Both sites are clay-dominated dry lakes and have been used for other sensors after the mid-1990s. The Ivanpah Playa is a hard surface. It is located south of Las Vegas, Nevada on the California-Nevada border. Figure 1(a) shows ASTER/VNIR image of the test site of Ivanpah playa while Figure 1 (b) shows a portion of ASTER/VNIR image of Alkali Lake test site. Also, Figure 1(c) shows ASTER/VNIR image of the Railroad Valley Playa test site.

These test sites are selected due to the fact that these are widely situated and homogeneous and also are situated at relatively high elevation (thin atmosphere). These are accessible comparatively easily.

(a)Inapah playa

(b)Alkali Lake

(c)Railroad Valley Playa

Fig. 1. Test sites for vicarious calibration

C. Method

As described above, the reflectance-based approach relies on measurements of the surface reflectance and atmospheric properties at the time of the sensor overpass. The calibration team determines the reflectance of the test site by transporting a spectral-radiometer across a rectangular test site that is 80 m by 300 m in size with the longer side being perpendicular to the along-track direction of the Terra platform. The primary instrument for the surface-reflectance collection is a commercially-available spectrometer that reports output at 1-nm intervals across the 350-2500 nm spectral range. Reflectance of the site is determined by ratioing the measurements of the site to those of a reference panel for which the bi-directional reflectance factor has been determined in the laboratory.

The second piece of information needed in the reflectance-based method is a characterization of the atmosphere. The solar radiometer is relatively calibrated immediately prior to, during, or after each field campaign via the Langley method and this allows for the determination of spectral atmospheric optical depths. The optical depth results are used as part of an inversion scheme to determine ozone optical depth and an aerosol size distribution. The aerosols are assumed to follow a power law distribution, also referred to as a Junge distribution. Columnar water vapor is derived from the solar extinction data using a modified-Langley approach.

The atmospheric and surface data are used in a radiative transfer code. There are a variety of codes available that all satisfy the requirements of predicting the at-sensor radiance to the required accuracy. The radiative transfer code used is MODTRAN which assumes a plane-parallel, homogeneous atmosphere and divides this atmosphere into layers to account for the vertical distribution of scatterers and weak absorption due to ozone in the visible and near infrared (approximately the 400 to 800 nm spectral range known as the Chappuis absorption band). The Junge parameter described in the previous section that is derived from the solar radiometer measurements is used to compute Mie scattering phase functions used in the code. The surface in this work is assumed to be Lambertian. The near-nadir view for the majority of the ASTER overpasses reduces the uncertainty of this assumption after the dominant direct-reflected solar irradiance is correctly taken into account.

Strong gaseous absorption effects due to water vapor are determined using MODTRAN to compute transmittance for the sun-to-surface-to-satellite path for 1-nm intervals from 350 to 2500 nm. This sun-to-ground-to-sensor transmittance is multiplied by the at-sensor radiance output from the radiative transfer code to correct the radiances for this strong absorption.

Meanwhile, this approach is an approximation that excludes interactions between diffusely-scattered radiances and absorption; it does not cause large uncertainties for application to ASTER because of the small effect of absorption within most of the bands and the typically high surface reflectance of the test sites used in this work.

III. RESULTS FROM SENSITIVITY ANALYSIS AND ERROR ANALYSIS

A. Radiometric Calibration Coefficients: RCCs

Radiometric Calibration Coefficients: RCCs calculated with onboard calibration data and RCCs estimated with vicarious calibration data are plotted in Figure 2 together with difference between onboard and vicarious RCCs (D).

RCC

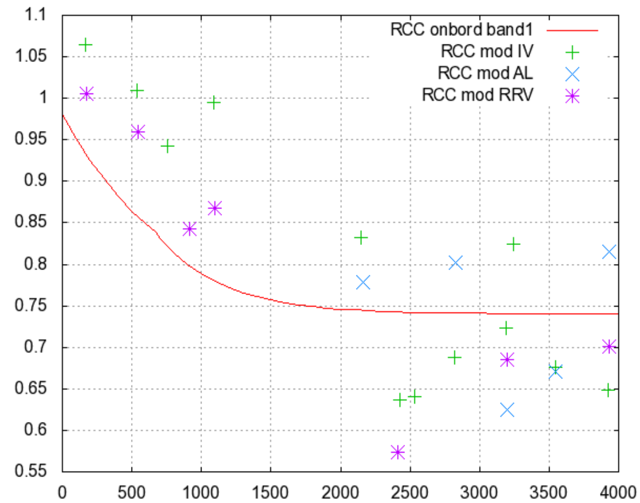

Days after launch
(a)Band 1

RCC

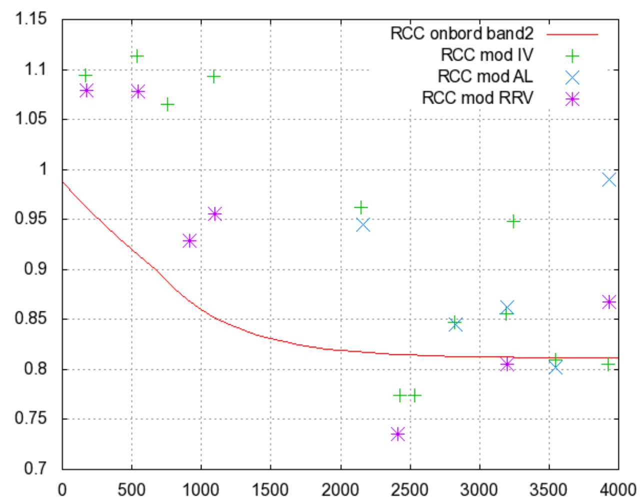

Days after launch
(b)Band 2

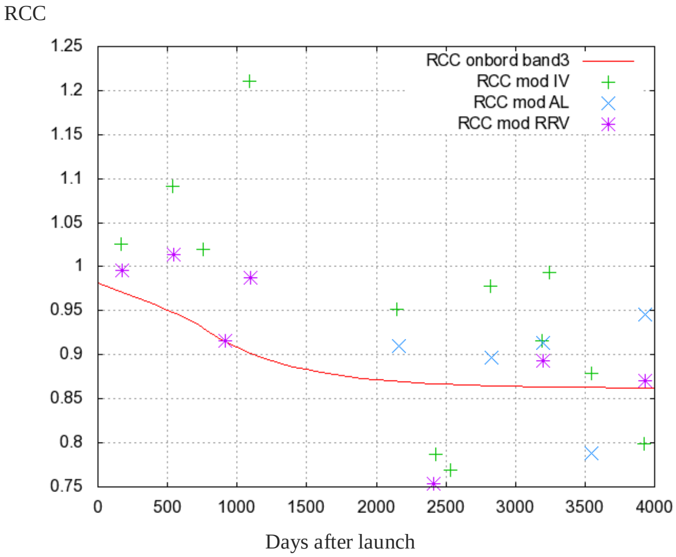

(c)Band 3

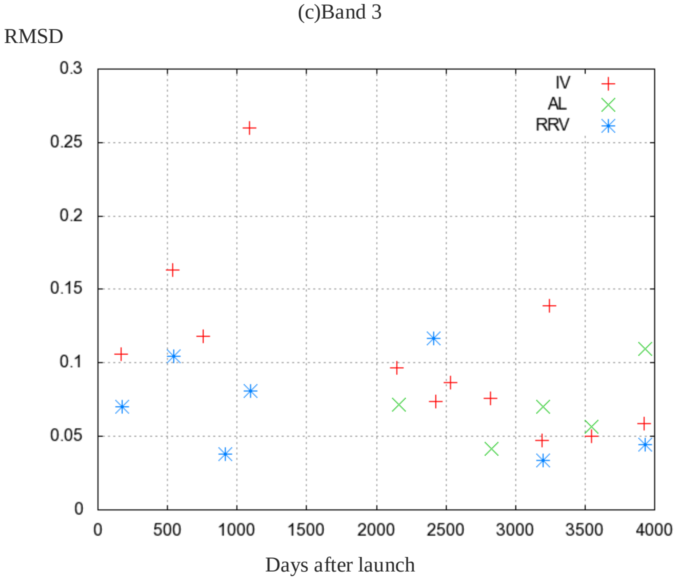

(d)Root Mean Square Difference: RMSD between vicarious and onboard calibration coefficients

Fig. 2. Trends of onboard and vicarious calibration coefficients and the dereference between both

B. Sensitivity Analysis

Vicarious calibration accuracy depends on surface reflectance, atmospheric optical depth measurement, solar direct and diffuse irradiance atmospheric radiative transfer code etc. In order to clarify how sensitive these parameters are, .sensitivity analysis with actual measured data which are acquired at Ivanpah playa in California, U.S.A. on September 14 2008. Major atmospheric parameters, Junge parameter, atmospheric optical depthy at 500 nm are as follows,

Junge parameter: 3.2

Atmospheric optical depth: 0.23

Top of the Atmosphere: TOA radiance (At Sensor Radiance) is calculated with the variables of surface reflectance, Atmospheric optical depth and Junge parameters. Figure 3 (a) shows the calculated TOA radiance with constant optical depth and the variables of surface reflectance and Junge parameters ranges from -50 to +50 % for Band 1 while that for Band 2 is shown in Figure 3 (b).

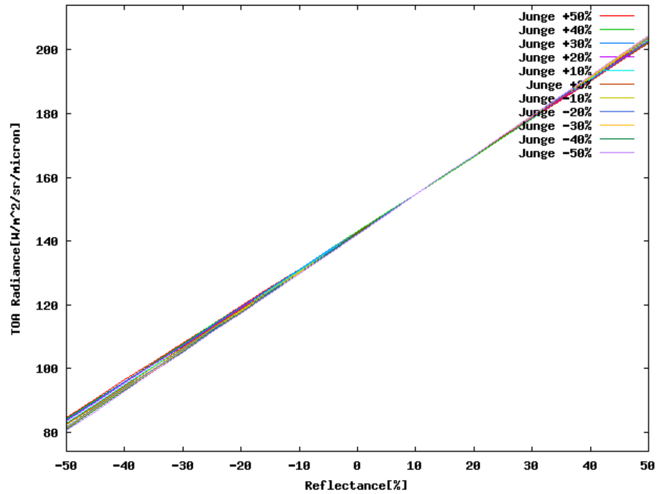

(a)Band 1

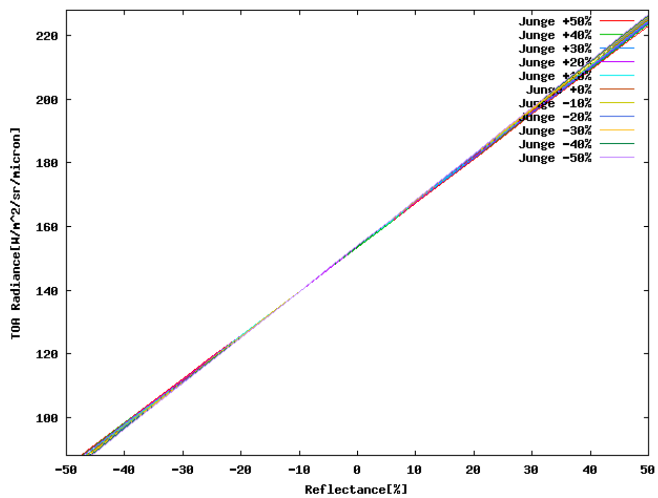

(b) Band 2

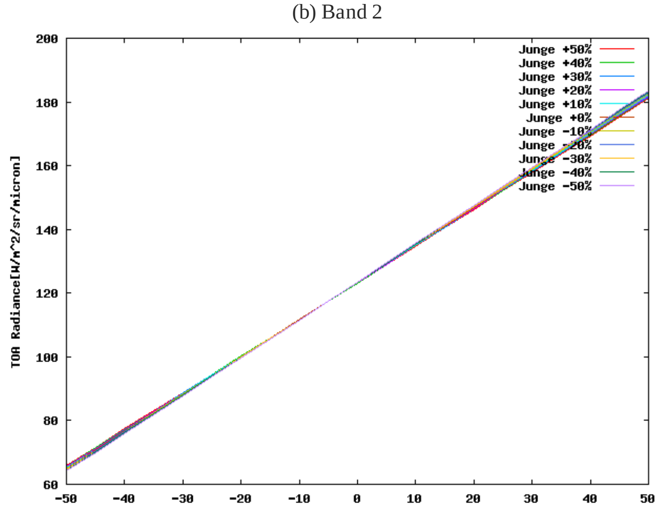

(c)Band 3

Fig. 3. Results from sensitivity analysis on TOA radiance with constant optical depth and the variables of surface reflectance and Junge parameter

On the other hand, Figure 3 (c) shows the results from sensitivity analysis for Band 3.

Meanwhile TOA radiance calculated with constant Junge parameter and with variables of atmospheric optical depth and surface reflectance is shown in Figure 4. Figure 4 (a) is for Band 1 while Figure 4 (b) is for Band 2. Furthermore, Figure 4 (c) is for Band 3.

On the other hand, TOA radiance calculated with constant surface reflectance and with variables of atmospheric optical depth and Junge parameter is shown in Figure 5. Figure 5 (a) is for Band 1 while Figure 5 (b) is for Band 2. In addition, Figure 5 (c) is for Band 3.

As a conclusion, it is confirmed that surface reflectance is most influencing factor on TOA radiance. When the atmospheric optical depth is small, then Junge parameter is influencing.

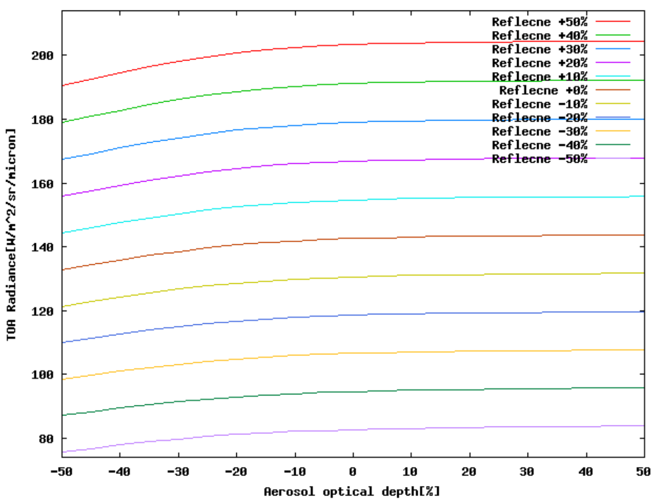

(a)Band 1

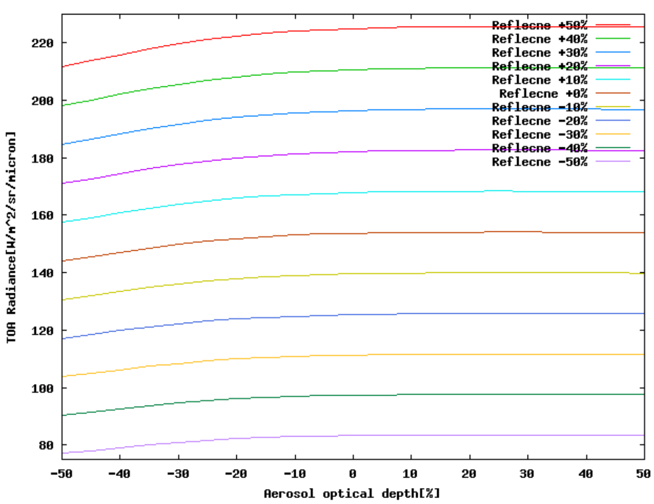

(b)Band 2

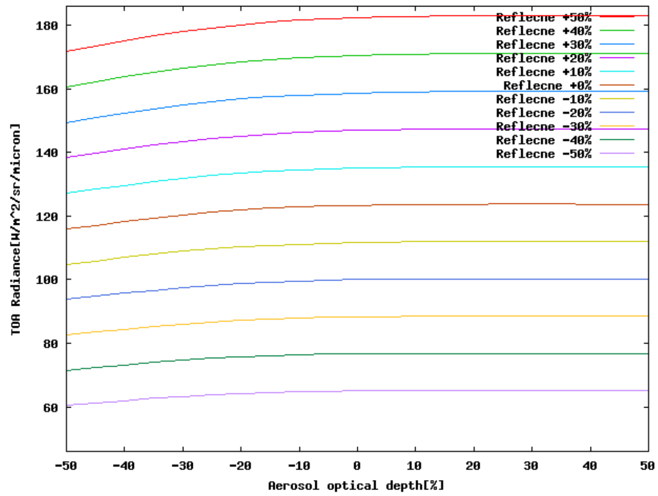

(c)Band 3

Fig. 4. Results from sensitivity analysis on TOA radiance with constant Junge parameter and with variables of optical depth surface reflectance

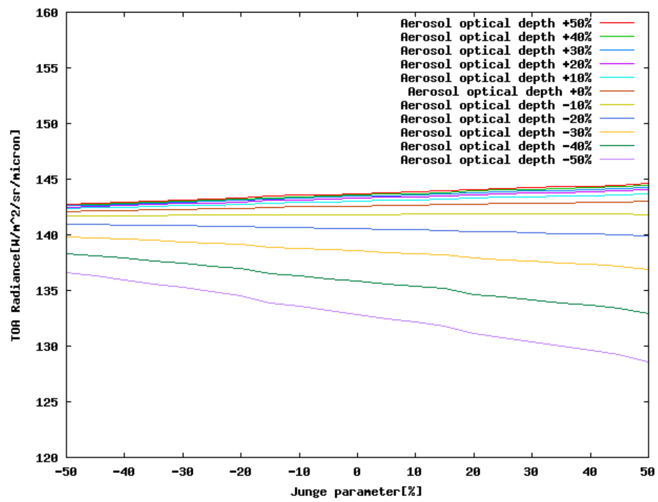

(a)Band 1

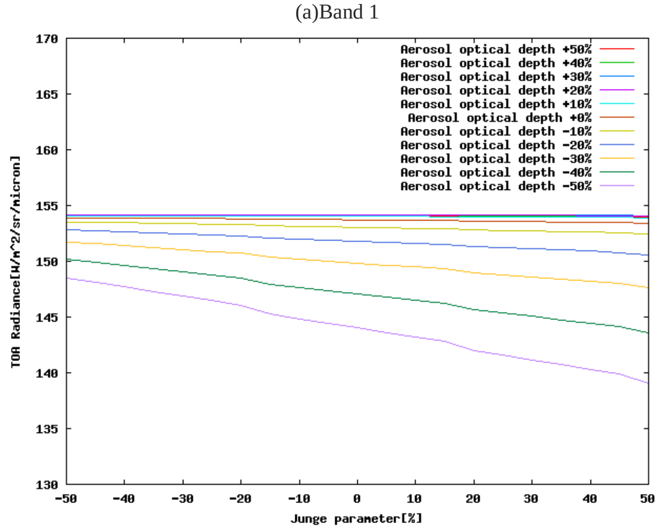

(b)Band 2

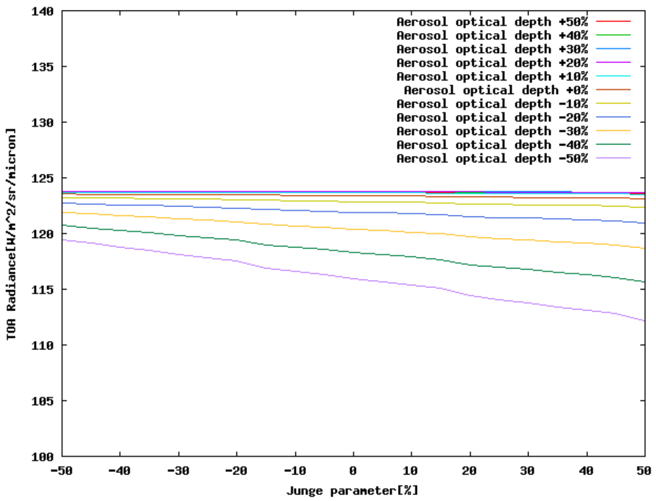

(c)Band 3

Fig. 5. Results from sensitivity analysis on TOA radiance with constant Surface reflectance and with the variables of optical depth and Junge parameter

C. Error Analysis

Error analysis is conducted with +/-5 % of intentional error on surface reflectance.

RCC

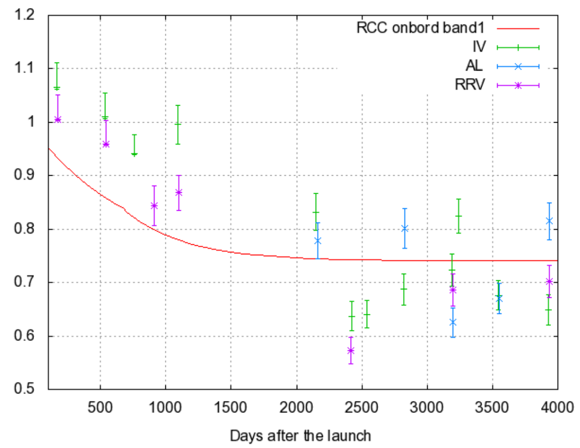

(a)Band 1

RCC

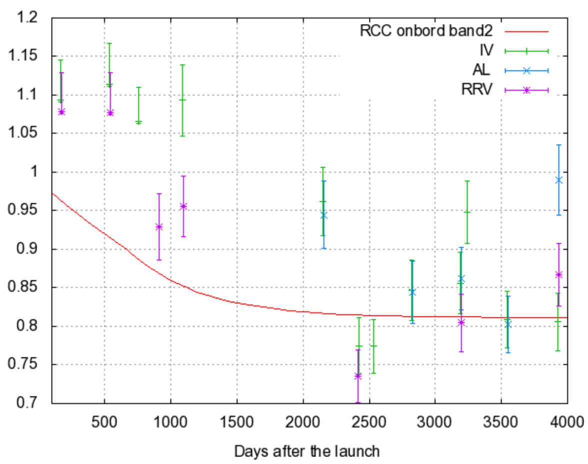

(b)Band 2

RCC

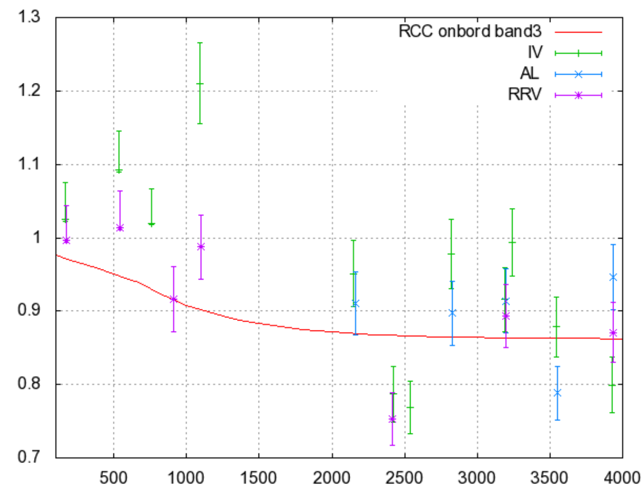

(c)Band 3

Fig. 6. Results from error analysis of vicarious calibration

Figure 6 (a), (b), (c) shows RCC with +/-5% of error bar of Band 1, 2, and 3, respectively. From the error analysis, it is found that +/-5% of surface reflectance error corresponds to -3.75% to +4.54% of TOA radiance error. It is also found that 75% to 91% of vicarious calibration error is caused by surface reflectance error.

D. Discrepancy between Onboard Calibration Coeffieint and Vicairous Clabration Coefficient

Red solid lines in Figure 6 show RCC derived from Onboard Calibration: OBC data while green, blue and purple lines show vicarious calibration coefficients with error bars.

Therefore, discrepancy between RCC derived from OBC data and vicarious calibration data is evaluated with error bars. Figure 7 shows the evaluated result of discrepancy between RCCs in terms of Root Mean Square: RMS error.

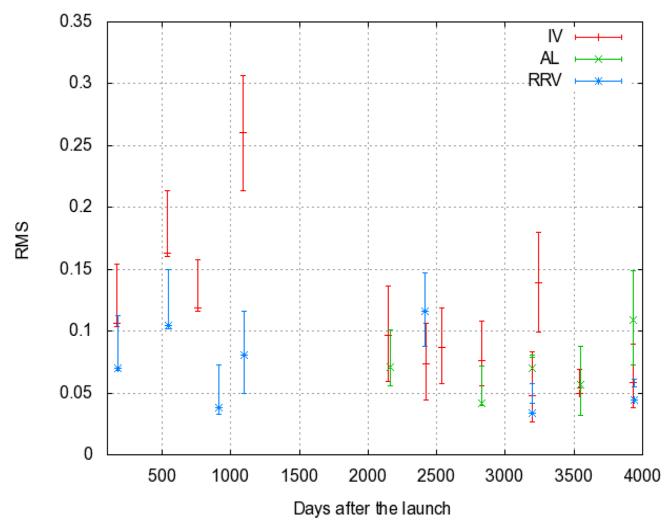

Fig. 7. Discrepancy between RCCs in terms of Root Mean Square: RMS error.

RMS error of the vicarious calibration coefficients is summarized with its mean and +/-5 % of surface reflectance error as shown in Table 4.

TABLE IV. RMS ERROR OF THE VICARIOUS CALIBRATION COEFFICIENTS IS SUMMARIZED WITH ITS MEAN AND +/-5 % OF SURFACE REFLECTANCE ERROR

RMS	Mean	5%	-5%
IV	0.10634	0.12903	0.10036
AL	0.06976	0.08648	0.06737
RRV	0.06961	0.09067	0.07409

Furthermore, vicarious calibration coefficients calculated with maximum surface reflectance for each band as well as averaged value are shown in Table 5.

Through these error analyses, it is found that the most influencing factor is surface reflectance. The most significant 75 to 91% of vicarious calibration coefficients error is due to surface reflectance followed by atmospheric optical depth and Junge parameter. Therefore, we have to care about surface reflectance measuring accuracy followed by atmospheric optical depth (aerosol refractive index, and water vapor and ozone absorption) and Junge parameter (aerosol size distribution).

TABLE V. VICARIOUS CALIBRATION COEFFICIENTS CALCULATED WITH MAXIMUM SURFACE REFLECTANCE FOR EACH BAND AS WELL AS AVERAGED VALUE

MAX	band1	band2	band3	average
IV	4.15	4.55	4.72	4.47
AL	4.37	4.66	4.77	4.6
RRV	4.32	4.6	4.74	4.55
average	4.28	4.6	4.74	4.54
MIN	band1	band2	band3	average
IV	-3.15	-3.45	-3.59	-3.4
AL	-4.36	-4.66	-4.77	-4.59
RRV	-3.09	-3.3	-3.43	-3.27
average	-3.53	-3.8	-3.93	-3.75

IV. CONCLUSION

Sensitivity analysis and error of reflectance based vicarious calibration with estimated aerosol refractive index and size distribution derived from measured solar direct and diffuse irradiance as well as measured surface reflectance is conducted for solar reflective channels of mission instruments onboard remote sensing satellites.

The most significant 75 to 91% of vicarious calibration coefficients error is due to surface reflectance followed by atmospheric optical depth and Junge parameter. Therefore, we have to care about surface reflectance measuring accuracy followed by atmospheric optical depth (aerosol refractive index, and water vapor and ozone absorption) and Junge parameter (aerosol size distribution).

As a conclusion, it is confirmed that surface reflectance is most influencing factor on TOA radiance. When the atmospheric optical depth is small, then Junge parameter is influencing.

ACKNOWLEDGMENT

The author would like to thank Mr. Kntaro Oya for his efforts through experiments and simulations.

REFERENCES

[1] Arai K., Preliminary assessment of radiometric accuracy for MOS-1 sensors, International Journal of Remote Sensing, 9, 1, 5-12, 1988.

[2] Barker, JL, SK Dolan, et al., Landsat-7 mission and early results, SPIE, 3870, 299-311, 1999.

[3] Barnes, RA, EEEplee, et al., Changes in the radiometric sensitivity of SeaWiFS determined from lunar and solar based measurements, Applied Optics, 38, 4649-4664, 1999.

[4] Gellman, DI, SF Biggar, et al., Review of SPOT-1 and 2 calibrations at White Sands from launch to the present, Proc. SPIE, Conf.No.1938, 118-125, 1993.

[5] Folkman, MA, S.Sandor, et al., Updated results from performance characterization and calibration of the TRWIS III Hyperspectral Imager, Proc. SPIE, 3118-17, 142, 1997.

[6] Hagolle, O., P.Galoub, et al., Results of POLDER in-flight calibration, IEEE Trans. On Geoscience and Remote Sensing, 37, 1550-1566, 1999.

[7] Thome, K., K. Arai, S. Tsuchida and S. Biggar, Vicarious calibration of ASTER via the reflectance based approach, IEEE transaction of GeoScience and Remote Sensing, 46, 10, 3285-3295, 2008.

[8] Cosnefroy, H., M.Leroy and X.Briottet, Selection and characterization of Saharan and Arabian Desert sites for the calibration of optical satellite sensors, Remote Sensing of Environment, 58, 110-114, 1996.

[9] Arai, K., In-flight test site cross calibration between mission instruments onboard same platform, Advances in Space Research, 19, 9, 1317-1328, 1997.

AUTHORS PROFILE

Kohei Arai, He received BS, MS and PhD degrees in 1972, 1974 and 1982, respectively. He was with The Institute for Industrial Science and Technology of the University of Tokyo from April 1974 to December 1978 also was with National Space Development Agency of Japan from January, 1979 to March, 1990. During from 1985 to 1987, he was with Canada Centre for Remote Sensing as a Post Doctoral Fellow of National Science and Engineering Research Council of Canada. He moved to Saga University as a Professor in Department of Information Science on April 1990. He was a councilor for the Aeronautics and Space related to the Technology Committee of the Ministry of Science and Technology during from 1998 to 2000. He was a councilor of Saga University for 2002 and 2003. He also was an executive councilor for the Remote Sensing Society of Japan for 2003 to 2005. He is an Adjunct Professor of University of Arizona, USA after 1998. He also is Vice Chairman of the Commission “A” of ICSU/COSPAR after 2008. He wrote 30 books and published 492 journal papers

Contradiction Resolution of Competitive and Input Neurons to Improve Prediction and Visualization Performance

Ryotaro Kamimura
IT Education Center and Graduate School of Science and Technology
Tokai University, 1117 Kitakaname, Hiratsuka, Kanagawa, Japan
ryo@keyaki.cc.u-tokai.ac.jp

***Abstract*—In this paper, we propose a new type of information-theoretic method to resolve the contradiction observed in competitive and input neurons. For competitive neurons, contradiction between self-evaluation (individuality) and outer-evaluation (collectivity) exists, which is reduced to realize the self-organizing maps. For input neurons, there exists contradiction between the use of many and few input neurons. We try to realize a situation where as many input neurons as possible are used, and at the same time, another where only a few input neurons are used. This contradictory situation can be resolved by viewing input neurons on different levels, namely, the individual and average level. We applied contradiction resolution to two data sets, namely, the Japanese short term economy survey (Tankan) and Dollar-Yen exchange rates. In both data sets, we succeeded in improving the prediction performance. Many input neurons were used on average, but a few input neurons were only taken for each input pattern. In addition, connection weights were condensed into a small number of distinct groups for better prediction and interpretation performance.**

Keywords—contradiction resolution; self- and outer-evaluation; visualization; self-organizing maps; dependent input neuron selection

I. INTRODUCTION

A. Contradiction Resolution

We have so far introduced contradiction resolution for neural networks [1], [2]. We believe that neural networks can be viewed from multiple points of view. If contradiction exits between the different points of view, it should be reduced as much as possible. An example of contradiction is two types of evaluation for a neuron [2], namely, self- and outer-evaluation. In self-evaluation, a neuron is evaluated for itself without considering the other neurons. On the other hand, in outer-evaluation, the neuron can be evaluated by all the other neurons. If contradiction between self- and outer-evaluation exists, this contradiction should be reduced as much as possible.

Contradiction resolution has previously been applied to the self-organizing maps (SOM) [3], [4], [5]. In particular, it has been used to improve the visualization and clarification of class structure. Roughly speaking, outer-evaluation corresponds to cooperation between neurons, which is not considered in self-evaluation. Thus, the self-organizing maps can be realized by minimizing contradiction between self- and outer-evaluation.

When we applied the method to the SOM, we focused on the extraction of clear class structure. The SOM is well-known and has been established as one of the main techniques in the visualization and interpretation of neural networks. Though the SOM has a good reputation in visualization and interpretation, we have had serious difficulty in extracting useful information from the knowledge obtained. Thus, a number of different types of methods have been developed to clarify SOM knowledge, [6], [7], [8], [9], [10], [11], [12]. In addition, there have been many other methods to create more interpretable connection weights by changing the learning procedures [13], [14], [15], [16]. However, we cannot say that SOM knowledge can be easily interpreted with these methods. Contradiction resolution has been previously introduced to clarify class structure or to create more interpretable connection weights, because the characteristics shared by self- and outer-evaluation tend to be enhanced [2].

B. Contradiction in Input Neurons

The above example of contradiction is concerned with competitive (output) neurons in the SOM. We have found that in addition to competitive neurons, contradiction can be found in input neurons in terms of their types of responses and the number of input neurons.

First, we try to resolve contradiction between the actual and expected responses of input neurons. We have found several cases where only specific input neurons among many tend to respond to all input patterns. For example, in our experiments in this paper, the most important input neuron (winning neuron) tended to respond to specific data (period), irrespectively of different input patterns. Because these specific input neurons are only used in learning, we do not have any way to examine whether the other input neurons have a role in learning. To examine the roles of all available input neurons, we need to develop a method to force all input neurons to play a role in learning. Thus, we need to resolve contradiction between the use of specific and all input neurons.

However, we can immediately point out another contradiction in input neurons, namely, contradiction between many and few neurons. If we interpret input neurons as input variables, this contradiction is related to the variable selection method widely used in machine learning [17], [18], [19]. Using variable selection, we can more easily interpret data and internal representations, reducing the computational time and storage. In addition, it is widely believed that reducing the number of input variables (neurons) is effective in improving prediction performance [17]. Thus, we have contradiction between a few and many neurons to be actually used in learning. We thus try to use many input neurons while at the same time using only a few. To resolve contradiction between many and few input neurons, we introduce dependent input neuron selection. In dependent input neuron selection, for a given input pattern, a few input neurons are taken, while for another input pattern, a few but different input neurons are used. For individual input patterns, the number of input neurons is small. On the other hand, many input neurons are used on the whole.

C. Outline

In Section 2, we first explain the concept of contradiction resolution in the order of competitive neuron, input neurons and the number of input neurons. By using the Kullback-Leibler divergence, we formulate contradiction between self- and outer-evaluation for competitive neurons. Then, contradiction between actual and expected responses of input neurons is formulated. Contradiction in the number of input neurons is resolved by introducing dependent input neuron selection. We applied the method to two data sets, namely, the short term economic survey and the Dollar-Yen exchange rates. In both data sets, prediction performance was improved, condensing connection weights into a few groups. In addition, the first, the second and the third winners responded to a variety of input patterns.

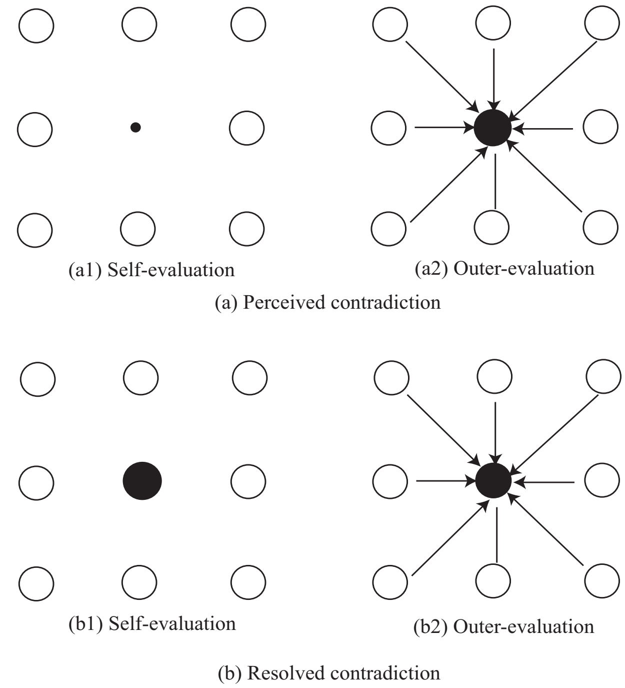

Fig. 1. Contradiction resolution between self- and outer-evaluation for competitive neurons.

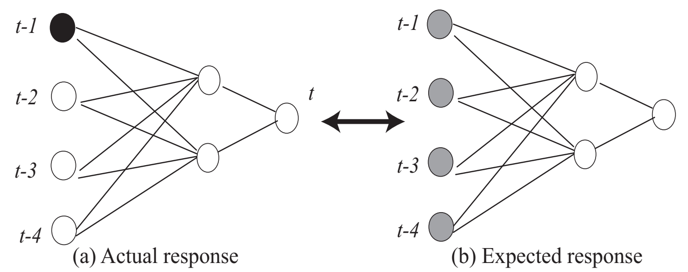

Fig. 2. Contradiction resolution between actual and expected responses of input neurons.

II. Theory and Computational Methods

A. Contradiction Resolution

We consider learning to be a process of contradiction resolution. We here propose three types of contradiction resolution processes, namely, contradiction resolution in terms of competitive neurons, input neurons and the number of input neurons.

1) Competitive Neurons: Contradiction resolution [1], [2] has been introduced to produce the self-organizing maps. In the self-organizing maps, neurons behave collectively and individual neurons must imitate those collective behaviors. Figure 1 shows the process of contradiction resolution. In Figure 1(a1), a neuron at the center is self-evaluated to fire; the firing rate of the neuron is determined by the neuron itself. On the other hand, in Figure 1(a2), a neuron at the center is outer-evaluated; the firing rate of the neuron is determined by all surrounding neurons. Because the firing rates obtained by the self- and outer-evaluation are low and high, respectively, we have contradiction between self- and outer-evaluation. Figure 1(b) shows an example of resolved contradiction. As shown in Figure 1(b1), the firing rate by the self-evaluation is forced to match the level by the outer-evaluation in Figure 1(b2). Thus, contradiction between self- and outer-evaluation is finally resolved.

2) Input Neurons: For input neurons, we think that there is contradiction between actual and expected responses. Let's look at an example to explain concretely this contradiction. We here explain a problem of the data used in our experiments in Section 3. We chose the time series data for demonstrating our method, because we found that the $t-1$th input neuron was mainly used for predicting the tth period, as in Figure 2(a1). This means that the input neuron responded mainly to the immediately previous step for predicting the present step. We found this fact in both data sets in this paper. If it is possible to take into account many input neurons or more previous steps, it may be possible to improve the prediction performance. More concretely, we should consider the $t-2$, $t-3$ and $t-4$ as well as the $t-1$th step. Thus, we have a contradiction that the actual responses of input neurons are biased toward the immediately previous step, while the expected responses are more uniform responses of input neurons. This contradiction between actual (biased) responses and expected (uniform) ones must be resolved, as shown in Figure 2(b).

3) Number of Input Neurons: Finally, we have the other contradiction. As mentioned above, we expect that input neurons respond more uniformly to input patterns. However, for better prediction performance, one of the more conventional methods is to reduce the number of input variables (neurons), namely, variable subsection selection, as shown in Figure 3(b). This is contrary to the state we try to achieve in Figure 2(b). This contradiction is resolved by introducing dependent input neuron selection, as shown in Figure 3(c). In dependent input neuron selection, a smaller number of input neurons are used, but they are chosen depending on input patterns. As shown in

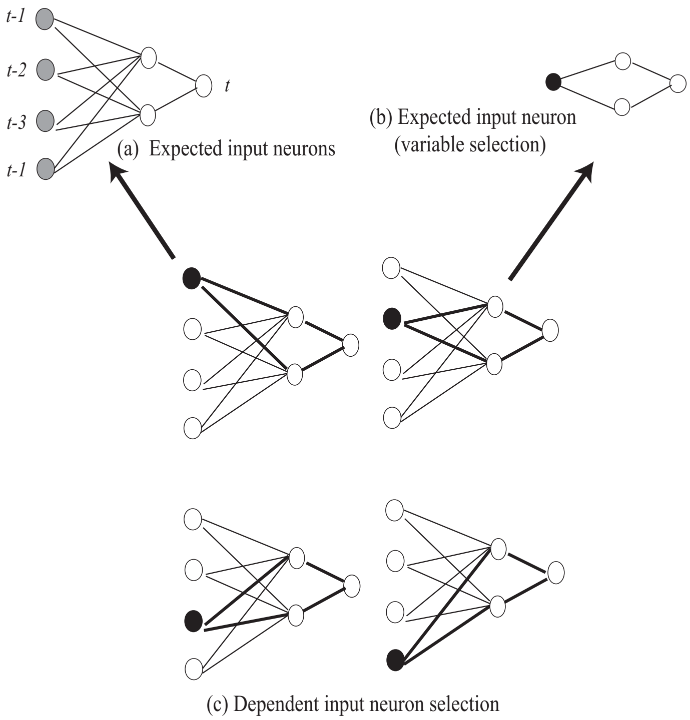

Fig. 3. Contradiction resolution by dependent input neuron selection.

Figure 3(c), for each neural network, only one input neuron is used. However, a different input neuron is used for each network in Figure 3(c). When we average these firing rates of four input neurons, they become the same for all input patterns in Figure 3(a). Thus, a smaller number of input neurons can be expected for some input neurons with averaged uniform firing rates.

B. Contradiction Resolution for Competitive Neurons

First, we consider contradiction resolution for competitive neurons in Figure 4. We suppose that a neuron, for example, a neuron in the middle of network in Figure 4, is evaluated by itself (self-evaluation) and evaluated by the other neurons (outer-evaluation). If any contradiction between self- and outer-evaluation exits, it should be reduced as much as possible. In terms of firing rates, if the firing rates by self-evaluation are different from those by outer-evaluation, this difference should be as small as possible.

1) Self- and Outer-Evaluation: Let us explain how to compute outputs from competitive neurons and input patterns in Figure 4. The sth input pattern can be represented by $\mathbf{x}^s = [x_1^s, x_2^s, \cdots, x_L^s]^T,\ s = 1, 2, \cdots, S$. Connection weights into the jth competitive neuron are computed by $\mathbf{w}_j = [w_{1j}, w_{2j}, \cdots, w_{Lj}]^T,\ j = 1, 2, \ldots, M$. Now, we can compute the firing rates by self- and outer-evaluation. A neuron's firing rates by self-evaluation can be defined by using the outputs from the neuron. Then, the jth competitive neuron output without considering the other neurons can be computed by

$$v_j^s = \exp\left(-\frac{\sum_{k=1}^{L}(x_k^s - w_{kj})^2}{2\sigma_{\beta_1}^2}\right). \tag{1}$$

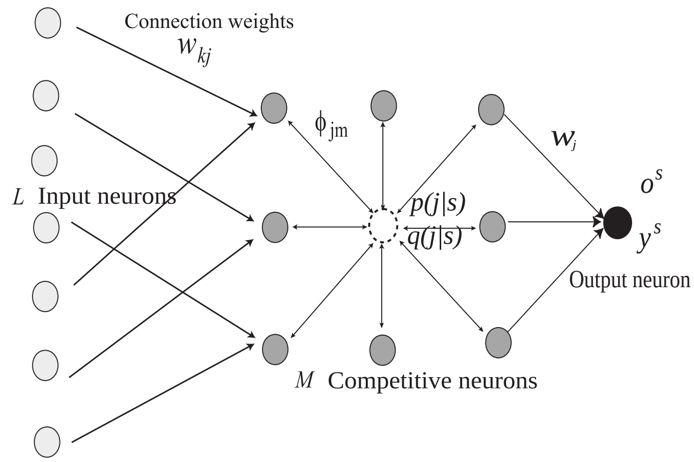

Fig. 4. Network architecture for contradiction resolution.

where $\mathbf{x}^s$ and $\mathbf{w}_j$ are supposed to represent L-dimensional input and weight column vectors, where L denotes the number of input neurons. The parameter σ_{β_1} is computed by

$$\sigma_{\beta_1} = \frac{1}{\beta_1}, \tag{2}$$

where β_1 is larger than zero. Thus, the firing rate by self-evaluation is computed by

$$p(j \mid s) = \frac{\exp\left(-\frac{\sum_{k=1}^{L}(x_k^s - w_{kj})^2}{2\sigma_{\beta_1}^2}\right)}{\sum_{m=1}^{M}\exp\left(-\frac{\sum_{k=1}^{L}(x_k^s - w_{km})^2}{2\sigma_{\beta_1}^2}\right)}. \tag{3}$$

The output of a neuron by outer-evaluation is determined by the sum of all outputs of all the other neurons. We suppose that the result by outer-evaluation does not contain that by self-evaluation; given this, we have the final output by the outer-evaluation

$$z_j^s = \sum_{m=1}^{M}\phi_{jm}v_m^s - v_j^s, \tag{4}$$

where ϕ_{jm} denotes the relation between the jth and mth neuron. When we apply the method to the self-organizing maps, this corresponds to the neighborhood function. Then, the firing rate by the outer-evaluation is defined by

$$q(j \mid s) = \frac{z_j^s}{\sum_{m=1}^{M} z_m^s}. \tag{5}$$

2) Reducing Contradiction: Contradiction resolution aims to reduce contradiction between self- and outer-evaluation. We use the Kullback-Leibler divergence to represent this contradiction. Using the Kullback-Leibler divergence, contradiction is defined by

$$\mathrm{C}_1 = \sum_{s=1}^{S}p(s)\sum_{j=1}^{M}p(j \mid s)\log\frac{p(j \mid s)}{q(j \mid s)}. \tag{6}$$

In addition to this contradiction, we have quantization errors between connection weights and input patterns

$$\mathrm{Q}_1 \quad = \quad \sum_{s=1}^{S}p(s)\sum_{j=1}^{M}p(j \mid s)\sum_{k=1}^{L}(x_k^s - w_{kj})^2. \tag{7}$$

To realize minimum contradiction in terms of contradiction ratio and quantization errors, first, we try to minimize the KL divergence with fixed quantization errors. Then, we have the optimal firing rates

$$p^*(j \mid s) = \frac{q(j \mid s)\exp\left(-\frac{\sum_{k=1}^{L}(x_k^s - w_{kj})^2}{2\sigma_{\beta_1}^2}\right)}{\sum_{m=1}^{M} q(m \mid s)\exp\left(-\frac{\sum_{k=1}^{L}(x_k^s - w_{km})^2}{2\sigma_{\beta_1}^2}\right)}. \quad (8)$$

By substituting this optimal firing rate $p^*(j \mid s)$ for $p(j \mid s)$, we have the free energy:

$$\begin{aligned} \mathrm{F}_1 &= -2\sigma_{\beta_1}^2 \sum_{s=1}^{S} p(s) \log \sum_{j=1}^{M} q(j \mid s) \\ &\times \exp\left(-\frac{\sum_{k=1}^{L}(x_k^s - w_{kj})^2}{2\sigma_{\beta_1}^2}\right). \end{aligned} \quad (9)$$

The free energy can be expanded into

$$\begin{aligned} \mathrm{F}_2 &= \sum_{s=1}^{S} p(s) \sum_{j=1}^{M} p^*(j \mid s) \sum_{k=1}^{L} (x_k^s - w_{kj})^2 \\ &+2\sigma_{\beta_1}^2 \sum_{s=1}^{S} p(s) \sum_{j=1}^{M} p^*(j \mid s) \log \frac{p^*(j \mid s)}{q(j \mid s)}. \end{aligned} \quad (10)$$

Thus, we actually minimize KL divergence as well as quantization errors. By differentiating the free energy, we have the re-estimation equation

$$\mathbf{w}_j = \frac{\sum_{s=1}^{S} p^*(j \mid s)\mathbf{x}^s}{\sum_{s=1}^{S} p^*(j \mid s)}. \quad (11)$$

C. Contradiction for Input Neurons

As mentioned above, we try to use as many input neurons as possible. On the other hand, only a specific input neuron responds to the input patterns in our data. This contradiction between the actual (biased) and expected (uniform) responses of input neurons must be resolved as much as possible. For measuring contradiction, we must compute the output from the kth input neuron.

Let us now compute the output from the kth input unit. The output from the kth input neuron is defined by

$$y_k^s = \exp\left(-\frac{\sum_{j=1}^{M}(x_k^s - w_{kj})^2}{2\sigma_{\beta_2}^2}\right) \quad (12)$$

Then, the firing rate is computed by

$$p(k \mid s) = \frac{\exp\left(-\frac{\sum_{j=1}^{M}(x_k^s - w_{kj})^2}{2\sigma_{\beta_2}^2}\right)}{\sum_{l=1}^{L}\exp\left(-\frac{\sum_{j=1}^{M}(x_l^s - w_{lj})^2}{2\sigma_{\beta_2}^2}\right)} \quad (13)$$

Because we try to achieve uniform responses of input neurons, the expected firing rate should be determined by $1/L$. Thus, we should maximize the entropy to achieve this uniform distribution

$$C_2 = \sum_{s=1}^{S} p(s) \sum_{j=1}^{M} p(k \mid s) \log p(k \mid s). \quad (14)$$

We can define two free energies for input and competitive neurons and we must minimize two types of free energy at the same time.

$$\begin{aligned} F &= -2\sigma_{\beta_1}^2 \sum_{s=1}^{S} p(s) \log \sum_{j=1}^{M} q(j \mid s) \exp\left(-\frac{\| \mathbf{x}^s - \mathbf{w}_j \|^2}{2\sigma_{\beta_1}^2}\right) \\ &-2\sigma_{\beta_2}^2 \sum_{s=1}^{S} p(s) \log \sum_{k=1}^{L} \exp\left(-\frac{\sum_{j=1}^{M}(x_k^s - w_{kj})^2}{2\sigma_{\beta_2}^2}\right) \end{aligned} \quad (15)$$

For simplification, we suppose that two spread parameters β_1 and β_2 are equal. Then, by differentiating the free energy, we have the re-estimation rule

$$\mathbf{w}_j = \frac{\sum_{s=1}^{S}(p^*(j \mid s) + p(k \mid s))\mathbf{x}^s}{\sum_{s=1}^{S}(p^*(j \mid s) + p(k \mid s))}. \quad (16)$$

D. Contradiction resolution by dependent input neuron selection

We have known that the reduction of the number of input neurons (variables) can be used to improve prediction performance [17]. This reduction is contrary to the previous contradiction resolution, which aimed to achieve the uniform responses of input neurons. We reduce this contradiction by introducing dependent input neuron selection. This method aims to choose an input neuron depending on a given input pattern. Though a small number of input neurons are used for the input patterns, they can be different for different input patterns. However, on average, they are uniformly used. Thus, the dependent input neuron selection can solve the contradiction between biased and uniform responses of input neurons. Figure 5 shows how to choose the input neurons according to the importance of the neurons.

Let us compute the output from the kth input unit. The output from the kth input neuron is defined by

$$v_k^s = \exp\left(-\frac{\sum_{j=1}^{M}(x_k^s - w_{kj})^2}{2\sigma_{\beta_2}^2}\right) \quad (17)$$

When the sth input pattern is presented, we first determine the winner g_1

$$g_1 = \mathrm{argmax}_k\, v_k^s. \quad (18)$$

Then, based on this winner, we can obtain a winning ranking, as shown in Figure 5,

$$g_1 < g_2 < \ldots < g_L. \quad (19)$$

Neurons of this ranking should keep the following relation:

$$v_{g_1}^s > v_{g_2}^s > \ldots > v_{g_L}^s. \quad (20)$$

By using this ranking, we can define the output from the jth neuron with only r winning input neurons

$$v_j^s(r) = \exp\left(-\frac{\sum_{k=1}^{r}(x_{g_k}^s - w_{g_k j})^2}{2\sigma_{\beta_2}^2}\right), \quad (21)$$

where r is a specified number of input neurons and less than or equal to the number of input neurons. By using this output, we obtain the outputs by outer-evaluation for the r input neurons

$$z_j^s(r) = \sum_{m=1}^{M} \phi_{jm} v_m^s(r) - v_j^s(r), \quad (22)$$

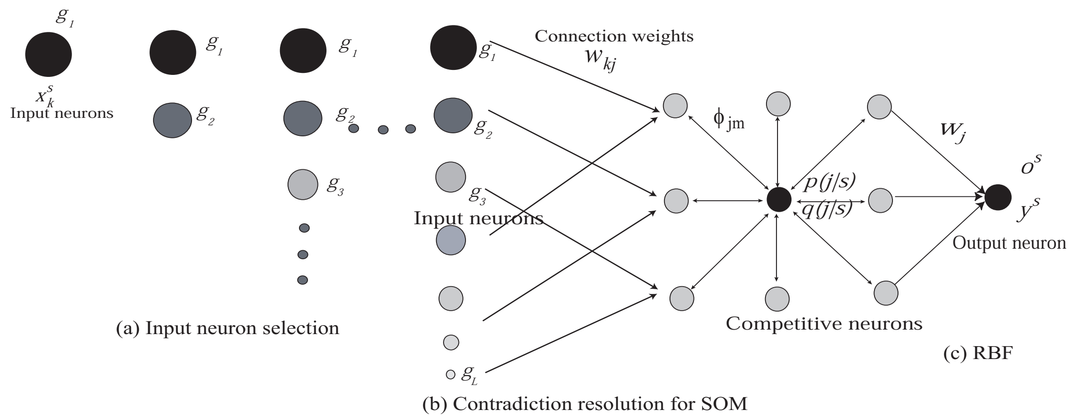

Fig. 5. Input neuron selection.

The firing rates are defined by

$$q(j \mid s; r) = \frac{z_j^s(r)}{\sum_{m=1}^{M} z_m^s(r)}. \tag{23}$$

By using these firing probabilities, we have

$$p^*(j \mid s) = \frac{q(j \mid s; r) \exp\left(-\frac{\sum_{k=1}^{r}(x_{g_k}^s - w_{g_k j})^2}{2\sigma_{\beta_2}^2}\right)}{\sum_{m=1}^{M} q(j \mid s; r) \exp\left(-\frac{\sum_{k=1}^{r}(x_{g_k}^s - w_{g_k j})^2}{2\sigma_{\beta_2}^2}\right)}. \tag{24}$$

We minimize two types of free energy at the same time:

$$\begin{aligned} F &= -2\sigma_{\beta_1}^2 \sum_{s=1}^{S} p(s) \log \sum_{j=1}^{M} q(j \mid s; r) \\ &\quad \times \exp\left(-\frac{\sum_{k=1}^{r}(x_k^s - w_{kj})^2}{2\sigma_{\beta_1}^2}\right) \\ &\quad -2\sigma_{\beta_2}^2 \sum_{s=1}^{S} p(s) \\ &\quad \times \log \sum_{k=1}^{L} \exp\left(-\frac{\sum_{j=1}^{M}(x_k^s - w_{kj})^2}{2\sigma_{\beta_2}^2}\right). \end{aligned} \tag{25}$$

By differentiating the free energy with $\beta_1 = \beta_2$, the re-estimation rule can be computed by

$$\mathbf{w}_j = \frac{\sum_{s=1}^{S}(p^*(j \mid s; r) + p(k \mid s))\mathbf{x}^s}{\sum_{s=1}^{S}(p^*(j \mid s; r) + p(k \mid s))}. \tag{26}$$

Finally, we should note a modification in the experiments. The parameter β_1 is supposed to be equivalent to the parameter β_2 for the easy implementation of our method. However, it is interesting to examine the relations between competitive and input neurons. For this, in the following experiments we slightly change the values of the two to examine the relation between competitive and input neurons. Specifically, the parameter β_2 is defined by

$$\beta_2 = \alpha\beta_1, \tag{27}$$

where α is larger than zero. When the parameter α is smaller, the effect of the input neurons becomes weaker.

III. Results and Discussion

A. Experimental Outline

We here present two experimental results for demonstrating the good performance of our method. We used the mean squared error (MSE) for the testing data to measure the performance. In addition, we computed quantization and topographic errors [20] to measure the quality of the maps. The quantization error is the average error between input patterns and connection weights into the first winner. On the other hand, the topographic error is the percentage of input patterns that are not neighboring neurons.

B. Short-Term Economic Survey (Tankan)

We used the quarterly short-term economic survey of principal enterprise in Japan. This is called ”Tankan.” The data set ranged between March 1983 and December 2012. The training data was between March 1983 and December 2004, and the testing data was between March 2005 and December 2012.

1) Quantitative Evaluation: Table I shows the summary of experimental results for the Tankan data. When the parameter β was 48, the parameter α was 1, and the number of input winners was 4, the MSE was 70.215. When the parameter α was 0.7, the MSE decreased to 66.298. These MSE values were lower than the 85.022 by the SOM and much lower than the 188.319 by the feed-forward selection (FS) of RBF and the 424.849 by Ridge regression (RR) of RBF networks. The quantization error increased from 0.783 by SOM to 1.493 ($\alpha = 1.0$) and to 1.448 ($\alpha = 0.7$). The topographic error increased from 0.012 by SOM to 0.602 ($\alpha = 1.0$) and to 0.988 ($\alpha = 0.7$). Thus, good prediction performance was accompanied by a degradation in map quality.

2) Visual Inspection: Figure 6 (a) shows the Tankan rates by contradiction resolution with $\alpha = 0.7$. The actual rates in blue were close to the predicted ones in red. By SOM in Figure 6(b), differences between actual and predicted ones were slightly larger than those by contradiction resolution. By using the feed-forward selection of RBF networks, differences between actual and predicted rates were larger in the middle of the period in Figure 6(c). By using Ridge regression of RBF networks, Tankan rates fluctuated in the later period in Figure 6(d).

TABLE I. MSE FOR THE TESTING DATA, QUANTIZATION ERRORS (QE) AND TOPOGRAPHIC ERRORS (TE) FOR THE TANKAN DATA BY CONTRADICTION RESOLUTION, SOM, FEED-FORWARD SELECTION (FS) AND RIDGE REGRESSION (RR) OF RBF NETWORKS.

Method	Beta	Alpha	Win	MSE	QE	TE
Contradiction	41	0.7	3	66.298	1.448	0.988
	48	1.0	4	70.215	1.493	0.602
SOM				85.022	0.783	0.012
RBF(FS)				188.319		
RBF(RR)				424.849		

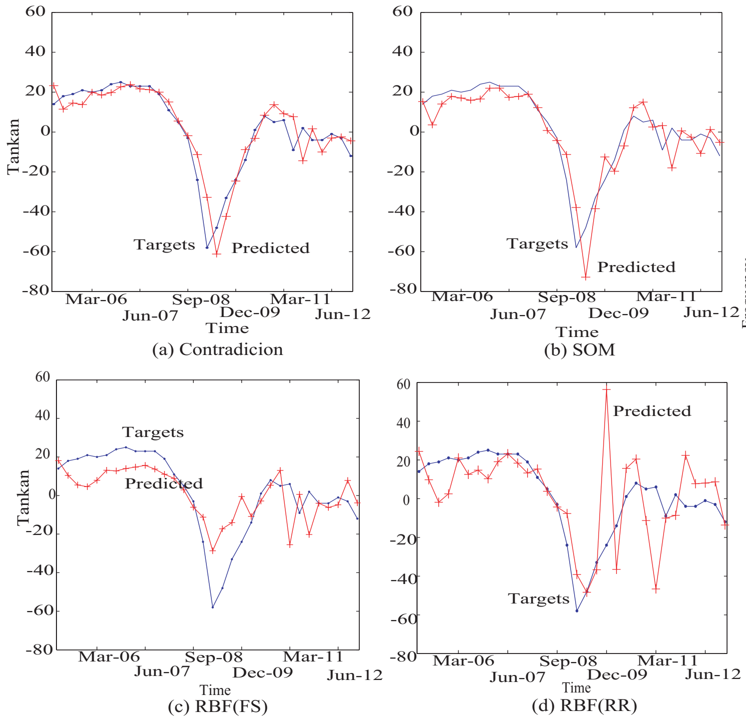

Fig. 6. Tankan rates in blue and predicted values in red by contradiction resolution (a), SOM (b), RBF(FS) (c) and RBF (RR) (d) for 5 by 3 sized map.

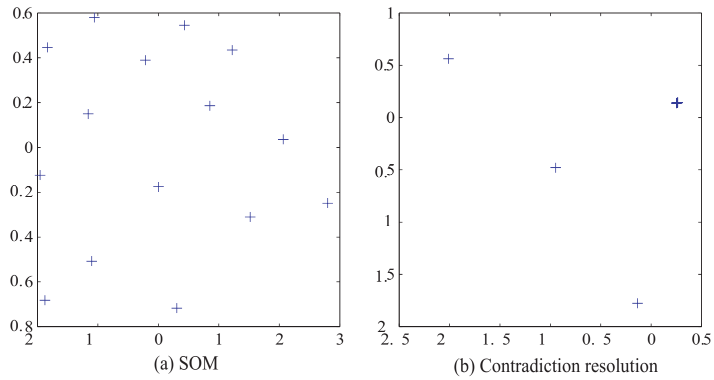

Fig. 7. Results by the principal component analysis (PCA) for connection weights by the SOM (a) and the contradiction resolution (b) for the Tankan data.

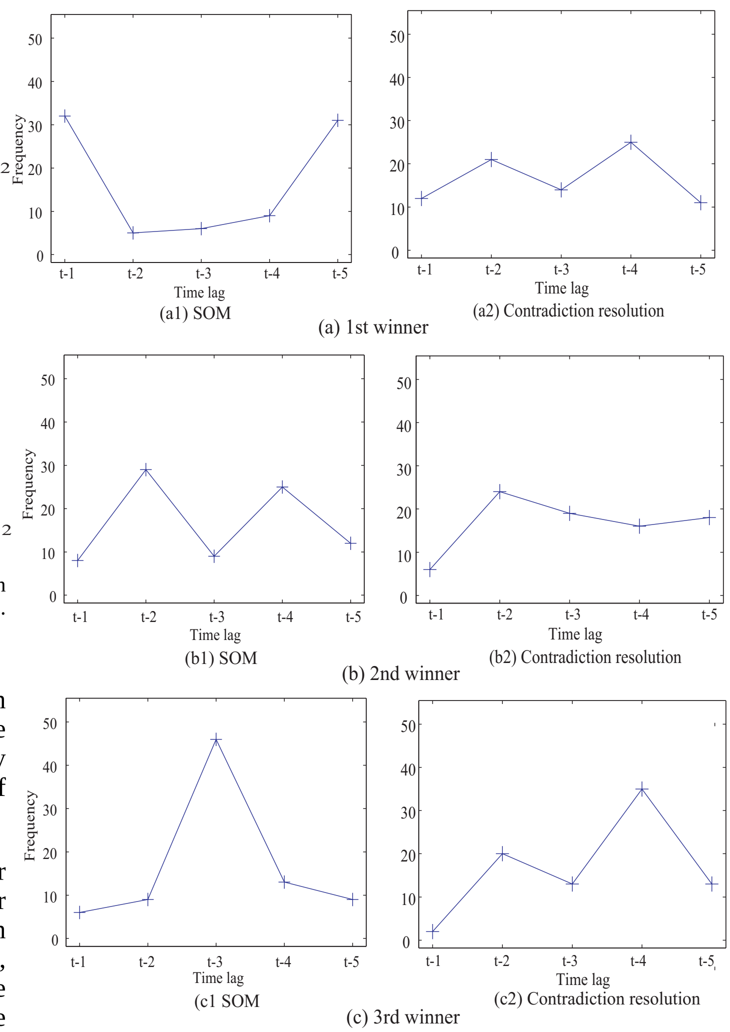

Fig. 8. Frequency of responses by the winners for each time lag for the Tankan data.

Figure 7(b) shows the results of PCA for connection weights by contradiction resolution. Connection weights were condensed into four distinct groups. On the other hand, by using the SOM, no regularity could be seen on the results of PCA in Figure 7(a).

Figure 8(a1) shows to which time lag the first input winner responded by the conventional SOM. The first input winner responded mainly to the $t-1$th and $t-5$th time lag. On the other hand, by contradiction resolution in Figure 8(a2), the first winner tended to respond more uniformly to the time lag. Figure 8(b) shows the response to the time lags by the second winner. The second winner by the SOM responded to the $t-2$th and $t-4$th time lag in Figure 8(b1). On the other hand, the second winner by contradiction resolution responded to the time lags almost uniformly in Figure 8(b2). Figure 8(c) shows the responses by the third winner. The third winner by the SOM responded to the $t-3$th time lag in Figure 8(c1), while the third winner by the contradiction resolution responded mainly to the $t-4$th lag but responded to many time lags (input neurons) in Figure 8(c2) . These results show that by contradiction resolution, many input neurons were used to respond to input patterns.

C. Dollar-Yen Exchange Rate Estimation

1) Experiment Outline: We used the dollar-yen exchange rates during 2012 (for the results of 2011, see [1]). The time lag was ten, meaning that the exchange rate at the tth period was determined by the rates of $t-1$, $t-2$, ..., $t-10$. The training data ranged between January to September, while the testing data ranged from October to December. For comparison, we

TABLE II. THE PARAMETER β AND α, THE NUMBER OF INPUT WINNING NEURONS, MSE FOR THE TESTING DATA, QUANTIZATION ERRORS (QE) AND TOPOGRAPHIC ERRORS (TE) FOR THE DOLLAR-YEN EXCHANGE RATES.

Method	Beta	Alpha	Win	MSE	QE	TE
Contradiction	36	0.5	4	0.122	1.601	0.145
	32	1.0	1	0.182	1.579	0.436
SOM				0.270	0.986	0.073
RBF(FS)				0.233		
RBF(RR)				5.870		

used several conventional methods such as the RBF networks with feed-forward selection and Ridge regression with GCV model selection criteria.

2) Quantitative Evaluation: Table II shows the summary of experimental results when the network size was 5 by 3 for the dollar-yen exchange rates. When the parameter β was 32, the parameter α was 1.0, the number of input winning neurons was one, the MSE was 0.182. When the parameter α was decreased to 0.5, the MSE further decreased to 0.122. The MSE values were much smaller than the 0.270 by SOM, 0.233 by the feed-forward selection of RBF and 5.870 by the Ridge regression of RBF networks. However, quantization errors increased from 0.986 by SOM to 1.579 ($\alpha = 1.0$) and to 1.601 ($\alpha = 0.5$). The topographical errors also increased from 0.073 by SOM to 0.436 ($\alpha = 1.0$) and to 0.145 ($\alpha = 0.5$). The prediction performance was improved at the expense of map quality in terms of quantization and topographic errors.

3) Visual Inspection: Figure 9(a) shows the actual and predicted rates by contradiction resolution with $\alpha = 0.5$. Actual and predicted rates were almost equal for the entire range of the period. When we used the SOM in Figure 9(b), differences between actual and predicted rates became larger as the time went on. By using the feed-forward selection of RBF networks in Figure 9(c), the predicted rates were almost flat for the entire range of the period. By the Ridge regression of RBF networks in Figure 9(d), the differences were relatively small, but they were larger than those by contradiction resolution for the entire range of the period. The experimental results showed that the prediction performance for the entire period was much improved by contradiction resolution.

Figure 10(a) shows the results of PCA for connection weights by contradiction resolution. We can see that connection weights were condensed into one major group with two distinct groups by contradiction resolution. On the other hand, by SOM in Figure 10(b), no regularity could be seen on the results of PCA. We think that the condensation of connection weights into a small number of groups was one of the main reasons for better performance.

Figures 11 (a1), (b1) and (c1) show the frequency of winning input neurons by the conventional SOM. As can be seen in the figures, the first, the second and third winning input neurons responded to the $t-1$th, $t-2$ and $t-3$th time lag by the conventional SOM. On the other hand, the first winning neuron by contradiction resolution in Figure 11(b1) responded to the $t-1$th and $t-5$th time lag mainly. In addition, the second and third winning neuron respond almost uniformly to the time lags in Figure 11 (b2) and (b3). Experimental results showed that the specific responses of input neurons were attenuated and

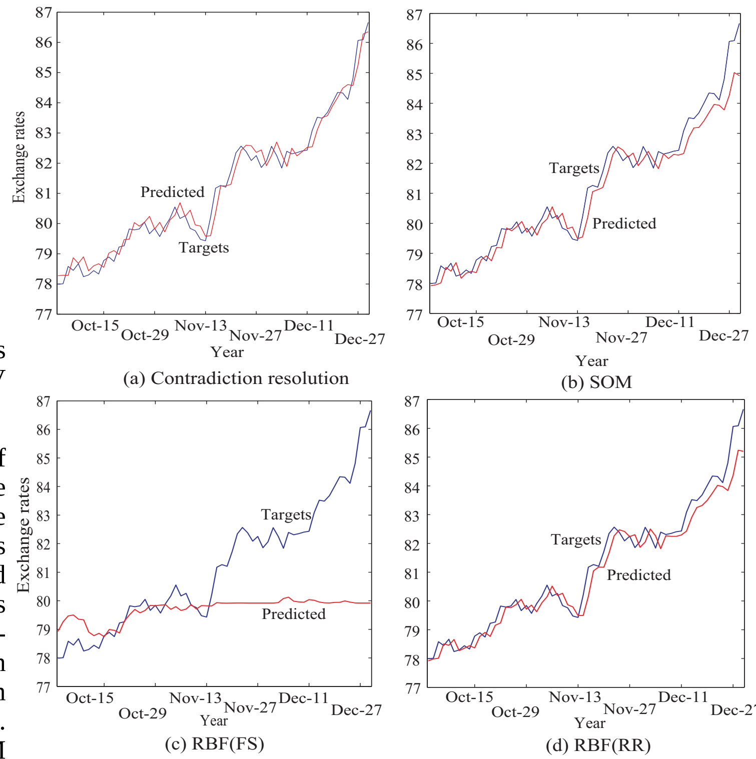

Fig. 9. Dollar-yen exchange rates and predicted values by contradiction resolution (a), SOM (b), RBF(FS) (c) and RBF (RR) (d) for 5 by 3 sized map.

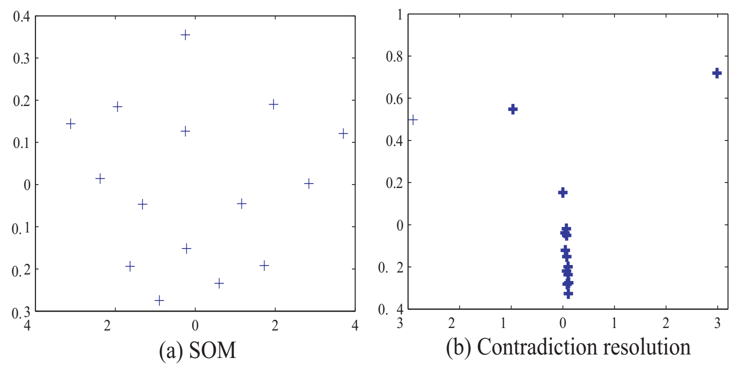

Fig. 10. Results by the principal component analysis (PCA) for connection weights by contradiction resolution (a) , SOM (b) and data itself (c) for Dollar-Yen exchange rates.

input neurons tended to respond to many different time lags. This property was certainly related to improved performance.

D. Discussion

1) Validity of Methods and Experimental Results: In this paper, we have introduced contradiction resolution between self- and outer-evaluation, and between expected and actual responses of input neurons. First, we compute two types of firing rates of a neuron. The first type is computed by self-evaluation. The firing rate is determined by its own responses to input patterns. On the other hand, the firing rate of a neuron is determined by outer-evaluation, namely, other neurons. If contradiction or difference between self- and outer-evaluation exists, this should be reduced as much as possible. The outer-evaluation corresponds to cooperation between competitive

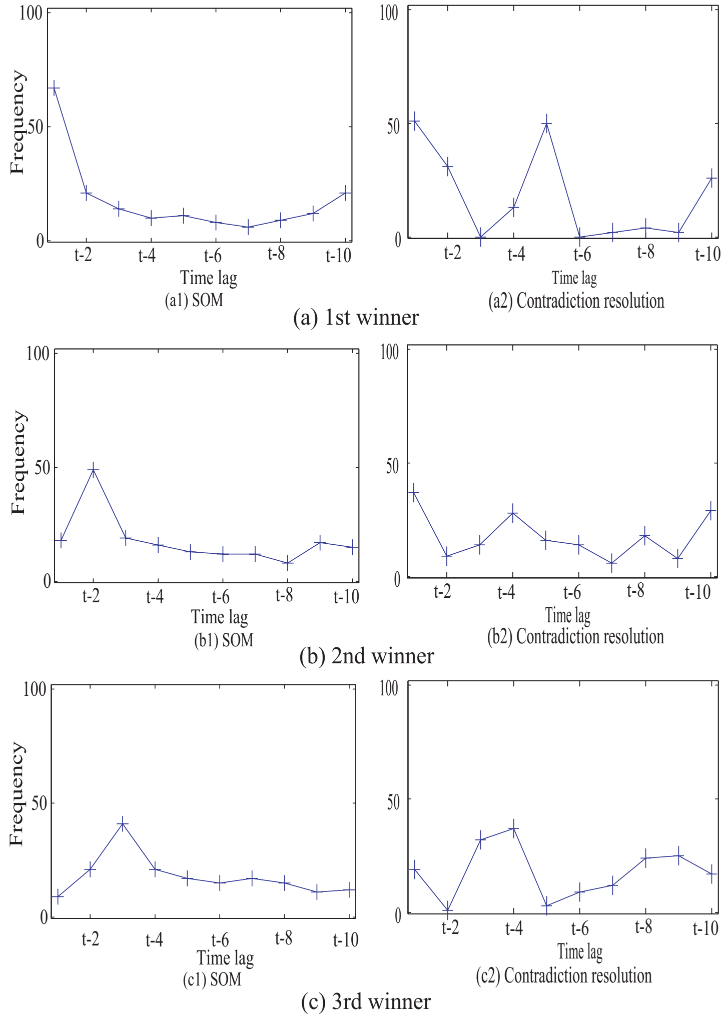

Fig. 11. Frequency of the responses by the winners for each time lag for dollar-yen exchange rates.

neurons. Thus, contradiction resolution between self- and outer-evaluation can be used to realize self-organizing maps.

The second type of contradiction is between actual and expected responses of input neurons. We have found that only specific input neurons respond to input patterns for some problems. The other input neurons are of no use in learning. We tried to use as many input neurons as possible.

However, we have known that to improve the prediction performance, the number of input neurons (variables) should be reduced. This is contradictory to the expected responses we try to achieve. The contradiction can be resolved by introducing dependent input neuron selection. In dependent input neuron selection, a few input neurons are chosen as in the variable selection. However, chosen input neurons can be different, depending on input patterns. Thus, when we see the responses of input neurons for a specific input neuron, few input neurons are used. However, on average, all input neurons can be used.

We applied the method to two data sets, namely, the short term economic survey (Tankan) and dollar-yen exchange rates. In both data sets, when contradiction resolution was introduced, much better performance in terms of MSE for testing data was observed, as in Tables I and II. Better performance was intuitively observed by plotting actual and estimated values for testing data in Figures 6 and 9. However, in these data sets, the map resolution in terms of quantization errors, and topological preservation in terms of topographic errors tended to degrade, as in Tables I and II. The better prediction performance was obtained at the expense of resolution and topological preservation.

The better performance of our method can be explained by the use of inactive input neurons and the condensation of connection weights. First, the good performance was due to the use of many inactive neurons. In both data sets, important input neurons tended to respond mainly to the specific input patterns. For example, the first winner tended to respond to the immediately previous step ($t-1$th step) for predicting the present step (tth step), as in Figures 8 (a1) and 11 (a1). By introducing contradiction resolution, many different input neurons tended to respond to input patterns, as in Figures 8 (a2) and 11 (a2). In addition, almost uniform responses could be detected in 8 (b2) and 11 (b2). Our method tried to use many input neurons actively. On the other hand, other conventional methods used, such as variable selection methods dealt passively with input neurons or input variables. The active use of input neurons or variables was one of the main reasons for better prediction performance.

Second, we could observe the condensation of connection weights. Our method detected four groups in the Tankan data, as in Figure 7(b). In the dollar-yen exchange rate data, one major group and two minor ones were detected, as in Figure 10(b). On the other hand, no explicit regularity could be distinguished by the conventional SOM, as shown in 7(a) and 10(a). The condensation of connection weights into a small number of groups is another reason for better prediction performance.

2) Limitation and Problems of Method: Though our method produced better results across all data sets, we should point out three problems or limitations of our method, namely, the parameters β and α, and the resolution and topological preservation of the maps.

First, contradiction between self- and outer-evaluation is determined by the parameter β. We define the spread parameter σ_β by using the parameter β

$$\sigma_\beta = \frac{1}{\beta}. \qquad (28)$$

Thus, when the parameter β is increased, competition becomes more of the winner-take-all type. When the parameter β is decreased, the soft type of competition emerges. When the parameter β is too high, contradiction between self- and outer-evaluation becomes intense and produces maps that cannot well represent input patterns. Additionally, the characteristics shared by self- and outer-evaluation become clearer. Because of the focus on shared characteristics, the final maps do not necessarily represent input patterns accurately. On the other hand, when the parameter β is smaller, contradiction between self- and outer-evaluation becomes weaker and shared characteristics become weaker as well. At the present state of research, no explicit rules exist to determine the parameter β. Future studies should thus clarify the relationship between the parameter β and network performance.

Second, we have a problem determining the parameter α. Though competitive and input neurons are supposed to be governed by the same parameter, β in our formulation of contradiction resolution, we have empirically found that input and competitive neurons should be controlled by different parameter rules for better prediction performance. This means that in order to improve prediction performance, contradiction in competitive and input neurons should be more carefully treated. More concretely, by changing the values of the parameter α, we can change the characteristics of input and competitive neurons. For example, when α is small, an input neuron is more weakly evaluated, while competitive neurons are more strongly evaluated. We can control the relation between input and competitive neurons. Thus, we need to develop a method to take into account the different properties of competitive and input neurons.

Third, we have the problem of poorer resolution and topological preservation in terms of quantization and topographic errors. In all experimental results, we found that the best prediction performance was not accompanied by the better resolution and topological preservation. This means that better prediction performance is contradictory to better resolution and topological preservation. By the results of the PCA in Figures 7(b) and 10(b), we could see that connection weights were condensed into several groups by contradiction resolution. This condensation is related to better prediction and interpretation at the expense of quantization and topographic errors. Thus, we need to develop a method to provide better prediction performance, keeping higher resolution and topological preservation.

3) Possibility of the Method: The possibility of our method can be summarized by three points, namely, interpretation, application to time-series analysis and new types of evaluation. First, the method can be applied to the procedure where neural networks produce easily interpretable internal representations. In neural networks, a critical problem is how to interpret internal representations. Though many methods have been developed, we have had still serious problems with interpretation. Our method aims to produce explicit and interpretable representations by stressing the characteristics shared by self- and outer-evaluation.

Second, our method can be applied to the time series analysis. In the time series analysis, one key problem is how to take into account the previous states behind the present state. It has been difficult to consider long-term correlation between the present and the previous states. This is because conventional methods have tried to describe the time-series without taking into account the properties of input neurons. Our method can force some inactive input neurons to respond to input patterns through as many input neurons as possible. This property is very different from the conventional approach to time series analysis. Our method actively uses the previous steps, while conventional methods receive the previous steps very passively.

Third, we aim principally to describe and use many different types of evaluation for neurons. We have introduced self- and outer-evaluation, but these are only one realization of social interaction to be observed in neurons. We can imagine many different kinds of interaction between neurons. If it is possible to take into account different types of interactions between neurons, in particular, social interaction observed in actual human societies, then it will possible to model human societies and simulate how individual and collective human being behave.

IV. Conclusion

In the present paper, we introduced contradiction resolution to improve the prediction and interpretation performance of neural networks. Contradiction is realized in terms of competitive neurons, input neurons and the number of input neurons. For competitive neurons, there was contradiction between self- and outer-evaluation. In self-evaluation, the firing rate of a neuron is determined only by the neuron itself, while in outer-evaluation, the firing rates of a neuron are determined by all surrounding neurons. By resolving contradiction between self- and outer-evaluation, competitive neurons tend to acquire the collective behaviors realized by outer-evaluation.

For input neurons, there was contradiction between actual and expected responses. In our data, only a small number of specific input neurons tended to respond to input patterns. For example, the first winning input neuron tended to respond to the input neuron representing one period before ($t-1$th period). We expect an input neuron to respond to many types of input patterns.

For the number of input neurons, we resolved the contradiction by introducing dependent input neuron selection. We know that a small number of neurons (variables) are effective in improving prediction performance. In variable selection, the number of input variables is reduced to improve prediction performance. This reduction in the number of input neurons is contrary to the objective we achieved, namely, the diversity of input neurons. For resolving this contradiction, we introduced dependent input neuron selection. The number of input neurons was small for an input pattern. However, many input neurons were used on average. Thus, this dependent input neuron selection aims to resolve contradiction between a small number of neurons and the use of many input neurons.

We applied this contradiction resolution to two data sets, namely, the short term economic survey and dollar-yen exchange rates. In both sets, the first, the second and the third winners tended to respond to specific input neurons, the representing $t-1$th, $t-2$th and $t-3$th periods. By using contradiction resolution, the input neuron tended to respond to many different types of input neurons. For example, the first neuron did not necessarily respond to the first input neuron, but many different input neurons. In addition, connection weights were condensed into a small number of groups. This condensation is related to improved prediction performance.

However, we observed that quantization and topographic errors did not decrease by using contradiction resolution. Thus, when we try to interpret final connection weights, we should interpret them with due consideration of the quality of internal representations.

Though several problems should be solved for practical application, contradiction resolution can be used to improve prediction as well as interpretation performance.

References

[1] R. Kamimura, “Contradiction resolution between self and outer evaluation for supervised multi-layered neural networks,” *Journal of Advanced Research in Artificial Intelligence*, vol. 2, no. 7, pp. 29–38, 2013.

[2] R. Kamimura, "Separation and unification of individuality and collectivity and its application to explicit class structure in self-organizing maps," *Artificial Neural Networks and Machine Learning–ICANN 2012*, pp. 387–394, 2012.

[3] T. Kohonen, "The self-organizing maps," *Proceedings of the IEEE*, vol. 78, no. 9, pp. 1464–1480, 1990.

[4] T. Kohonen, *Self-Organization and Associative Memory*. New York: Springer-Verlag, 1988.

[5] T. Kohonen, *Self-Organizing Maps*. Springer-Verlag, 1995.

[6] J. Vesanto, "SOM-based data visualization methods," *Intelligent Data Analysis*, vol. 3, pp. 111–126, 1999.

[7] S. Kaski, J. Nikkila, and T. Kohonen, "Methods for interpreting a self-organized map in data analysis," in *Proceedings of European Symposium on Artificial Neural Networks*, (Bruges, Belgium), 1998.

[8] I. Mao and A. K. Jain, "Artificial neural networks for feature extraction and multivariate data projection," *IEEE Transactions on Neural Networks*, vol. 6, no. 2, pp. 296–317, 1995.

[9] C. De Runz, E. Desjardin, and M. Herbin, "Unsupervised visual data mining using self-organizing maps and a data-driven color mapping," in *Information Visualisation (IV), 2012 16th International Conference on*, pp. 241–245, IEEE, 2012.

[10] S. Shieh and I. Liao, "A new approach for data clustering and visualization using self-organizing maps," *Expert Systems with Applications*, 2012.

[11] H. Yin, "ViSOM-a novel method for multivariate data projection and structure visualization," *IEEE Transactions on Neural Networks*, vol. 13, no. 1, pp. 237–243, 2002.

[12] M.-C. Su and H.-T. Chang, "A new model of self-organizing neural networks and its application in data projection," *IEEE Transactions on Neural Networks*, vol. 123, no. 1, pp. 153–158, 2001.

[13] S. Wu and T. Chow, "Prsom: A new visualization method by hybridizing multidimensional scaling and self-organizing map," *Neural Networks, IEEE Transactions on*, vol. 16, no. 6, pp. 1362–1380, 2005.

[14] L. Xu, Y. Xu, and T. W. Chow, "PolSOM-a new method for multidimentional data visualization," *Pattern Recognition*, vol. 43, pp. 1668–1675, 2010.

[15] Y. Xu, L. Xu, and T. Chow, "Pposom: A new variant of polsom by using probabilistic assignment for multidimensional data visualization," *Neurocomputing*, vol. 74, no. 11, pp. 2018–2027, 2011.

[16] L. Xu and T. Chow, "Multivariate data classification using polsom," in *Prognostics and System Health Management Conference (PHM-Shenzhen), 2011*, pp. 1–4, IEEE, 2011.

[17] I. Guyon and A. Elisseeff, "An introduction to variable and feature selection," *Journal of Machine Learning Research*, vol. 3, pp. 1157–1182, 2003.

[18] A. Rakotomamonjy, "Variable selection using SVM-based criteria," *Journal of Machine Learning Research*, vol. 3, pp. 1357–1370, 2003.

[19] S. Perkins, K. Lacker, and J. Theiler, "Grafting: Fast, incremental feature selection by gradient descent in function space," *Journal of Machine Learning Research*, vol. 3, pp. 1333–1356, 2003.

[20] K. Kiviluoto, "Topology preservation in self-organizing maps," in *In Proceedings of the IEEE International Conference on Neural Networks*, pp. 294–299, 1996.

AUTHOR PROFILE

Ryotaro Kamimura is currently a professor of IT Education Center and Graduate School of Science and Technology of Tokai University in Japan. His research interests are information-theoretic approach to neural computing.

Evolving Software Effort Estimation Models Using Multigene Symbolic Regression Genetic Programming

Sultan Aljahdali and Alaa Sheta
Computer Science Department
College of Computers and Information Technology
Taif University
Taif, Saudi Arabia
aljahdali@tu.edu.sa, asheta66@gmail.com

***Abstract*—Software has played an essential role in engineering, economic development, stock market growth and military applications. Mature software industry count on highly predictive software effort estimation models. Correct estimation of software effort lead to correct estimation of budget and development time. It also allows companies to develop appropriate time plan for marketing campaign. Now a day it became a great challenge to get these estimates due to the increasing number of attributes which affect the software development life cycle. Software cost estimation models should be able to provide sufficient confidence on its prediction capabilities. Recently, Computational Intelligence (CI) paradigms were explored to handle the software effort estimation problem with promising results. In this paper we evolve two new models for software effort estimation using Multigene Symbolic Regression Genetic Programming (GP). One model utilizes the Source Line Of Code (SLOC) as input variable to estimate the Effort (E); while the second model utilize the Inputs, Outputs, Files, and User Inquiries to estimate the Function Point (FP). The proposed GP models show better estimation capabilities compared to other reported models in the literature. The validation results are accepted based Albrecht data set.**

I. Introduction

Estimating software effort on the early stage of development might produce uncertainty of up to 400% as mentioned in [1]. In 2001, it was also reported by the Standish group that, 53% of U.S. software projects ran over 189% of the original estimate [2]. In the 21st century software technology was capable on providing variety of software tools, techniques and software estimation models with many features which can help software project developer, manager, analyst and tester to do their job in a better way. The question that arises according to this opportunity, which tool and which model can really help in providing an accurate estimate? In most cases, the models adopted were based on expert judgment including Delphi technique [3] and work breakdown structure based methods. Models inspired by mathematical equations later came in line and named as Algorithmic Method. For example, Constructive Cost Model (COCOMO) [1], [4], Software Life Cycle Management (SLIM) [5], [6], and Software Evaluation and Estimation of Resources-Software Estimating Model (SEER-SEM) [7], Function Point models [8] and many others.

Practitioners figured out that the inability to correctly estimate software development costs is a challenging problem. Solving this problem becomes a pressure on IT companies since costs associated with their development became higher than before due to software complexity. As a result, more research focused on gaining a better understanding of the software development life cycle as well as the intelligent techniques which can help in developing accurate and efficient software cost estimation models.

In this paper, we continue exploring the idea of developing evolutionary software effort estimation models based on COCOMO and FP models [9]. Multigene Symbolic Regression GP shall be used to derive a mathematical model in both cases. The models should take in consideration the most important attributes which affect the effort modeling process for both the COCOMO and FP models.

II. Literature Review

Early investigations on using Machine Learning techniques as a tool for software development effort estimation were presented in [10]–[12]. Recently, Machine Learning techniques were also explored to solve the effort and cost estimation problem for software systems. In [10], author explored the use of Neural Networks (NNs), Genetic Algorithms (GAs) and Genetic Programming (GP) to provide a methodology for software cost estimation. A novel soft computing model to increase the accuracy of software development cost estimation was presented in [13]. Authors claims that their proposed NNs model can be interpreted and validated by experts, and has good generalization capability.

CI techniques were presented and analyzed for software cost estimation along with the emerging trends was presented in [14]. A new approach to find architectural design models based on multi-criteria genetic algorithm with optimal performance, reliability, and cost properties was presented in [15]. In [16], author provided a state of the art article on the use of search based approaches for software development effort estimation. The capabilities of these approaches were fully explored and the empirical analysis was carried out. A comparison between Neuro-fuzzy model and the most common software models such as Halstead, WalstonFelix, Bailey-Basili and Doty models was presented in [17].

In [18], author provided an innovative set of models modified from the famous COCOMO model with interesting results. Later on, many authors explored the same idea with some modification [19]–[22] and provided a comparison to the work presented in [18]. Exploration of the advantages of Fuzzy Logic using the Takagi-Sugeno (TS) technique on building a set of linear models over the domain of possible software Kilo Line Of Code (KLOC) were investigated in [23]. Authors in [24], [25] presented an extended work on the use of Particle Swarm Optimization (PSO) and Differential Evolution (DE) to build a suitable model structure to utilize improved estimations of software effort for NASA software projects. The developed PSO model provided promising results. Many model structures were explored including COCOMO-PSO, Fuzzy Logic (FL), Halstead, Walston-Felix, Bailey-Basili and Doty models. The potential of the developed COCOMO-PSO and FL models were high compared to other models from the literature.

III. COST ESTIMATION MODELS

A. COCOMO Model

COCOMO is one of the most famous software effort estimation model used in the literature. This model was originally developed by Barry Boehm [1], [4] and was extensively revised in [26]. The model is given by Equation 1. Recently, tuning the parameters of the COCOMO model using differential evolution to provide a better effort estimate was presented [25].

$$E = A \times Size^{B} \times EAF \tag{1}$$

Given that:

- E is the effort in person-months
- A is a calibrated constant
- B is a size scale factor
- $Size$ is measured by the Kilo Source Line of Code
- EAF is an Effort Adjustment Factor from cost factor multipliers

Software size may not be the most significant attribute in effort estimation but it does have major influence on the effort and time computation. If we could not accurately estimate the project size it is always hard to plan for project budget and duration. The values of the parameters A and B can be found in Table I. Three types of COCOMO models are presented. They are: Organic, Semidetached and Embedded models [27].

TABLE I. BASIC COCOMO MODELS

Model Name	Effort (E)	Time (T)
Organic Model	$E = 2.4(KLOC)^{1.05}$	$T = 2.5(E)^{0.38}$
Semi-Detached Model	$E = 3.0(KLOC)^{1.12}$	$T = 2.5(E)^{0.35}$
Embedded Model	$E = 3.6(KLOC)^{1.20}$	$T = 2.5(E)^{0.32}$

B. Function Point Model

Function points are a well-known concept although only recently they gained wider acceptance as a software size measure [28], [29]. Function points measure software size based on the functionality requested by and provided to the end user. Albrecht's function point gained acceptance during the 1980's and 1990's because of the tempting benefits compared to the models based on the SLOC [30], [31]. Albrecht proposed his model of computing the software size based on the system functionality [32], [33]. Albrecht originally proposed four function types [32]: files, inputs, outputs and inquiries with one set of associated weights and ten General System Characteristics (GSC). In 1983, the work developed in [33], proposed the expansion of the function type, a set of three weighting values (i.e. simple, average, complex) and fourteen General System Characteristics (GSCs) were proposed as given in Table II.

TABLE II. 1983 FUNCTION TYPES AND WEIGHTS

Function Type	Simple	Average	Complex
External Input	3	4	6
External Output	4	5	7
Internal Files	7	10	15
External Files	5	7	10
External Inquiry	3	4	6

Because FP is self-governing and independent of language type, platform, it can be used to identify many productivity benefits. FP is designed to estimate the time required for a software project development, and thereby the cost of the project and maintaining existing software systems. Because FP is self-governing and independent of language type, platform, it can be used to identify many productivity benefits. FP is designed to estimate the time required for a software project development, and thereby the cost of the project and maintaining existing software systems.

The Albrecht FP model consists of two parts 1) *Unadjusted Function Point* (UFP) and 2) *Adjusted Function Point* (AFP). The UFP consists of five components. They are given in Table II. There are also 14 GSCs factors that affect the size of the project effort, and each is ranked from "0"- no influence to "5"- essential. GSCs consists of 14 factors known as $f_1, f_2, \ldots, f_{14}$. These factors are listed in listed in Table III. The sum of all factors is then multiplied given in Equation 2 which constitute the Adjustment Factor (AF) defined in the range [0.65,-1.35]. Then, the Unadjusted FP is then multiplied by the UFP to create the Adjusted Function Point (AFP) count as given in Equation 3. The Adjusted FP value-will is within 35% of the original UFP figure.

$$AF = 0.65 + 0.01 \sum_{i=1}^{14} f_i \tag{2}$$

TABLE III. GENERAL SYSTEM CHARACTERISTICS (GSCS)

1	Data Communications
2	Distributed Functions
3	Performance
4	Heavily Used Configuration
5	Transaction Rate
6	Online Data Entry
7	End User Efficiency
8	Online Update
9	Complex Processing
10	Reusability
11	Installation Ease
12	Operational Ease
13	Multiple Sites
14	Facilitate Change

$$Adjusted\ FP = Unadjusted\ FP \times AF \tag{3}$$

IV. Genetic Programming

GP is an evolutionary computation technique which allows computer programs to evolve and produce a solution to a problem. GP a biologically inspired machine learning method which randomly generate a population of computer programs (i.e. solutions) represented by a trees structure of LISP expression [34], [35]. Using mutation and crossover, GP produce a new population of solution which is more likely to have better solution than their parents. This process in repeated till the end of certain number of generations or the best solution is reached. GP often use symbolic regression to build a mathematical model or expression based on given data set [36], [37]. The foremost advantages of GP is that; it evolves both the model structure (i.e. function) and the tune the model parameters. This makes GP more suitable to modeling and identification of nonlinear dynamic systems [38]–[42].

A. Multigene Symbolic Regression

Assume we are using GP to develop a model for a system with x inputs and y output. GP can produce a tree structure which introduce the mathematical relationship $y = f(x_1, x_2, \dots, x_n)$. Given that n is the number of input variables. In multigene symbolic regression, each prediction of the output variable $\hat{y}$ is formed by a weighted output of number of trees/genes in the multigene individual plus a bias term. Each tree is represents a model of zero or more of the given inputs n.

Mathematically, a multigene regression model can be written as:

$$\hat{y} = a_0 + a_1 \times tree_1 + \cdots + a_M \times tree_M \tag{4}$$

where a_0 represents the bias or offset term while $a_1, \dots, a_M$ are the gene weights and M is the number of genes (i.e. trees) which constitute the available individual. The weights (i.e. regression coefficients) usually computed using least square estimation for each tree. A multigene symbolic model usually consists of one of more gene (i.e. GP tree) weighted by linear combination parameter. An example of multigene model is shown in Figure 1. The presented model can be introduced mathematically as given in Equation 5.

$$\hat{y} = a_0 + a_1[x_1 x_2 + 9x_2] + a_2[22x_1 + x_3] \tag{5}$$

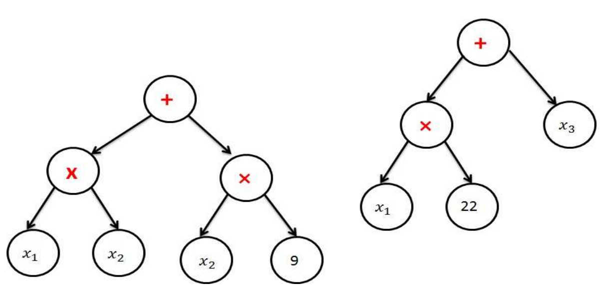

Fig. 1. A pseudo linear multigene model of output $\hat{y}$ along with x_1, x_2 and x_3 as inputs

B. Performance Criterion

The Route Mean Square (RMS) was used as the fitness function for genetic programming. RMS can be described by Equation 6.

$$RMS = \sqrt{\frac{1}{n}\sum_i (y_i - \hat{y}_i)^2} \tag{6}$$

Other performance criterion was used to evaluate the goodness of the developed GP model. They are given in following equations:

1) Variance-Accounted-For (VAF):

$$VAF = [1 - \frac{var(y-\hat{y})}{var(y)}] \times 100\% \tag{7}$$

2) Euclidian distance (ED):

$$ED = \sqrt{\sum_{i=1}^{n} (y_i - \hat{y}_i)^2} \tag{8}$$

3) Manhattan distance (MD):

$$MD = (\sum_{i=1}^{n} |y_i - \hat{y}_i|) \tag{9}$$

4) Mean Magnitude of Relative Error (MMRE):

$$MMRE = \frac{1}{n}\sum_{i=1}^{n} \frac{|y_i - \hat{y}_i|}{y_i} \tag{10}$$

where y and $\hat{y}$ are the actual and the estimated effort based on the developed GP model.

V. Experimental Results

A. Experimental Setup

To develop the proposed GP effort estimation model we used the GPTIPS [43] toolbox with the setting parameters given in Table IV. The default GPTIPS multigene symbolic regression function was used in order to minimize the root mean squared (RMS) prediction error on the training data. The default recombination operator probabilities were used as 0.85 for crossover, 0.1 for mutation and direct reproduction of 0.05.

TABLE IV. Tuning parameters of the GPTIPS Toolbox

Parameter	Value
Population size	25
Number of generations	300
Tournament size	10
Elitism	0.05
Maximum depth of trees	10
Maximum No. of genes	7;
function node set	+, -, ×

B. GP effort model as a function of SLOC

The famous COCOMO model always used the SLOC as main input to develop the effort equation as given in Equation 1. In our case, we adopted the COCOMO model as a basis for our development. Thus, we used the SLOC as an input and the effort as an output. The developed model is given in Equation 11 where x_1 stands for the SLOC.

$$\begin{aligned} y &= -\left(8.33\cdot 10^{-9}\right)\,\mathrm{x_1}^5 + \left(4.036\cdot 10^{-6}\right)\,\mathrm{x_1}^4 \\ &- 0.0005124\,\mathrm{x_1}^3 + 0.02337\,\mathrm{x_1}^2 \\ &- 0.08683\,\mathrm{x_1} + 1.401 \end{aligned} \tag{11}$$

In Figure 2, we show the GP convergence process where the best RMS was measured as 6.3475 which were received at generation 292. Figure 3 shows the actual and estimated effort using GP over the sorted list of projects. The characteristics between the two curves look very similar with high VAF criteria. In Table V, we show the values of each evaluation criteria adopted in this study.

TABLE V. GP BASED SLOC MODEL: PERFORMANCE CRITERION

VAF	ED	MD	MMRE
94.794%	31.097	100.27	0.48502

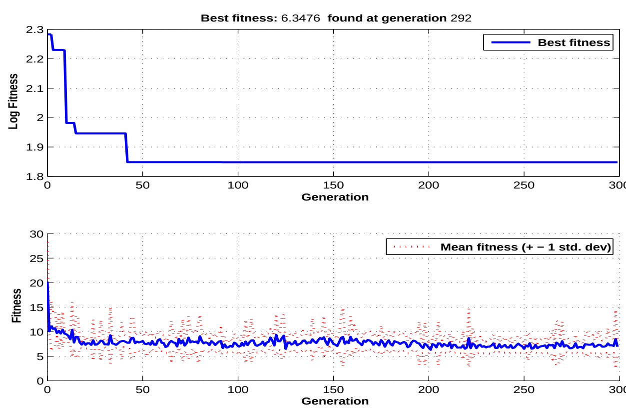

Fig. 2. GP convergence process in the effort estimation case

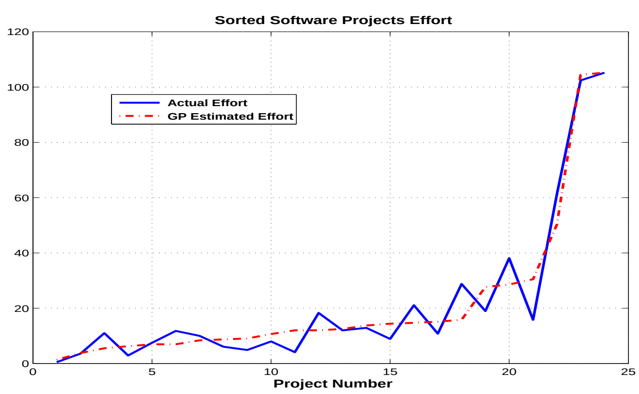

Fig. 3. Actual and estimated GP effort using SLOC Model

C. GP Effort model based FP

In this case, we are developing a GP model based the FP. The FP model utilizes the Inputs (x_1), Outputs (x_2), Files (x_3), and User Inquiries (x_4) to estimate the Function Point (FP). Thus, we considered these attributes as input to our model and the number of FP as an output. We run the GPTIPS [43] toolbox with the setting parameters given in Table IV. The developed GP model for the FP is given in Equation 12.

$$\begin{aligned} y &= 3.713\,\mathrm{x_2} - 10.29\,\mathrm{x_1} + 4.939\,\mathrm{x_3} + 3.682\,\mathrm{x_4} \\ &+ 0.1965\,\mathrm{x_1}\,\mathrm{x_2} + 1.011\,\mathrm{x_1}\,\mathrm{x_3} + 0.2481\,\mathrm{x_1}\,\mathrm{x_4} \\ &- 0.1838\,\mathrm{x_2}\,\mathrm{x_3} + 0.006156\,\mathrm{x_2}\,\mathrm{x_4} - 0.3135\,\mathrm{x_3}\,\mathrm{x_4} \\ &- 0.006156\,\mathrm{x_1}\,\mathrm{x_3}^2 + 0.006687\,\mathrm{x_2}\,\mathrm{x_3}^2 \\ &- 0.001063\,\mathrm{x_3}\,\mathrm{x_4}^2 - 0.002834\,\mathrm{x_3}^2\,\mathrm{x_4} \\ &+ 0.003078\,\mathrm{x_2}^2 - 0.2509\,\mathrm{x_3}^2 - 0.001063\,\mathrm{x_3}^3 \\ &+ 0.0001771\,\mathrm{x_1}\,\mathrm{x_2}\,\mathrm{x_3}^2 - 0.0001771\,\mathrm{x_1}\,\mathrm{x_3}^2\,\mathrm{x_4} \\ &- 0.01298\,\mathrm{x_1}\,\mathrm{x_2}\,\mathrm{x_3} - 0.003078\,\mathrm{x_1}\,\mathrm{x_3}\,\mathrm{x_4} \\ &+ 0.003255\,\mathrm{x_2}\,\mathrm{x_3}\,\mathrm{x_4} + 158.6 \end{aligned} \tag{12}$$

In Figure 4, we show the GP convergence process where the best RMS found was 30.8868 which were received at generation 297. Figure 5 shows the actual and estimated effort using GP based Albrecht data set adopted in this study. The developed model's performance were computed using number of criteria reported in Table VIII.

TABLE VI. ACTUAL AND ESTIMATED EFFORT USING GP

SLOC	Effort	GP-Effort
3	0.5	1.3373
15	3.6	3.8261
20	11	5.5339
22	2.9	6.2505
24	7.5	6.9704
24	11.8	6.9704
28	10	8.386
29	6.1	8.7295
30	4.9	9.0674
35	8	10.651
40	4.1	12.023
40	18.3	12.023
42	12	12.508
48	12.9	13.748
52	8.9	14.421
54	21.1	14.723
57	10.8	15.148
62	28.8	15.832
93	19	27.72
94	38.1	28.597
96	15.8	30.497
110	61.2	50.263
130	102.4	104.48
318	105.2	105.2

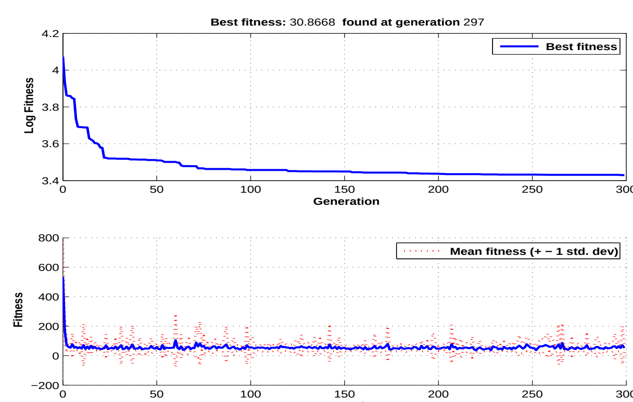

Fig. 4. GP convergence process in FP estimation case

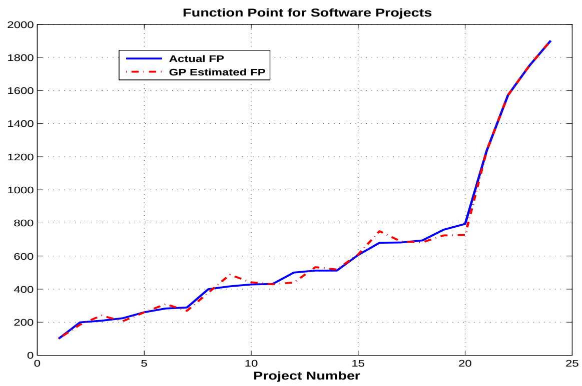

Fig. 5. Actual and estimated GP Function Points results

TABLE VII. ACTUAL AND ESTIMATED GP NUMBER OF FP

Inputs	Outputs	Files	Inquiries	FP	GP-FP
34	14	5	0	100	100.54
15	15	3	6	199	185.25
7	12	8	13	209	240.35
33	17	5	8	224	206
12	15	15	0	260	259.65
13	19	23	0	283	309.26
17	17	5	15	289	269.24
27	20	6	24	400	378.86
28	41	11	16	417	486.84
70	27	12	0	428	441.28
10	69	9	1	431	429.19
25	28	22	4	500	439.86
41	27	5	29	512	532.66
28	38	9	24	512	518.51
42	57	5	12	606	609.39
45	64	16	14	680	750.1
43	40	35	20	682	687.45
61	68	11	0	694	682.89
40	60	12	20	759	724.64
40	60	15	20	794	727.36
48	66	50	13	1235	1234.9
69	112	39	21	1572	1571.7
25	150	60	75	1750	1750.2
193	98	36	70	1902	1901.9

VI. CONCLUSIONS AND FUTURE WORK

In this paper, an evolutionary software effort estimation models based Multigene Symbolic Regression Genetic Programming were developed. Two GP based models were developed; one model considered the Source Line Of Code (SLOC) as input variable to estimate the Effort (E); while the second model considered the Inputs, Outputs, Files, and User Inquiries to estimate the Function Point (FP). The proposed GP models show better performance compared to other reported models in the literature. They were tested using the Albrecht data set reported in [12]. The mathematical equation which represents both models is adequately simple and can be easily used to predict further project's effort. These types of models significant help project managers to estimate time and cost for future developments.

ACKNOWLEDGMENTS

Dr. Sultan Aljahdali would like to acknowledge the financial support of King Abdulaziz City for Science and Technology and Taif University during his short research visit to Prof. Jayantha Herath with the Computer Science Department, St. Cloud State University, St. Cloud, MN 56301, USA on the Summer of 2013.

TABLE VIII. GP BASED FP MODEL: PERFORMANCE CRITERION

VAF	ED	MD	MMRE
99.59%	151.22	20.63	0.048274

REFERENCES

[1] B. Boehm, *Software Engineering Economics*. Englewood Cliffs, NJ, Prentice-Hall, 1981.

[2] T. S. Group, *CHAOS Chronicles*. PhD thesis, Standish Group Internet Report, 1995.

[3] P. Suri and P. Ranjan, "Article: Comparative analysis of software effort estimation techniques," *International Journal of Computer Applications*, vol. 48, pp. 12–19, June 2012. Published by Foundation of Computer Science, New York, USA.

[4] B. Boehm, *Cost Models for Future Software Life Cycle Process: COCOMO2*. Annals of Software Engineering, 1995.

[5] L. Putnam and W. Myers, *Measures for excellence*. Yourdon Press Computing Series, 1992.

[6] L. Putnam, "A general empirical solution to the macro software sizing and estimation problem," *IEEE Transactionson Software Engineering*, vol. 4, no. 4, pp. 345–381, 1978.

[7] R. Jensen, "An improved macrolevel software development resource estimation model," in *In Proceedings of 5th Conference of International S Parametric Analysts*, pp. 88–92, 1983.

[8] J. E. Matson, B. E. Barret, and J. M. Mellinchamp, "Software developemnet cost estimation using function points," *IEEE Trans. Software Engineering*, vol. 20, no. 4, pp. 275–287, 1994.

[9] A. Sheta and S. Aljahdali, "Software effort estimation inspired by COCOMO and FP models: A fuzzy logic approach," *International Journal of Advanced Computer Science and Applications*, vol. 4, Dec. 2013.

[10] M. A. Kelly, "A methodlolgy for software cost estimation using machine learning techniques," Master's thesis, Naval Postgratuate School, Monterey, California, 1993.

[11] G. R. Finnie and G. E. Wittig, "AI tools for software development effort estimation," in *Proceedings of the 1996 International Conference on Software Engineering: Education and Practice (SE:EP '96)*, SEEP '96, (Washington, DC, USA), pp. 346–, IEEE Computer Society, 1996.

[12] C. Schofield, *An Empirical Investigation into Software Effort Estimation by Analogy*. PhD thesis, Bournemouth University, 1998.

[13] I. Attarzadeh and S. H. Ow, "A novel soft computing model to increase the accuracy of software development cost estimation," in *2010 The 2nd International Conference on Computer and Automation Engineering (ICCAE)*, vol. 3, pp. 603–607, 2010.

[14] T. R. Benala, S. Dehuri, and R. Mall, "Computational intelligence in software cost estimation: an emerging paradigm," *SIGSOFT Software Engineering Notes*, vol. 37, pp. 1–7, May 2012.

[15] A. Martens, H. Koziolek, S. Becker, and R. Reussner, "Automatically improve software architecture models for performance, reliability, and cost using evolutionary algorithms," in *Proceedings of the first joint WOSP/SIPEW international conference on Performance engineering*, WOSP/SIPEW '10, (New York, NY, USA), pp. 105–116, ACM, 2010.

[16] F. Sarro, "Search-based approaches for software development effort estimation," in *Proceedings of the 12th International Conference on Product Focused Software Development and Process Improvement*, Profes '11, (New York, NY, USA), pp. 38–43, ACM, 2011.

[17] U. Saxena and S. P. Singh, "Software effort estimation using neuro-fuzzy approach," in *2012 CSI Sixth International Conference on Software Engineering (CONSEG)*, pp. 1–6, 2012.

[18] A. F. Sheta, "Estimation of the COCOMO model parameters using genetic algorithms for NASA software projects," *Journal of Computer Science*, vol. 2, no. 2, pp. 118–123, 2006.

[19] H. Mittal and P. Bhatia, "A comparative study of conventional effort estimation and fuzzy effort estimation based on triangular fuzzy numbers," *International Journal of Computer Science and Security*, vol. 1, no. 4, pp. 36–47, 2007.

[20] H. Mittal and P. Bhatia, "Optimization criteria for effort estimation using fuzzy technique," *CLEI Electronic Journal*, vol. 10, no. 1, pp. 1–11, 2007.

[21] M. Uysal, "Estimation of the effort component of the software projects using simulated annealing algorithm," in *World Academy of Science, Engineering and Technology*, vol. 41, pp. 258–261, 2008.

[22] P. S. Sandhu, M. Prashar, P. Bassi, and A. Bisht, "A model for estimation of efforts in development of software systems," in *World Academy of Science, Engineering and Technology*, vol. 56, pp. 148–152, 2009.

[23] A. Sheta, "Software effort estimation and stock market prediction using takagi-sugeno fuzzy models," in *Proceedings of the 2006 IEEE Fuzzy Logic Conference, Sheraton, Vancouver Wall Centre, Vancouver, BC, Canada, July 16-21*, pp. 579–586, 2006.

[24] A. Sheta, D. Rine, and A. Ayesh, "Development of software effort and schedule estimation models using soft computing techniques," in *Proceedings of the 2008 IEEE Congress on Evolutionary Computation (IEEE CEC 2008) within the 2008 IEEE World Congress on Computational Intelligence (WCCI 2008), Hong Kong, 1-6 June*, pp. 1283–1289, 2008.

[25] S. Aljahdali and A. Sheta, "Software effort estimation by tuning COOCMO model parameters using differential evolution," in *2010 IEEE/ACS International Conference on Computer Systems and Applications (AICCSA)*, pp. 1–6, 2010.

[26] B. Boehm and et all, *Software Cost Estimation with COCOMO II*. Prentice Hall PTR, 2000.

[27] O. Benediktsson, D. Dalcher, K. Reed, and M. Woodman, "COCOMO based effort estimation for iterative and incremental software development," *Software Quality Journal*, vol. 11, pp. 265–281, 2003.

[28] J. Moses, "Measuring effort estimation uncertainty to improve client confidence," *Software Quality Control*, vol. 10, pp. 135–148, Sept. 2002.

[29] J. Wu and X. Cai, "A software size measurement model for large-scale business applications," in *Proceedings of the 2008 International Conference on Computer Science and Software Engineering - Volume 02*, CSSE '08, (Washington, DC, USA), pp. 39–42, IEEE Computer Society, 2008.

[30] R. Rask, P. Laamanen, and K. Lyytinen, "A comparison of albrecht's function point and symons' mark ii metrics," in *Proceedings of the thirteenth international conference on Information systems*, ICIS '92, (Minneapolis, MN, USA), pp. 207–221, University of Minnesota, 1992.

[31] S. Furey, "Why we should use function points [software metrics]," *IEEE Software*, vol. 14, pp. 28, 30–, Mar. 1997.

[32] A. J. Albrecht, "Measuring application development productivity," in *Proceedings of the Joint SHARE, GUIDE, and IBM Application Developments Symposium*, pp. 83–92, 1979.

[33] A. J. Albrecht and J. E. Gaffney, "Software function, source lines of code, and development effort prediction: A software science validation," *IEEE Transactions on Software Engineering*, vol. 9, no. 6, pp. 639–648, 1983.

[34] J. Koza, "Evolving a computer program to generate random numbers using the genetic programming paradigm," in *Proceedings of the Fourth International Conference on Genetic Algorithms*, Morgan Kaufmann, La Jolla,CA, 1991.

[35] J. R. Koza, *Genetic Programming: On the Programming of Computers by Means of Natural Selection*. The MIT Press, 1992.

[36] J. R. Koza, ed., *Genetic Algorithms and Genetic Programming at Stanford 2003*. Stanford, California, 94305-3079 USA: Stanford University Bookstore, June 2003.

[37] J. R. Koza, "Human-competitive results produced by genetic programming," *Genetic Programming and Evolvable Machines*, vol. 11, pp. 251–284, Sept. 2010.

[38] A. Sheta and A. Al-Afeef, "A GP effort estimation model utilizing line of code and methodology for NASA software projects," in *2010 10th International Conference on Intelligent Systems Design and Applications (ISDA)*, pp. 290–295, 2010.

[39] H. Faris, M. Al-kasassbeh, and A. Sheta, "Predicting stock abundance of the barents sea capelin using genetic programming," *International Review on Computers and Software (IRECOS)*, vol. 7, no. 4, 2012.

[40] H. Faris and A. Sheta, "Identification of the tennessee eastman chemical process reactor using genetic programming," *International Journal of Advanced Science and Technology*, vol. 50, pp. 121–140, Jan. 2013.

[41] H. Faris, A. Sheta, and E. Oznergiz, "Modeling hot rolling manufacturing process using soft computing techniques," *International Journal of Computer Integrated Manufacturing*, vol. 26, no. 8, 2013.

[42] A. Sheta, R. Hiary, H. Faris, and N. Ghatasheh, "Optimizing thermostable enzymes production using multigene symbolic regression genetic programming," *World Applied Sciences*, vol. 22, no. 4, pp. 485–493, 2013.

[43] D. P. Searson, D. E. Leahy, and M. J. Willis, "GPTIPS : An open source genetic programming toolbox for multigene symbolic regression," in *Proceedings of the International Multi-conference of Engineers and Computer Scientists*, vol. 1, (Hong Kong), pp. 77–80, 17-19 Mar. 2010.